Computational studies on the structure and stabilities of magnetic inter-metallic compounds

Dissertation
zur Erlangung des Grades
"Doktor der Naturwissenschaften"
am Fachbereich Chemie, Pharmazie und Geowissenschaften
der Johannes Gutenberg-Universität Mainz

vorgelegt von
Hem Chandra Kandpal
geboren in Almora (INDIA)

Mainz, 2006

Dekan: Prof. Dr. Peter Langguth

Tag der mündlichen Prüfung: 20th July 2007

This work was carried out from October 2002 to December 2006 at the Institut für Anorganische und Analytische Chemie, Johannes Gutenberg-Universität, Mainz under the supervision of Prof. Dr. Claudia Felser.

I declare that I wrote this work myself and carried out the computational study described in it, without using any other sources and aids than those that are stated.

Mainz, December 2006

Thesis advisor

Claudia Felser

Author

Hem Chandra Kandpal

Computational studies on the structure and stabilities of magnetic inter-metallic compounds

Abstract

The purpose of this thesis is to further the understanding of the structural, electronic and magnetic properties of ternary inter-metallic compounds using density functional theory (DFT). Four main problems are addressed. First, a detailed analysis on the ternary Heusler compounds is made. It has long been known that many Heusler compounds (X_2YZ; X and Y transition elements, Z main group element) exhibit interesting half-metallic and ferromagnetic properties. In order to understand these, the dependence of magnetic and electronic properties on the structural parameters, the type of exchange-correlation functional and electron-electron correlation was examined. It was found that almost all Co_2YZ Heusler compounds exhibit half-metallic ferromagnetism. It is also observed that X and Y atoms mainly contribute to the total magnetic moment. The magnitude of the total magnetic moment is determined only indirectly by the nature of Z atoms, and shows a trend consistent with Slater-Pauling behaviour in several classes of these compounds. In contrast to experiments, calculations give a non-integer value of the magnetic moment in certain Co_2-based Heusler compounds. To explain deviations of the calculated magnetic moment, the LDA+U scheme was applied and it was found that the inclusion of electron-electron correlation beyond the LSDA and GGA is necessary to obtain theoretical description of some Heusler compounds that are half-metallic ferromagnets. The electronic structure and magnetic properties of substitutional series of the quaternary Heusler compound $Co_2Mn_{1-x}Fe_xSi$ were investigated under LDA+U. The calculated band structure suggest that the most stable compound in a half-metallic state will occur at an intermediate Fe concentration. These calculated findings are qualitatively confirmed by experimental studies.

Second, the effect of antisite disordering in the Co_2TiSn system was investigated theo-

retically as well as experimentally. Preservation of half-metallicity for Co_2TiSn was observed with moderate antisite disordering and experimental findings suggest that the Co and Ti antisites disorder amounts to approximately 10 % in the compound.

Third, a systematic examination was carried out for band gaps and the nature (covalent or ionic) of bonding in semiconducting 8- and 18-electron or half-metallic ferromagnet half-Heusler compounds. It was found that the most appropriate description of these compounds from the viewpoint of electronic structures is one of a YZ zinc blende lattice stuffed by the X ion. Simple valence rules are obeyed for bonding in the 8- and 18-electron compounds.

Fourth, hexagonal analogues of half-Heusler compounds have been searched. Three series of compounds were investigated: GdPdSb, GdAuX (X = Mn, Cd and In) and EuNiP. GdPdSb is suggested as a possible half-metallic weak ferromagnet at low temperature. GdAuX (X = Mn, Cd and In) and EuNiP were investigated because they exhibit interesting bonding, structural and magnetic properties. The results qualitatively confirm experimental studies on magnetic and structural behaviour in GdPdSb, GdAuX (X = Mn, Cd and In) and EuNiP compounds.

Contents

List of Figures

List of Tables

Citations to Previously Published Work

Large portions of Chapters 2 and 3 have appeared in the following papers:

> "Calculated electronic and magnetic properties of the half-metallic, transition metal based Heusler compounds",
> Hem C. Kandpal, Gerhard H. Fecher and Claudia Felser,
> J. Phys. D (submitted),
>
> "Correlation in the transition-metal-based Heusler compounds Co_2MnSi and Co_2FeSi",
> Hem C. Kandpal, Gerhard H. Fecher, Claudia Felser and Gerd Schönhense,
> Phys. Rev. B **73**, 094422 (2006),
>
> "Slater-Pauling rule and Curie temperature of Co_2-based Heusler compounds",
> Gerhard H. Fecher, Hem C. Kandpal, Sabine Wurmehl, Claudia Felser and Gerd Schoïhense,
> J. Appl. Phys. **99**, 08J106 (2006),
>
> "Correlation in Heusler compounds Co_2YSi (Y = 3*d* transition metals)",
> Hem C. Kandpal, Claudia Felser and Gerhard H. Fecher,
> J. Magn. Magn. Mater. (accepted) (2006),
>
> "Properties of the quaternary half-metal-type Heusler alloy $Co_2Mn_{1-x}Fe_xSi$",
> Benjamin Balke, Gerhard H. Fecher, Hem C. Kandpal, Claudia Felser, K. Kobayashi, E. lkenaga, J. -J. Kim and S. Ueda,
> Phys. Rev. B **74**, 104405 (2006),

Chapter 4 appears in its entirety as

> "Electronic structure, magnetism, and disorder in the Heusler compound Co_2TiSn",
> Hem C. Kandpal, Vadim Ksenofontov, Marek Wojcik, Ram Seshadri, and Claudia Felser,
> J. Phys. D (accepted),

Chapter 5 appears in its entirety as

> "Covalent bonding and the nature of band gaps in some half-Heusler compounds",
> Hem C. Kandpal, Claudia Felser and Ram Seshadri,
> J. Phys. D: Appl. Phys. **39**, 776 (2006).

Chapter 6, Chapter 7, and Chapter 8 have been published as

> "GdPdSb: a possible half metal and weak ferromagnet at low temperature",
> Frederick Casper, Hem C. Kandpal, Vadim Ksenofontov, and Claudia Felser,
> J. Phys. D (submitted),
>
> "Variation of the bonding interactions in GdAuX (X=Mg, Cd, and In)",
> Hem C. Kandpal, Gerhard H. Fecher, Claudia Felser and Rainer Pöttgen,
> in preparation,
>
> "Verwey-type transition in EuNiP",
> Vadim Ksenofontov, Hem C. Kandpal, J. Ensling, M. Waldeck, D. Johrendt, A. Mewis, P. Gütlich and C. Felser,
> Europhys. Lett. **74**, 672 (2006).

Finally, most of the published work can be found in the publication list.

Publications

1. Hem C. Kandpal and Ram Seshadri
   First-principles electronic structure of the delafossites ABO_2 (A = Cu, Ag, Au; B = Al, Ga, Sc, In, Y): Evolution of d^{10}-d^{10} interactions
   Solid State Sciences **4** (2002) 1045.

2. Umesah V. Waghmare, Nicola A. Hill, Hem C. Kandpal, and Ram Seshadri
   First principles indicators of metallicity and cation off-centricity in the IV-VI rock-salt chalcogenides of divalent Ge, Sn and Pb
   Phys. Rev. B **67** (2003) 125111.

3. Marcus Lauer, Roser Valenti, Hem C. Kandpal, and Ram Seshadri
   First principles electronic structure of spinel $LiCr_2O_4$: A possible half metal
   Phys. Rev. B **69** (2004) 075117-(1-8).

4. G. Melnyk, Hem C. Kandpal, L. D. Gulay, and W. Tremel
   Crystal structures of R_2Pd_2Pb (R = Y, LA, Ce, Pr, Nd, Sm, Gd, Tb, Dy, Ho, Er, Tm, and Lu) compounds
   J. Alloys Comps. **370** (2004) 217.

5. S. Wurmehl, G. H. Fecher, Hem C. Kandpal, K. Kroth, H.-J Elmers, G. Schönhense, C. Felser, J. Morais, Y. Hwu, and R. Klauser
   Z. Anorg. Allg. Chem. **630** (2004) 1771.

6. Gerhard H. Fecher, Hem C. Kandpal, Sabine Wurmehl, and Claudia Felser
   Slater-Pauling Rule and Curie-Temperature of Co_2-based Heusler compounds
   J. Appl. Phys. **99** (2006) 08J106.

7. Gerhard H. Fecher, Hem Chandra Kandpal, Sabine Wurmehl, Jonder Morais, Hong-Ji Lin, Hans-Joachim Elmers, Gerd Schönhense, and Claudia Felser
   Design of magnetic materials: The electronic structure of the ordered, doped Heusler compound $Co_2Cr_{1-x}Fe_xAl$
   J. Phys. Condens. Matter **17** (2005) 7237.

8. Sabine Wurmehl, Gerhard H. Fecher, Hem Chandra Kandpal, Vadim Ksenofontov, Claudia Felseri, and Hong-Ji Lin
   Investigation of Co_2FeSi: The Heusler compound with highest Curie temperature and magnetic moment
   Appl. Phys. Lett. **88** (2006) 032503.

9. Sabine Wurmehl, Gerhard H. Fecher, Hem Chandra Kandpal, Vadim Ksenofontov, and Claudia Felser
   Geometric, electronic, and magnetic structure of Co_2FeSi: Curie temperature and magnetic moment measurements and calculations
   Phys. Rev. B **72** (2005) 184434.

10. M. Kallmayer, H. Schneider, G. Jakob, H.-J Elmers, K. Kroth, Hem C. Kandpal, U. Stumm, and S. Cramm
    Reduction of surface magnetism of $Co_2Cr_{0.6}Fe_{0.4}Al$ Heusler alloy films
    Appl. Phys. Lett. **88** (2006) 072506.

11. A. Gloskovskii, S. A. Nepijko, M. Cinchetti, G. Schönhense, G. H. Fecher, Hem C. Kandpal, Claudia Felser, H. A. Therese, N. Zink, W. Tremel, and A. Oelsner
    Time-of-flight photoelectron spectromicroscopy of single MoS_2 nanotubes
    J. Appl. Phys. (accepted).

12. Hem Chandra Kandpal, Claudia Felser, and Ram Seshadri
Covalent bonding and the nature of band gaps in some half-Heusler compounds
J. Phys. D **39** (2006) 776.

13. V. Ksenofontov, Hem.C. Kandpal, J. Ensling, M. Waldeck, D. Johrendt, A. Mewis, P. Gütlich, and C. Felser
Verwey-type transition in EuNiP
Euro. Phys. Lett. **74** (2006) 672.

14. Frederick Casper, Vadim Ksenofontov, Hem Chandra Kandpal, Sergey Reiman, Toetsu Shishido, Masashi Takahashi, Masuo Takeda, and Claudia Felser
Z. Anorg. Allg. Chem. **632** (2006) 1273.

15. Frederick Casper, Hem Chandra Kandpal, Vadim Ksenofontov, and Claudia Felser
GdPdSb as possible half-metal and weak ferromagnet at low temperature
J. Phys. D (submitted) 2006.

16. Hem Chandra Kandpal, Gerhard H. Fecher, Claudia Felser, and Gerd Schönhense
Correlation in the transition metal based Heusler compounds Co_2MnSi and Co_2FeSi
Phys. Rev. B **73** (2006) 094422.

17. Benjamin Balke, Hem C. Kandpal, Gerhard H. Fecher, and Claudia felser
The half-metallic ferromagnet $Co_2Mn_{0.5}Fe_{0.5}Si$
J. Magn. Magn. Mater. (accepted) 2006.

18. Benjamin Balke, Gerhard H. Fecher, Hem C. Kandpal, and Claudia Felser
Properties of the quaternary half-metal-type Heusler alloy $Co_2Mn_{1-x}Fe_xSi$
Phys. Rev. B **74** (2006) 104405.

19. Sabine Wurmehl, Hem C. Kandpal, Gerhard H. Fecher, and Claudia Felser
Valence electron rules for prediction of half-metallic compensated ferrimagnetic behaviour of Heusler compounds with complete spin polarization
J. Phys.: Condens Matter **18** (2006) 6171.

20. Hem C. Kandpal, Claudia Felser, and Gerhard H. Fecher
Correlation in Heusler compounds Co_2YSi (Y = Sc, Ti, V, Cr, Mn, Fe)
J. Magn. Magn. Mater. (accepted) 2006.

21. Hem C. Kandpal, Gerhard H. Fecher, Claudia Felser, and Rainer Pöttgen
Variation of the bonding interactions in GdAuX (X = Mg, Cd, and In)
in preparation 2006.

22. Hem C. Kandpal, Gerhard H. Fecher, and Claudia Felser
Calculated electronic and magnetic properties of the half-metallic, transition metal based Heusler compounds
J. Phys. D (submitted) 2006.

23. Hem C. Kandpal, Vadim Ksenofontov, Marek Wojcik, Ram Seshadri and Claudia Felser
Electronic structure , magnetism, and disorder in the Heusler compound Co_2TiSn
J. Phys. D (accepted) 2006.

Dedicated to my late sister Geeta,
and my mother.

Chapter 1

Introduction

Materials that exhibit half-metallic ferromagnetism are seen to be potential candidates for the field of application being called spintronics [38, 183], that is electronics, making use of the electron-spin instead of its charge. The concept of half-metallic ferromagnetism was first presented by de Groot [41], predicting it to appear in cubic $C1_b$ compounds. The model suggests that the density of states exhibit a gap for minority electrons around the Fermi energy (ϵ_F). Thus, these materials are 100% spin polarized at ϵ_F. Most of the compounds predicted to be half-metallic ferromagnets (HMF) belong to the group of Heusler [70] compounds. Since then, the properties have been identified in some of the cubic $C1_b$ [41], Heusler [23] and other compounds [39, 98, 135, 171]. It was shown that Co_2FeSi is a very good candidate since it exhibits a very high Curie temperature of 1100 K and a magnetic moment of $6\mu_B$ [176]. The first principles band structure calculations reveal the appearance of a gap in the minority bands in Co_2FeSi [96]. In fact, a large number of band structure calculations revealed the appearance of half-metallic ferromagnetic behavior in Heusler compounds [81]. In general, these are ternary X_2YZ-compounds, crystallize in the $L2_1$ structure. X and Y are usually transition metals while Z is a main group element.

In the past few years, the efforts to create spintronic devices have led to the need for materials that exhibit high Curie temperatures, high magnetic moments, and of course large gaps in one spin direction. Indeed the most important requirement is a large spin polarization at ϵ_F. The search for materials, exhibiting all these properties has led to numerous studies on different materials. Heusler compounds belong to the class of materials having such properties and thus are good candidates for spintronic materials. Investigation on bulk, thin film [63, 64, 146, 94, 170, 169], as devices [79, 95, 113], along with theoretical predictions, have been undertaken primarily in the last few years in the hope of finding suitable material for spintronics.

For both scientific and technological reasons it is important to measure directly and easily

the electronic spin polarization at ϵ_F of a material, although it is difficult to measure spin polarization at ϵ_F of a ferromagnet [92]. The spin-polarization at ϵ_F in a crude approximation is defined by:

$$P = \frac{N_\uparrow(E_\mathrm{F}) - N_\downarrow(E_\mathrm{F})}{N_\uparrow(E_\mathrm{F}) + N_\downarrow(E_\mathrm{F})} \times 100\%, \tag{1.1}$$

where $N_\uparrow(E_\mathrm{F})$ and $N_\downarrow(E_\mathrm{F})$ are the spin dependent density of states at ϵ_F. When the electrons are fully spin polarized, either $N_\uparrow(E_\mathrm{F})$ or $N_\downarrow(E_\mathrm{F})$ is equal to zero and therefore the spin polarization will be 100%.

The goal of this work is a systematic study of these compounds which may help to design potential new half-metallic compounds. Density functional theory is a powerful tool for computational materials sciences, and can be used successfully both to explain phenomena observed in existing materials, and to design new ones with specific properties. First principles calculations based on density functional theory have contributed significantly to our current understanding of the electronic and magnetic behavior of the Heusler compounds.

1.1 First principles methods

The equations that govern interactions between the electrons and nuclei of solids have been well known for decades, but finding their exact solution for a complex solid is beyond the limits of current computing power. However, using a series of approximations, the electronic structure and thus the total energy of most materials can be calculated quite accurately. A wide variety of first-principles methods are used to determine the behavior of materials. Materials have different types of bonding interactions and therefore some approximations are better suited than others for a particular system of interest.

1.1.1 Density functional theory (DFT) and local density approximation (LDA)

Since its introduction in the 1960s [73, 99] density functional theory (DFT) has evolved into a powerful tool that is widely used in condensed matter theory and computational materials science for the calculation of electronic, magnetic and structural properties of solids. The method has been remarkably successful in predicting, reproducing and explaining a wide variety of materials phenomena. Specific example range from early predictions of magnetic, electronic properties and understanding various physical properties of the systems.

Density functional theory (DFT) enables the description of the ground state properties of a real system in terms of its ground state electronic charge density $\rho(\mathbf{r})$, a parameter simply depending on a single spatial coordinate $\mathbf{r}$, instead of the wave functions which depend on all the

electronic coordinates $\mathbf{r}_i$. In this formalism, all the physical quantities related to the ground state, are expressed as functionals of the charge density, $F[\rho(\mathbf{r})]$. As was shown by Hohenberg and Kohn (and later extended by Levy) [73, 108], all ground state properties of a crystal are uniquely determined by the electron charge density.

Hohenberg and Kohn demonstrated that there exists a unique universal functional $E[\rho(\mathbf{r})]$ of the ground state electron density, which satisfies the variational principle with respect to the electron density:

$$E[\rho(\mathbf{r})] = \int \upsilon(\mathbf{r})\rho(\mathbf{r})\, d\mathbf{r} + F[\rho(\mathbf{r})] \tag{1.2}$$

where $F[\rho(\mathbf{r})]$ contains the electronic kinetic energy (T) and the electronic Coulomb interaction (V_{ee})

$$F[\rho(\mathbf{r})] =< \phi|T + V_{ee}|\phi > \tag{1.3}$$

and $\upsilon(\mathbf{r})$ represents the Coulomb potential due to the nuclei of the solid. The fundamental Hohenberg-Kohn theorem of the density functional theory states that the ground state energy can be obtained by minimization of the functional (1.2), constrained with the conservation of the total charge.

Unfortunately, the universal functional $F[\rho(\mathbf{r})]$ is not known. To solve this problem, Kohn and Sham [99] introduced an additional development by mapping the original interacting problem into an effective and non-interacting problem with a slightly different potential V_{KS}, called the *effective Kohn-Sham potential*. The density functional $F[\rho(\mathbf{r})]$ for the interacting system is given by the sum of the kinetic energies of a non-interacting electron gas with the same density $\rho(\mathbf{r})$ as the original one, and additional terms that describe the inter-particle interactions

$$F[\rho] = T_s[\rho] + J[\rho] + E_{xc}[\rho] \tag{1.4}$$

where $T_s[\rho]$ is the kinetic energy of a non-interacting electron gas, $J[\rho]$ is the classical Coulomb energy (often referred as Hartree term)

$$J[\rho] = \frac{e^2}{2} \int\int \frac{\rho(\mathbf{r})\rho(\mathbf{r}')}{|\mathbf{r} - \mathbf{r}'|}\, d\mathbf{r}\, d\mathbf{r}' \tag{1.5}$$

and $E_{xc}[\rho]$ is called *exchange-correlation energy* and contains all many-body effects not described by the other terms. In other words, $E_{xc}[\rho]$ describes the difference between the real system and the effective non-interacting system (including the correction for the kinetic energy and the Coulomb interactions):

$$E_{xc}[\rho] = \{T[\rho] + V_{ee}[\rho]\} - \{T_s[\rho] + J[\rho]\} \tag{1.6}$$

The difference is usually expected to be small, and $E_{xc}[\rho]$ principally contains the correction of $J[\rho]$ arising from the correlations between electrons.

From equation 1.4 it is possible to extract the effective Kohn-Sham potential V_{KS}, by imposing that the energy functional $E[\rho(\mathbf{r})]$ for the interacting problem must be minimized by the same electron density $\rho(\mathbf{r})$ that minimizes the energy $E_s[\rho(\mathbf{r})]$ of the non-interacting electron gas.

$$\left[-\frac{1}{2}\nabla^2 + V_{KS}\right]\phi_i(\mathbf{r}) = \varepsilon_{\mathbf{i}}\phi_{\mathbf{i}}(\mathbf{r}) \tag{1.7}$$

where

$$V_{KS}(\mathbf{r}) = \upsilon(\mathbf{r}) + e^2\int \frac{\rho(\mathbf{r}')}{|\mathbf{r}-\mathbf{r}'|}\,d\mathbf{r}' + \frac{\delta E_{xc}\left[\rho(\mathbf{r})\right]}{\delta\rho(\mathbf{r})} \tag{1.8}$$

With the Kohn-Sham potential V_{KS}, the effective Hamiltonian describes a non-interacting system, since all interactions have been included in V_{KS}. In addition, the electronic problem can now be tackled using a one-particle system, and the charge density becomes:

$$\rho(\mathbf{r}) = \sum |\phi_{\mathbf{i}}|^{\mathbf{2}} \tag{1.9}$$

The *exchange-correlation potential* is the variational derivative of the exchange correlation energy functional:

$$\upsilon_{xc}(\mathbf{r}) = \frac{\delta E_{xc}\left[\rho(\mathbf{r})\right]}{\delta\rho(\mathbf{r})} \tag{1.10}$$

The wave function $\phi_i(\mathbf{r})$ appearing in the Kohn-Sham equations describe electronic orbitals for the auxiliary non-interacting gas; they are the eigenstates of the effective single electron non-interacting problem and should not be considered as wave functions for the electrons of the real system. It is only the total energy and the electronic density $\rho(\mathbf{r})$ that have a physical meaning. However, usually the Kohn-Sham energy levels give good description of band structure of the real crystalline solids.

Although the exchange correlation energy, $\mathrm{E}_{xc}[\rho(\mathbf{r})]$, is well defined as a concept, its expression is not known precisely, and therefore an approximate expression is necessary to obtain the ground state energy $E[\rho(r)]$. The local density approximation (LDA) is a simple expression for $E_{xc}[\rho(\mathbf{r})]$ and it is based on the assumption that the real $E_{xc}[\rho(\mathbf{r})]$ is equal to the exchange correlation energy per electron of a homogeneous electron gas of the same density $\rho(\mathbf{r})$:

$$E_{xc}[\rho] = \int \rho(\mathbf{r})\epsilon_{xc}(\rho(\mathbf{r}))\,d\mathbf{r} \tag{1.11}$$

where ϵ_{xc} is the exchange-correlation energy per electron of a uniformly interacting electron gas of the same density, ρ. The LDA is strictly valid only if $\rho(\mathbf{r})$ is varying slowly, and many extensions exist which give improved accuracy for systems with localized electrons. For the LDA calculations

performed in this work, parameterizations developed by Barth-Hedin [12] and Vosko-Wilk-Nusair [168] were used.

To extend the density approximation to systems with more significant non-homogeneous densities, several techniques have been proposed. The most successful one is the generalized gradient approximation (GGA), where the real $E_{xc}[\rho(\mathbf{r})]$ is expressed as a functional of the density $\rho(\mathbf{r})$ and its gradient $\nabla\rho(\mathbf{r})$:

$$E_{xc}[\rho] = \int \rho(\mathbf{r})\epsilon_{xc}(\rho(\mathbf{r}))\,\mathbf{dr} + \int \mathbf{F_{xc}}[\rho, |\nabla\rho|]\,\mathbf{dr} \tag{1.12}$$

where F_{xc} is a correction. In principle this method should be called as LDA+GGA, but for short one uses only the term GGA. The GGA formalism gives a better description of inhomogeneous systems, like transition metals, and it significantly improves the binding energy, predicting good results also in the cases where LDA fails. GGA accounts specifically for density gradients that are neglected in pure LDA. For the GGA calculations performed in this work, the Perdew-Burke-Ernzerhof (PBE96) [129] parameterization for the exchange-correlation functional was used. The LDA and GGA methods are not accurate enough for a proper description, when on-site Coulomb correlation is very important. For such highly localized system containing such as f states and in some cases d states, LDA+U scheme is designed to give the self energy correction to localized states embedded in delocalized states.

1.1.2 Local spin density approximation (LSDA)

For magnetic materials, the LDA is extended to include spin-polarization, resulting in the local spin density approximation or LSDA. The $E_{xc}[\rho(\mathbf{r})]$ energy is a functional of both the up and down spin densities. With such distinction, the Kohn-Sham equations can be written as:

$$\left[-\frac{1}{2}\nabla^2 + V_{KS}^{\sigma}\right]\phi_i^{\sigma}(\mathbf{r}) = \varepsilon_{\mathbf{i}}^{\sigma}\phi_{\mathbf{i}}^{\sigma}(\mathbf{r}) \tag{1.13}$$

where V_{KS}^{σ}, $\upsilon_{xc}(\mathbf{r})$, $\rho^{\sigma}(\mathbf{r})$ and $\rho(\mathbf{r}$ are the spin extension of the previous quantities:

$$V_{KS}^{\sigma}(\mathbf{r}) = \upsilon(\mathbf{r}) + e^2\int\frac{\rho(\mathbf{r}')}{|\mathbf{r}-\mathbf{r}'|}\,d\mathbf{r}' + \frac{\delta E_{xc}\left[n^{\uparrow}, n^{\downarrow}\right]}{\delta\rho(\mathbf{r})} \tag{1.14}$$

$$\upsilon_{xc}^{\sigma}(\mathbf{r}) = \tfrac{\delta E_{xc}[n\uparrow, n\downarrow]}{\delta\rho^{\sigma}(\mathbf{r})}, \rho^{\sigma}(\mathbf{r}) = \textstyle\sum|\phi_{\mathbf{i}}^{\sigma}|^{\mathbf{2}}, \rho(\mathbf{r} = \sum_{\sigma}\rho^{\sigma}(\mathbf{r})$$

The imbalance between $n^{\uparrow}$ and $n^{\downarrow}$, producing the magnetization M = $n^{\uparrow}$ - $n^{\downarrow}$, is given by the exchange-correlation potential $\upsilon_{xc}^{\sigma}(\mathbf{r})$ which accounts for the different populations $n^{\uparrow}$ and $n^{\downarrow}$ by the derivative. In the local spin density approximation (LSDA), the exchange and correlation contributions are separated:

$$E_x^{LSDA}\left[\rho(\mathbf{r})\right] = \sum_{\sigma} \int \epsilon_{xc}^{hom}(\rho^{\sigma}(\mathbf{r}))\rho^{\sigma}(\mathbf{r})\,\mathbf{dr}, \tag{1.15}$$

$$E_c^{LSDA}\left[\rho(\mathbf{r}),\xi(\mathbf{r})\right] = \int \left[\epsilon_c^{U}(\rho(\mathbf{r})) + \mathbf{f}(\xi(\mathbf{r}))(\epsilon_{\mathbf{c}}^{\mathbf{P}}(\rho(\mathbf{r})) - \epsilon_{\mathbf{c}}^{\mathbf{U}}(\rho(\mathbf{r})))\right]\rho(\mathbf{r})\,\mathbf{dr}, \tag{1.16}$$

Where $\xi(\mathbf{r}) = \left|\mathbf{n}^{\uparrow}(\rho(\mathbf{r})) - \mathbf{n}^{\downarrow}(\rho(\mathbf{r}))\right| / \mathbf{n}^{\uparrow}(\rho(\mathbf{r})) - \mathbf{n}^{\downarrow}(\rho(\mathbf{r}))$ is the normalized magnetization, $f(\xi(\mathbf{r}))$ is a smoothing function, and ϵ_c^P and ϵ_c^U are proper functional representing the correlation energies for the spin-polarized and unpolarized systems, respectively [32, 125, 133].

1.1.3 Linear muffin-tin orbital (LMTO) highly localized basis functions

The Stuttgart LMTO program [85] is a fast and efficient tool for calculation of charge- and spin-self-consistent band structures, partial density of states, Fermi surfaces, and total energies. In addition, the program delivers tools for analyzing the electronic structure and chemical bonding such as orbital-projected band structures, crystal orbital Hamiltonian populations and electron localization functions. Forces and energy difference between structures can not be obtained accurately within the LMTO method because it is based on atomic sphere approximations (ASA), where it uses linearized numerical radial function in addition Hankel- and Bessel function expansions.

In LMTO, the orbitals are constructed from the muffin-tin (MT) approximation to the potential in the solid. A MT-potential is spherically symmetric inside non-overlapping spheres surrounding the atoms and constant in between. In the interstitial region, a linear muffin-tin orbital (LMTO) of the 1st generation is used, which is a spherical harmonic multiplied by the appropriate spherical Hankel or Neumann function, regular at infinity and with a fixed wavenumber. This envelope function is continued smoothly inside the spheres as the appropriate linear combination of spherical harmonics multiplied by radial Schrödinger-equation solutions, and their first energy derivatives, with the energy chosen at the center of interest. In interstitial space, empty spheres are taken and these spheres are allowed to overlap. This program uses downfolding technique, which is a useful way to reduce the size of an LMTO basis set. This helps in case of ghost bands because ghost bands are the feature of any linearization method. The full charge density must be used to calculate the total energy correctly. A full detail of the theory and computational techniques is given by Skriver [155].

1.1.4 Linear augmented plane wave method (WIEN2k)

Wien2k is based on linearized augmented plane wave (LAPW) [153] formalism and is one of the most accurate methods for performing electronic structure calculations for solids. Core states

are treated relativistically and valence states are treated either in a semi-relativistic way or with the second variational method including spin-orbit coupling.

In LAPW, the region of non-overlapping atomic spheres (centered at the atomic sites) is treated as a linear combination of radial functions times spherical harmonics $Y_{lm}(r)$, while in the interstitial regions, a plane wave expansion is used. Each plane wave is augmented by an atomic-like function in every atomic sphere. The solution of Kohn-Sham equations is expanded in this combined basis set of LAPWs according to the linear variation method. In order to improve linearization and to make possible a consistent treatment of semi-core and valence states in one energy window additional (reciprocal lattice vectors independent) basis functions (called local orbitals (LO)) can be added. In this method no shape approximations are used, thus it is frequently called a full potential method. It is well known that for localized electrons LDA and GGA methods are not accurate enough for a proper description of some of the strongly correlated systems. Thus other methods like LDA+U and Orbital polarization are also implemented in this program. In Wien2k [18] the effective Coulomb-exchange interaction ($U_{eff} = U - J$) is used for the LDA+U calculations [3]. This particular scheme is used in Wien2k to include double-counting corrections, however, it neglects multipole terms. It should be mentioned that the $+U$ was used on top of GGA rather than LSDA parametrization of the exchange-correlation functional. No significant differences were observed using one or the other of the parameterizations.

1.1.5 Full relativistic Korringa-Kohn-Rostocker (KKR) method

KKR is based on the solution of multiple scattering problem [49]. It is based on the Greens function formalism and is equivalent to LMTO. The LMTO method is the linearized version of the KKR method.
In addition, other methods are also used for various tasks.

1.2 Crystal structures of Heusler, cubic $C1_b$ and hexagonal compounds

1.2.1 Crystal structure of Heusler compounds

X_2YZ Heusler compounds crystallize in the cubic $L2_1$ structure (space group $Fm\bar{3}m$). In general X and Y atoms are transition metals and Z is a main group element. In some cases, Y is replaced by a rare earth element. The X atoms are placed on *8a* (1/4, 1/4, 1/4) and the Y and Z atoms on *4a* (0, 0, 0) and *4b* (1/2, 1/2, 1/2) *Wyckoff* positions, respectively. The cubic $L2_1$ structure consists of four inter-penetrating *fcc* sub-lattices, two of which are equally occupied by X.

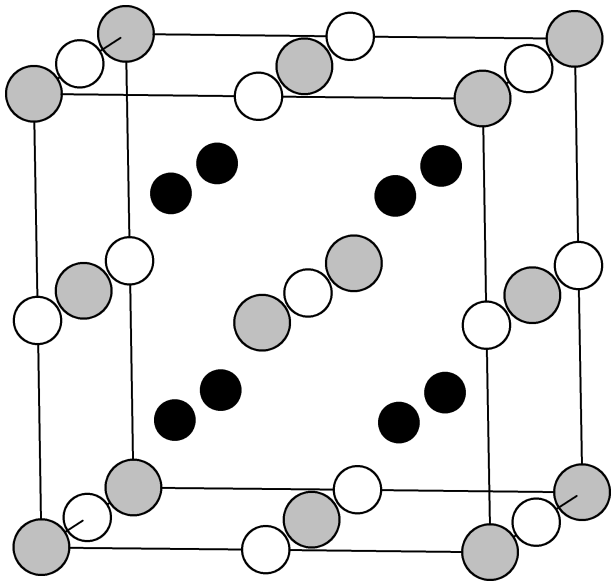

Figure 1.1: Structure of the X_2YZ Heusler compounds. X atoms (black) are at $(\frac{1}{4}, \frac{1}{4}, \frac{1}{4})$, Y (white) and Z (gray) atoms at $(\frac{1}{2}, \frac{1}{2}, \frac{1}{2})$ and $(0, 0, 0)$, respectively.

The two X *fcc* sub-lattices combine to form a simple cubic sub-lattice. The Y and Z atoms occupy alternatingly the center of the simple cubic X_2 sub-lattice resulting in a CsCl type super structure. The crystal structure of Heusler compounds is illustrated in Figure 1.1.

1.2.2 $C1_b$ crystal structure

Cubic XYZ compounds with $C1_b$ structure crystallize in the zinc blende structure type in space group ($F\bar{4}3m$) with a cubic cell parameter close to 6.0 Å. The least and most electronegative elements are Y at $(\frac{1}{2}, \frac{1}{2}, \frac{1}{2})$ and Z at $(0, 0, 0)$ forming a rock salt lattice. X are found at $(\frac{1}{2}, \frac{1}{2}, \frac{1}{2})$ in the centers of tetrahedra formed by Z, as well as by Y. Connecting X and Z reveals the stuffed zinc blende lattice of the $C1_b$ structure as displayed in Figure 1.2. There are other, equivalent descriptions of this structure, but this is the one used for this work, because it is closest to the description of the chemical bonding in this work.

1.2.3 Hexagonal analogues of cubic $C1_b$ compounds

At this point it is interesting to look at or think about hexagonal analogues of cubic $C1_b$ compounds (Figure 1.4). The prototype of this structure is known as LiGaGe (Space group $P6_3mc$). A number of experimental studies have been carried out on such ternary compounds. It was found that most of the compounds are reported in the disordered $CaIn_2$ structure type. Their correct

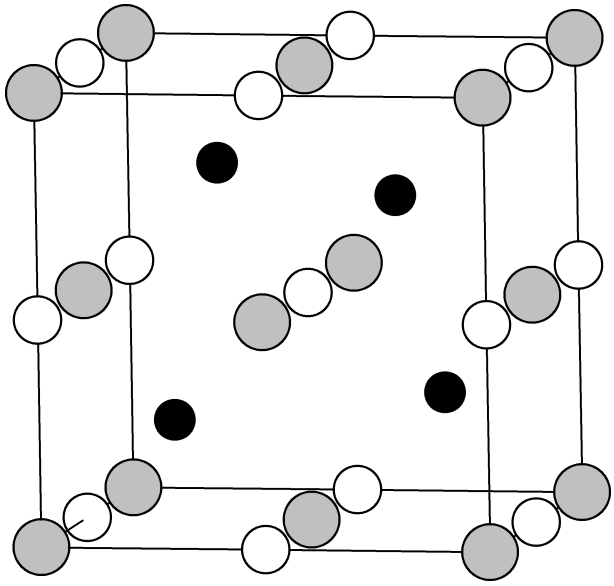

Figure 1.2: XYZ cubic $C1_b$ crystal structure in the $F\bar{4}3m$ space group. Z (gray) atoms are at the origin, X (black) at $(\frac{1}{4},\frac{1}{4},\frac{1}{4})$ and Y (white) at $(\frac{1}{2},\frac{1}{2},\frac{1}{2})$. Note the tetrahedral zinc blende (diamondoid) sublattice formed by X and Z.

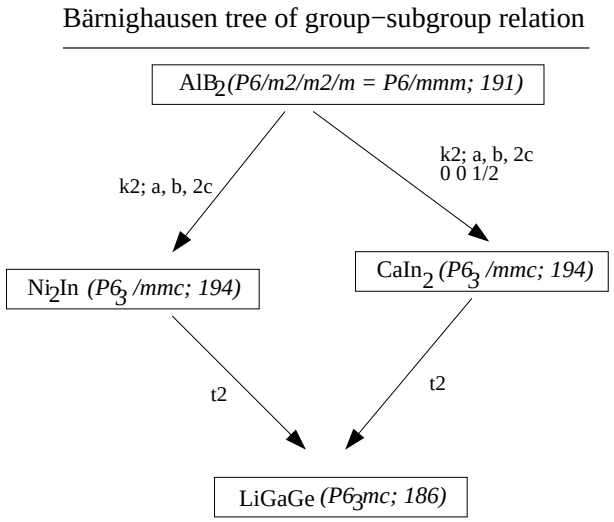

Figure 1.3: Bärnighausen tree of the group-subgroup relationships of the AlB_2 type and its distorted or ordered hexagonal derivatives. The indices of the *klassengleiche* (k), the *translationengleiche* (t) unit cell transformations and origin shifts are given. The number after t and k indicate the index of the reduction in symmetry.

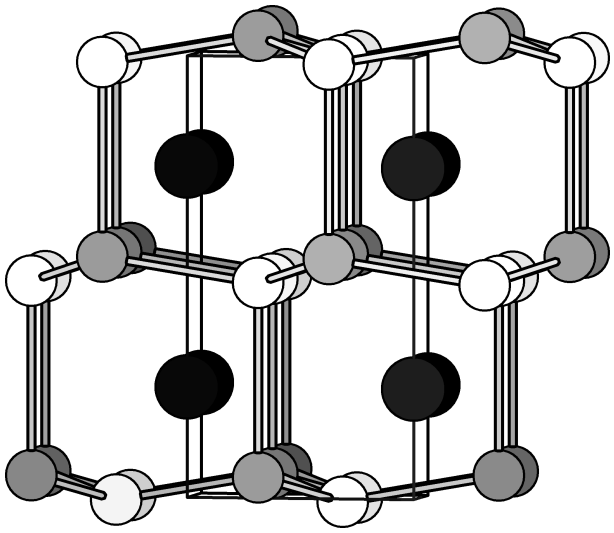

Figure 1.4: *REYZ* (LiGaGe) crystal structure in the $P6_3mc$ space group. Li (black) atoms are at $(0, 0, \frac{1}{4})$, Ga (gray) at $(\frac{1}{3}, \frac{2}{3}, \frac{1}{2} - z_1)$ and Ge (white) at $(\frac{1}{3}, \frac{2}{3}, \frac{1}{2} - z_2)$, the hexagonal wurtzite sublattice formed by Ga and Ge.

structure is the LiGaGe structure type, which belongs to a subgroup of $P6_3mc$. The corresponding Bärnighausen group-subgroup relation chart is shown in Figure 1.3. The LiGaGe crystal structure can be thought of as a stuffed wurtzite, with ionic Li^+ stuffing a more covalent $(GaGe)^{-1}$ lattice.

The crystal structure of *REYZ* is completely described by four parameters, the hexagonal cell parameters a, c, and the internal Y and Z positional parameters $(\frac{1}{3}, \frac{2}{3}, \frac{1}{2} - z)$ where z is different for Y and Z.

1.2.4 Crystal structure of GdAu*X* compounds

The intermetallic compounds GdAuIn, GdAuMg, and GdAuCd crystallize in the hexagonal ZrNiAl structure type. The experimental structural parameters that were used as starting values for the calculations are displayed in Table 1.1. In Figure 1.5, a projection of the GdAuMg structure together with the corresponding coordination polyhedra are displayed as an example. Both crystallographically independent Au sites have a trigonal prismatic coordination of Gd and X atoms, respectively. The two different trigonal prismatic building groups are shifted with respect to each other via half the translation period c. The trigonal prisms are capped by three additional atoms on the rectangular faces leading to a coordination number of 9, which is often observed for related intermetallics.

Table 1.1: Crystal structures of GdAuX (X = Mg, Cd, and In), space group $P6\bar{2}m$ (189): Gd in (x, 0, 0); Au1 in (1/3, 2/3, 1/2); Au2 in (0, 0, 0); X in (x, 0, 1/2)

Compound	a (Å)	b (Å)	x (Gd)	x (X)
GdAuMg	7.563	4.127	0.41250	0.7540
GdAuCd	7.701	3.960	0.4057	0.7421
GdAuIn	3.978	3.978	0.40635	0.7411

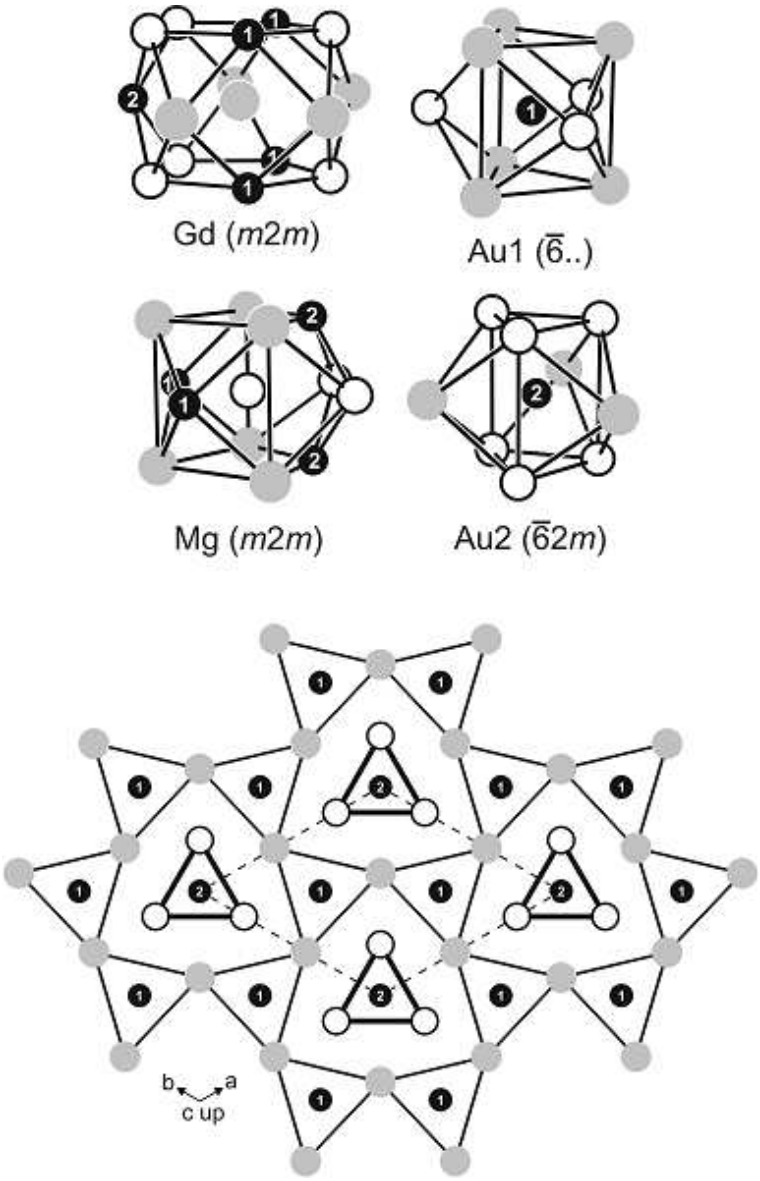

Figure 1.5: Projection of the GdAuMg structure onto the xy plane. All atoms are located on mirror planes at $z = 0$ (thin lines) and $z = 1/2$ (thick lines). Gd, Au, and Mg atoms are drawn as gray, black, and open circles, respectively. The trigonal prisms around the Au atoms are emphasized. The coordination polyhedra are drawn in the upper part and the site symmetries are indicated.

1.3 Structure of the thesis

This work is divided into two parts. Part one provides a broad overview of the main ideas and results of the Heusler compounds necessary to understand electronic structure and magnetic information in depth. In part two, bonding, electronic and magnetic properties of hexagonal analogues of cubic compounds are described.

The thesis is organized into 8 Chapters. Chapter 1 (this chapter) is an introductory chapter which outlines the development of the density functional theory (DFT), description of crystal structures and highlighting computational details for all the Chapters. In Chapter 2, results of ab-initio band structure calculations for X_2YZ Heusler compounds that have both X and Y sites occupied by transition metals and Z site by main group elements are presented. Chapter 3 deals especially with electronic correlation in Heusler compounds. Chapter 4 covers effects of disorder on half-metallic behavior of Co_2TiSn compound. In Chapter 5, a systematic examination of band gaps and the nature (covalent or ionic) of bonding in semiconducting 8- and 18-electron cubic $C1_b$ compounds is reported. Chapters 6, 7 and 8 are devoted to the search of hexagonal analogues of cubic $C1_b$ semiconductors and half-metals.

1.4 Calculational parameters used in different Chapters

- Chapter 2: The energy threshold between core and valence states was set to -81.6 eV. Various sets of muffin-tin-radii were taken to ensure almost nearly touching spheres. $R_{MT} \times k_{\max} = 7$ was used for the number of plane waves and the expansion of the wave functions was set to $l = 10$ inside of muffin tins. The self-consistent calculations employed a grid of 256 k points on a 20×20×20 mesh in the irreducible Brillouin zone. The LDA+U method [3] was used to account for on-site correlation at the transition metal sites. It was found that the spin-orbit interaction has only a weak influence on the half-metallic ferro-magnetism [115] in Heusler compounds, therefore it was neglected in the calculations. However the calculations include the mass velocity and Darwin terms.

- Chapter 3: The energy threshold between core and valence states was set to -81.6 eV. 2.3 a_{Bohr} was considered for the muffin-tin radii (R_{MT}) of all atoms, resulting in nearly touching spheres. 455 irreducible k points of a $25 \times 25 \times 25$ mesh were used for Brillouin zone integration. The number of plane waves was restricted to $R_{MT} \times k_{max} = 7$. Finally, the LDA+$U$ method [3] was used to account for on-site correlation at the transition metal sites. The used values of U for different transition elements are explained in Appendix B.

- Chapter 4: Wien2k is used to calculate electronic properties of Co_2TiSn. For comparison in

Co_2TiSn various methods were used: LMTO, SPKKR and full potential LMTO.

- Chapter 5: Density functional theory-based electronic structure calculations were performed using the full-potential Linear Augmented Plane Wave (LAPW) code WIEN2K [18] to optimize cell volumes of the different $C1_b$ compounds described here. Starting structures for LMTO calculations were obtained from the results of volume optimization using WIEN2K. Two important tools have been used to visualize the electronic structure of these phases. The crystal orbital Hamiltonian population (COHP) [48] enables the repartitioning of the density of states into regions which are pairwise bonding, non-bonding, or antibonding. The electron localization function (ELF) [14, 152] is a real-space indicator of the extent to which electrons are localized, and display a strong Pauli repulsion. The ELF therefore serves to locate bonding and non-bonding electron pairs in the real space of the crystal structure.

- Chapter 6: Wien2k and LDA+U scheme is used to calculate electronic properties of GdPdSb hexagonal compound.

- Chapter 7, Chapter 8: the TB-LMTO-ASA program was used to perform calculations of GdAuX (X = Mg, Cd, and In), EuAuAs, EuPdP and EuNiP using the atomic sphere approximation. All k-space integrations were performed using the tetrahedron method with 449 irreducible k points within the primitive wedge of the Brillouin zone. The basis sets consist of $6s$, $5d$ and $4f$ orbitals for Eu; $6s$, $6p$ and $5d$ for Au; $5s$, $5p$ and $4d$ for Pd; $4s$, $4p$ and $3d$ for Ni; $4s$ and $4p$ for As and $3s$ and $3p$ orbitals for P. Because of the valence instabilities of the compounds, which indicate a contribution of the europium $4f$ electrons to the bonding, it was necessary to treat these electrons as valence electrons.

For all calculations mentioned above, the energy convergence criterion was set to 10^{-5}. The charge convergence was monitored concurrently.

Chapter 2

Electronic and magnetic properties of the half-metallic, transition metal based Heusler compounds

2.1 Introduction

The Heusler compounds, as named after their discoverer [70] are ternary intermetallics with a 2:1:1 stoichiometry and the chemical formula X_2YZ. They usually consist of two transition metals (X, Y) and a main group element (Z). They first attracted the interest to the magnetism community when Heusler had shown that the compound Cu_xMn_yAl becomes ferromagnetic in the 211 form, even if none of its constituents is ferromagnetic by itself. However, it took three decades before their structure was explained to be an ordered compound [28].

The main interest during the first decades after their discovery was concentrated on Cu_2 and Mn containing compounds. Co_2 based compounds were synthesized and investigated in the 1970s [172]. Kübler *et al.* [102] recognized that the minority-spin state densities at the Fermi energy (ϵ_F) nearly vanish for Co_2MnAl and Co_2MnSn. The authors concluded that this should lead to peculiar transport properties in these Heusler compounds because only the majority density contributes at ϵ_F. At the same time, de Groot *et al.* [41] proposed the concept of the so called half-metallic ferromagnets (HMF) that are materials predicted to exhibit 100 % spin polarization at ϵ_F. This exceptional property would make the HMF ideal candidates for spin injection devices to be used in spin electronics [38].

The electronic structure plays an important role in determining the magnetic properties of

Heusler compounds and, in particular, for predicting half-metallic ferromagnetism. Band structure calculations must therefore be performed very carefully. The first attempt to calculate the band structure of some Co_2-based compounds (Co_2MnSn, Co_2TiSi and Co_2TiAl) did not indicate half-metallic ferromagnetism [80]. These calculations displayed a minimum of the minority density of states at ϵ_F. At that time, the calculations were based on spherical potentials, and the exchange-correlation potential of the local spin density approximation (LSDA) was used in a rather simple form [12, 69, 99, 168]. The first clear indication of half-metallic ferromagnetism in Co_2-based Heusler compounds was reported by Ishida *et al.* [81, 82] for Co_2MnZ and Ru_2MnZ (Z = Al, Si, Sn, Sb). Using full symmetry potentials, Mohn *et al.* [119] found the magnetic ground state of Co_2TiZ (Z = Al, Sn), but not a half-metallic state. Galanakis *et al.* [61] reported half-metallic behavior in various X_2YZ compounds, but not for the Co_2 compounds with Ti or Fe. The results were compatible with those found for the Mn compounds as calculated by Picozzi *et al.* [136] using the generalized gradient approximation instead of the pure LSDA. The generalized gradient approximation (GGA), as introduced by Perdew *et al.* [129, 130, 131, 132], accounts for gradients of the density that are absent in the pure LSDA parameterization of the exchange-correlation functional. Using spherical potentials and the GGA, a half-metallic state could not be verified for Co_2FeAl [4, 118]. A half-metallic ferromagnetic ground state was also found for the complete series $Co_2Cr_{1-x}Fe_xAl$, when the full symmetry potentials were used along with the GGA in the calculations [53]. This clearly indicates that to find the correct ground state, electronic structure for the Heusler compounds, one should require both the full symmetry potentials and the generalized gradient approximation. With this information, the properties of the reported transition metal based Heusler compounds were calculated in the present work using both the GGA and the full symmetry potentials. There are some cases where simple LSDA-GGA does not give the correct magnetic moments and ϵ_F may not fall into the minority gap. In such cases one can treat compounds in a special way using the LDA+U scheme as was shown in Ref. [96].

A systematic examination of the electronic and the magnetic structure of the Heusler compounds were carried out in this work. To study the effect of valence electron concentration on minority band gap, the density of states are compared for these compounds.

2.2 Non existing Heusler compounds, optimization and band structure

It is of interest to look first at those compounds which are missing from the series of Heusler compounds based on Co_2YZ [1]. The compound Co_2ScSi is not reported, and neither is Co_2CrSi.

[1] Appendix D provides a list of all Heusler compounds

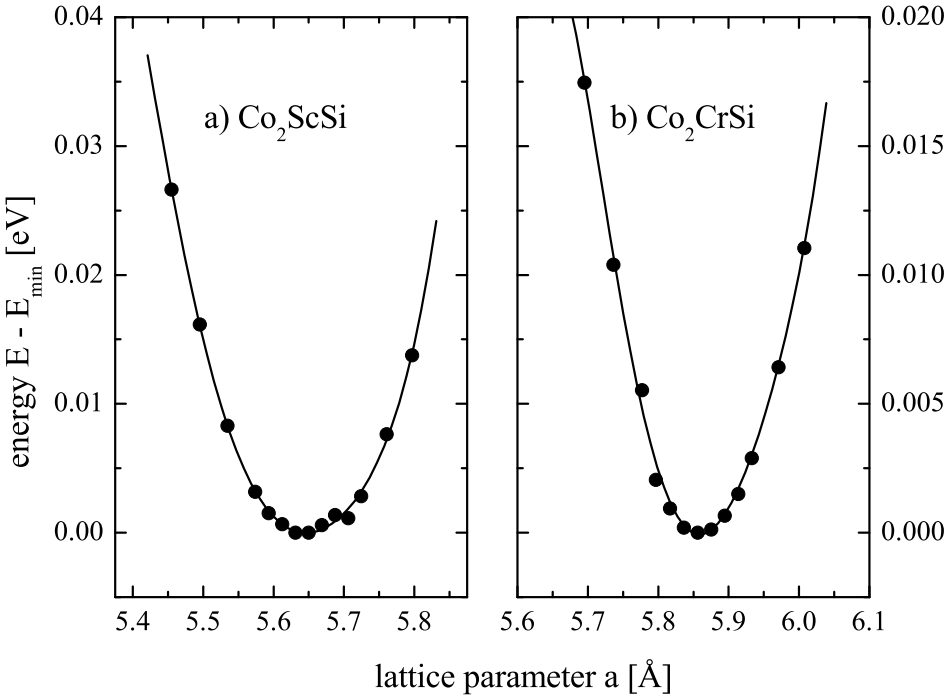

Figure 2.1: Optimization of the lattice parameter for Co_2ScSi and Co_2CrSi compounds. (The solid lines result from a polynomial fit.)

Within the FLAPW scheme, a structural optimization was performed for these two compounds. It was confirmed that the ferromagnetic configuration is lower in energy than the non spin-polarized case for both compounds. An anti-ferromagnetic spin arrangement of the Cr atoms in the cubic lattice showed to be energetically unfavorable with respect to the ferromagnetic arrangement in the Co_2CrSi compound. The results of the structural optimization are shown in Figure 2.1. The values of the optimized cell parameters are given in Table 2.2. The values of the calculated total spin magnetic moment and the elemental resolved moments are also given in Table 2.2. Both compounds exhibit large values of the minority band gap. The minority band gap is found to be 0.246 eV and 0.878 eV and the density of states at ϵ_F for majority states are 1.36 eV^{-1} and 2.9 eV^{-1} for Co_2ScSi and Co_2CrSi, respectively. The non-existence of Co_2CrSi and Co_2ScSi could be associated with the high peak in the density of states at ϵ_F.

The calculated total magnetic moments are 1 and 4 μ_B for Co_2ScSi and Co_2CrSi respectively. This is in good agreement with the Slater-Pauling like behavior [2]. The magnetic moment at the Co site is 0.6 μ_B in Co_2ScSi and 1 μ_B in Co_2CrSi, the remainder arises from the Y site (see Table 2.2. The majority density of states at ϵ_F is higher in Co_2CrSi as compared to the Co_2ScSi compound, as expected. The Cr compound exhibits a larger minority gap compared to the Sc compound.

Figure 2.2 shows the calculated DOS and band structures of both hypothetical compounds. These band structures can serve as common basis for the explanation of many Co_2-based Heusler compounds. They exhibit half-metallic ferromagnetic behavior with majority bands crossing ϵ_F. The band gap in minority states results in 100 % spin polarization for these compounds.

2.3 Results and discussions

In the half-metallic Heusler compounds discussed in this Chapter, the gap stays with few exceptions in the minority spin channel, whereas ϵ_F cuts through bands in the majority spin channel. For the majority spin channel, the position of ϵ_F is in the region of the d derived bands. These states are shifted to higher energies with respect to the corresponding minority spin states by the exchange splitting. Half metallic-behavior has been already predicted for a large number of Heusler compounds which are members of the series of ferromagnetic compounds. In general the Y atoms and in some cases also the X atoms carry the magnetic moments in these compounds. It is well known that the magnetic properties of these compounds depend sensitively on the degree of atomic order and on the valence electron concentration [61, 118]. The magnetic properties depend on whether the Z component is a member of the $3A$ or $4A$ maingroup, with the latter group having higher magnetic moments and Curie temperatures. Spin polarized electronic structure calculations indicate that the

[2] Slater-Pauling behavior for Heusler compounds is discussed in Appendix A

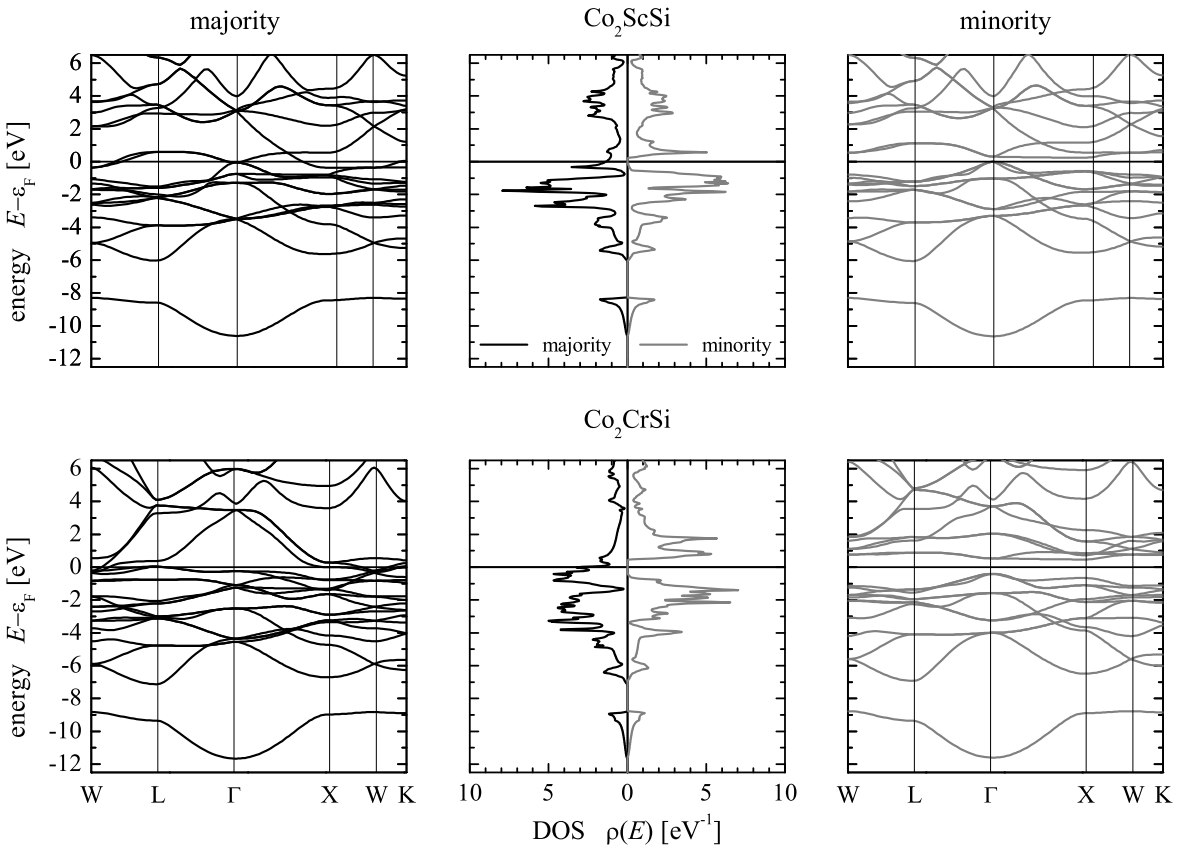

Figure 2.2: Band structure and density of states for the hypothetical compounds Co_2ScSi and Co_2CrSi.

Table 2.1: Magnetic moments of Co_2YZ Heusler compounds. The results of the calculations are compared to experimental values. All magnetic moments are given in μ_B. N_V is the number of valence electrons per formula unit (within parentheses). Total magnetic moments m_{Calc} are given per unit cell. m_X and m_Y are the site resolved magnetic moments on X and Y sites, respectively. Experimental values of the lattice parameter a and magnetic moments m_{exp} are taken mainly from references [25, 51, 173, 181], further additional references are given in the table.

			GGA			LDA+U			
compound (N_V)	a_{exp}	m_{exp}	m_{calc}	m_X	m_Y	m_{calc}	m_X	m_Y	Ref.
Co_2TiAl (25)	5.847	0.74	1.00	0.67	-0.18	1.0	0.84	-0.39	
Co_2TiGa (25)	5.85	0.75	1.00	0.63	-0.15				
Co_2TiSi (26)	5.743	1.65	2.00	1.03	-0.02	2.0	1.16	-0.18	
Co_2TiGe (26)	5.807	1.59	1.97	1.05	-0.06				
Co_2TiSn (26)	6.077	1.96	1.96	1.08	-0.07				
Co_2VAl (26)	5.722	1.95	2.00	0.94	0.218	2.0	1.15	-0.09	
Co_2VGa (26)	5.779	1.92	2.01	0.97	0.16				[29]
Co_2VSn (27)	5.96	1.21	3.03	1.10	0.86				
Co_2VSi (27)	5.657		3.00	0.789	1.09	3.00	1.20	0.69	[65]
Co_2CrAl (27)	5.727	1.55	3.00	0.83	1.47	3.01	0.79	1.70	
Co_2CrGa (27)	5.805	3.01	3.05	0.76	1.63				[164]
Co_2CrIn (27)	6.060	1.10	3.20	0.67	1.98				[175]
Co_2MnAl (28)	5.749	4.04	4.04	0.76	2.745	4.28	0.73	3.17	
Co_2MnGa (28)	5.767	4.05	4.12	0.75	2.78				
Co_2MnSi (29)	5.645	4.9	5.00	1.00	3.00	5.0	0.979	3.29	
Co_2MnGe (29)	5.749	4.93	5.00	1.02	3.06				
Co_2MnSn (29)	5.984	5.08	5.03	0.97	3.23				
Co_2FeAl (29)	5.73	4.96	4.98	1.23	2.78	5.00	1.22	2.97	
Co_2FeGa (29)	5.737	5.04	5.02	1.20	2.81				[164]
Co_2FeSi (30)	5.64	6.00	5.59	1.40	2.87	6.00	1.50	3.14	[177]
Co_2FeGe (30)	5.738	5.90	5.70	1.42	2.92				

moments are predominantly of $3d$ origin. The density of state (DOS) of the minority states is almost zero at ϵ_F whereas the majority d density can have a peak or a valley close to this energy. It is filling and emptying of this peak that is assumed to produce the change in the size of the magnetic moment and the Curie temperature. In order to verify this, and to obtain further evidence for half-metallic behavior, a series of calculations for X_2YZ compounds was performed and is presented in the following.

2.3.1 Magnetic properties

Starting with the Co_2-based compounds, all the information about the atom-resolved, total spin moments, the experimental lattice parameters, the experimental and the calculated magnetic moments are summarized in Table 2.1. For each compound, calculations were carried out using the experimental lattice parameters, and most of them exhibit at least nearly HMF type character (either gap in the minority or majority states). This is clear from Figures 2.5 and 2.6 where the

spin projected density of states (DOSs) of nine selected compounds are shown (note: details will be discussed later). Those will be used as representatives of the compounds as listed in Table 2.1. These nine compounds are Co_2YZ Heusler compounds with Y = Ti, V, Cr, Mn, Fe and Z = Al, Ga and Si. By making such a choice, one covers both a range of electronically different kinds of Y and Z atoms with Co atoms at the X site. In most of the cases the total spin magnetic moment is exactly integer as expected for a half-metallic system. The experimental magnetic moments are also given in Table 2.1 for comparison with calculations. In most cases, the calculated magnetic moments are in good agreement with the experimental results. m_{cal} is the calculated total spin magnetic moment of the compound, which is the combination of the moments at X site (2 times), the Y sites, the Z sites and the moment of the interstitial between the sites. That is the reason why m_X and m_Y alone are not summing up to result in m_{cal}. The missing or excess of the total moment is found at the Z sites and in the interstitial between the sites. Exceptions from experimental values appear for compounds carrying a high magnetic moment like Co_2FeSi, Co_2FeGe etc. Inspection of the magnetic moment revealed that the Co and Y atoms possess high spin magnetic moments in this series of compounds. In case of small magnetic moment compounds, the Co atoms contribute most to the moment compared to the compounds with large magnetic moments. While going from the low to the high magnetic moment side, the Y atoms contribute an increasing moment in these compounds.

In all reported compounds, the Z atoms carry a negligible magnetic moment, that does not contribute much to the overall moment. In most of the compounds it is aligned anti-parallel to the X and Y moments. It emerges from the overlap of the electron wave functions.

There are some cases where simple LSDA-GGA does not give the correct magnetic moments, and ϵ_F may not fall into the minority gap. Thus the system no longer exist as magnetic half-metal. In such cases one can treat them in a special way using the LDA+U scheme. The magnetic moment of most of the compounds in this series exhibits a linear behavior with the number of valence electrons and follows the Slater-Pauling rule [126, 156]. Note that there are some deviations from this trend: for example, Co_2FeAl, Co_2VGa, Co_2TiGa and Co_2ScSi.

Inspecting other transition metal based Heusler compounds not based on Co_2, one finds that compounds with magnetic moments above the expected Slater-Pauling value are X = Fe based. Those with lower values are either X = Cu or X = Ni based. Where Ni based compounds exhibiting higher moments compared to the Cu based compounds at the same number of valence electrons. Moreover, some of the Cu or Ni based compounds are non ferromagnetic, independent of the number of valence electrons. Besides Mn_2VAl, only compounds containing both, Fe and Mn, were found to exhibit HMF character with magnetic moments according to the Slater-Pauling rule (discussed in Appendix A).

Table 2.2: Optimized lattice parameters (in Å), total magnetic moments, and atom resolved magnetic moments (in μ_B). $\Delta(a)$ is the change of the lattice parameter (in %) with respect to the experimental value

Compound	a_{opt}	$\Delta(a)$	m_{tot}	m_X	m_Y
Co_2ScAl	5.960		0	0.00	0.00
Co_2TiAl	5.828	-0.3	1	0.62	-0.13
Co_2VAl	5.754	+0.6	2	0.94	0.23
Co_2CrAl	5.708	-0.3	3	0.80	1.52
Co_2MnAl	5.695	-0.9	4	0.77	2.67
Co_2FeAl	5.706	-0.7	5	1.22	2.79
Co_2ScSi	5.865		1	0.60	-0.10
Co_2TiSi	5.760	+0.3	2	1.03	-0.02
Co_2VSi	5.688	+0.5	3	1.10	0.80
Co_2CrSi	5.647		4	1.00	2.03
Co_2MnSi	5.643	0	5	1.06	2.99
Co_2FeSi	5.634	0	5.55	1.39	2.85

Dependence of magnetic behavior on valence electron concentration

In this subsection, the magnetic behavior of different compounds with different valence electron concentrations is discussed. The structure of two series of compounds Co_2YAl and Co_2YSi (Y = Sc, Ti, V, Cr, Mn, Fe), were first geometrically optimized. The energy minimum which defines the optimal a was taken as input for further calculations. The optimized lattice parameters were found to be in average within 1% of the experimentally obtained lattice parameters. This implies that the electronic structure is independent of the use of the experimental or optimized lattice parameters. Differences in the element specific magnetic moments are mainly due to the different Muffin-tin radii that changes with a. In the two cases, Co_2MnSi and Co_2FeSi, the optimized lattice parameter was found to match the experimental one. The optimized lattice parameters are given in Table 2.2 together with the total and element specific magnetic moments for Co and Y sites.

In the Co_2YAl series, the magnetic moment at the Co site first increases and then stays at about 1 μ_B, while the magnetic moment at the Y site starts from small negative values and then increases linearly with the valence electron concentration (see in Figure 2.3). In all compounds, the magnetic moment at the Al and Si sites is very small and anti-parallel to Co. It seems that the moment of Co is fixed at about $1\mu_B$ and compels the Y moment to result in the overall magnetic moment according to the valence electron concentration.

The magnetic moment at the Co site stays at about 1 μ_B from Ti to Mn and diverges from this value only for Sc and Fe containing compounds. The magnetic moment at the Y site increases linearly from Ti to Mn compounds such that the total magnetic moment follows the Slater-Pauling rule. With an increasing number of valence electrons, the magnetic moment increases linearly up to Mn and after that it deviates from this trend. At least for high magnetic moment compounds one

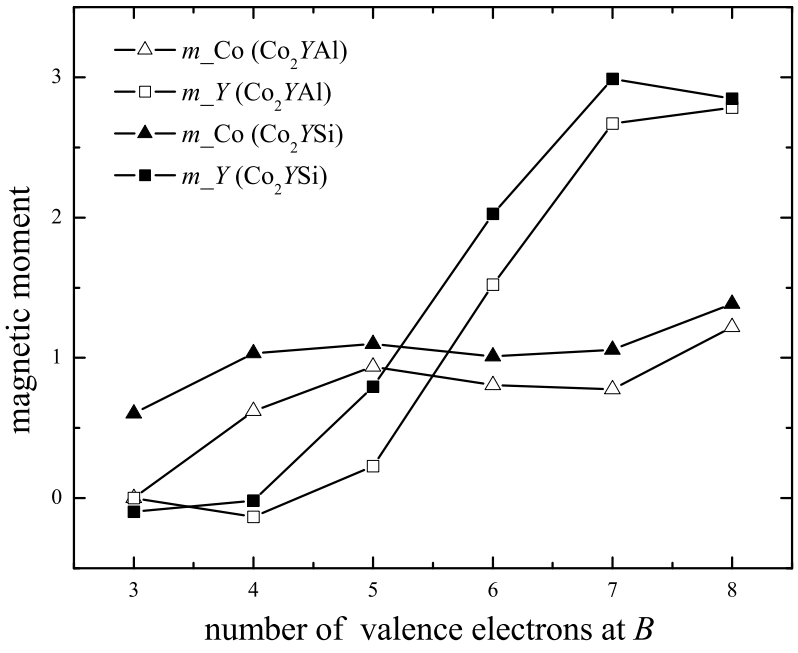

Figure 2.3: Evaluation of the magnetic moments of Co and Y atoms in the series Co_2YZ (Z = Al, Si).

Table 2.3: Co_2YZ compounds with minority band gaps including ϵ_F. E_{min} and E_{max} are the values of the minimum energy of the conduction band and the maximum energy of the valence band. The band gap ΔE is the difference between these external energies. All energies are given in eV. $N_\uparrow(\epsilon_F)$ is the density of states at ϵ_F for majority electrons.

	GGA				LDA+U		
Compound	$E_{max}(\Gamma)$	E_{min} (X)	ΔE	$N_\uparrow(\epsilon_F)$	E_{max}	E_{min}	ΔE
Co_2TiAl	-0.24	0.215	0.456	1.37	-0.206	0.914	1.120
Co_2TiSi	-0.606	0.179	0.785	0.986	-0.583	0.632	1.215
Co_2TiGe	-0.401	0.194	0.595	0.93			
Co_2TiSn	-0.222	0.282	0.504	1.05			
Co_2VGa	-0.142	0.047	0.189	1.52			
Co_2VSn	-0.397	0.151	0.548	5.34			
Co_2CrAl	-0.118	0.63	0.748	4.84	0.071	1.39	1.319
Co_2MnSi	-0.292	0.506	0.798	1.27	0.007	1.307	1.300
Co_2MnGe	-0.048	0.533	0.581	1.29			
Co_2VSi	-0.886	-0.067	0.072	3.50	-0.905	0.138	1.04
Co_2FeAl	-0.138	-0.027	0.111	0.87	0.022	0.811	0.789
Co_2TiGa	0.06	0.216	0.210	1.44			
Co_2FeGa	0.086	0.107	0.021	0.88			

should consider on-site electron-electron correlation. In the Co_2YSi series, the trends are the same as in the previously discussed Al series. The only difference is the detail of the magnetic moments at Co and Y atoms. The increase of the magnetic moments are attributed to the rearrangement of the electrons (discussed briefly in the next section). In summary the Co atoms contribute 1 μ_B and *drives* the properties of the Y atoms to have a magnetic moment according to the number of valence electrons of the compounds. The properties of the Co_2YZ compounds are dominated by the nature of the Co atoms which force the *extent of localization* of the electrons and the resulting magnetic moment at the Y site.

2.3.2 Electronic structure and density of states

As seen in the previous subsection, the Co_2YZ compounds can be distinguished in two classes, one with small magnetic moments (less than 3 μ_B) and the remainder ones with high magnetic moments. The class of compounds with small magnetic moments will be called "low-m" and the one with high magnetic moments "high-m". In the next subsection, the evaluation of the band gap in the minority states is discussed.

Band gap

Tables 2.3 summarizes the results calculated for the minority band gap of the Co_2YZ compounds with a clear gap at ϵ_F. All of the listed compounds show a gap along $\Gamma - X$ *i.* e. in the Δ-direction (see detail in Appendix C). The listed compounds (except the four shown at the

(a)

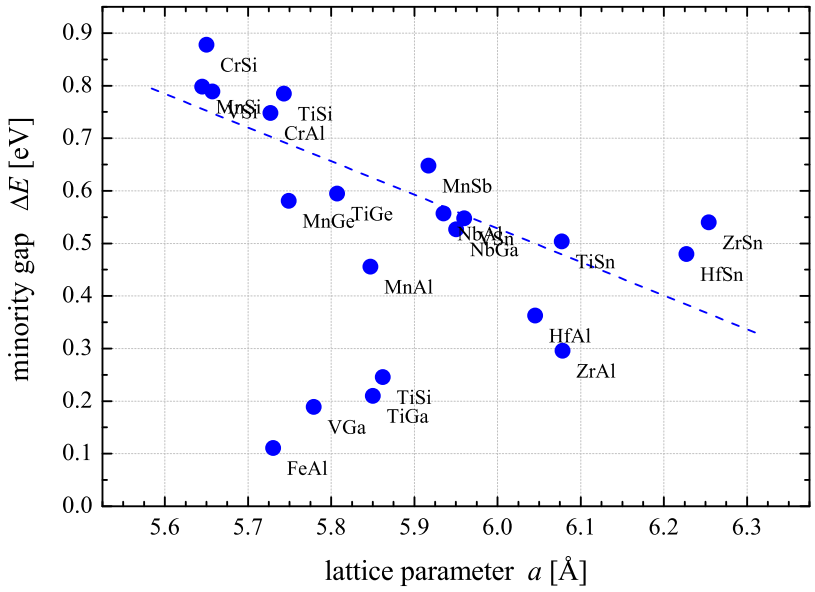

(b)

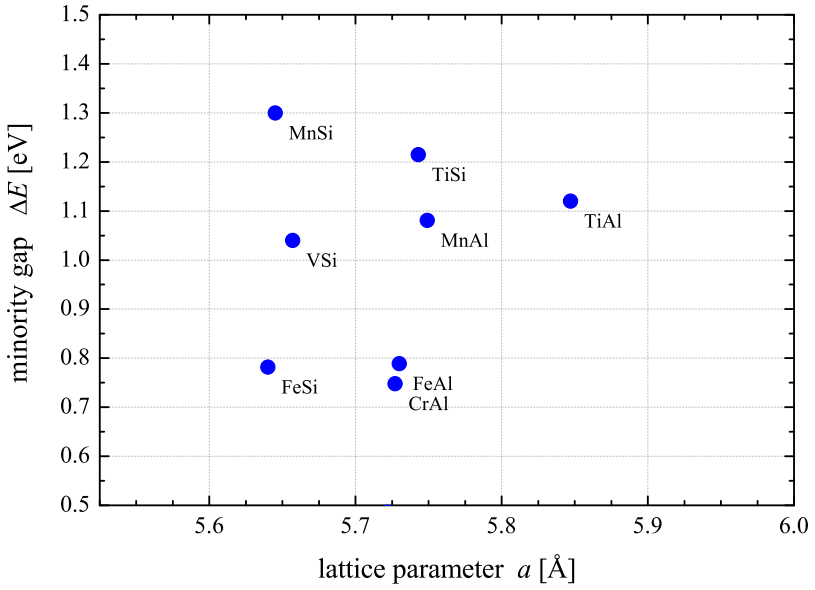

Figure 2.4: Minority band gap in Co_2 based half-metallic ferromagnets within (a) GGA and (b) LDA+U. Shown is the size of the gap (ΔE) versus lattice parameter. The line is drawn to guide the eye.

Table 2.4: Band gaps in the minority states of Co_2YZ compounds with ϵ_F outside of the gap. In this class of compounds the minority gap does not include ϵ_F. The compounds are grouped for the cases where ϵ_F from GGA calculations is below or above the gap. (For quantities see Table 2.1)

	GGA					LDA+U		
Compound	E_{max}	E_{min}	ΔE	$N_\uparrow(\epsilon_F)$	$N_\downarrow(\epsilon_F)$	E_{max}	E_{min}	ΔE
Co_2CrGa	0.203	0.628	0.425	2.8	0.2			
Co_2CrIn	0.450	0.612	0.162	2.35	0.5			
Co_2MnAl	0.256	0.882	0.626	1.05	0.2	0.424	1.505	1.081
Co_2MnGa	0.362	0.731	0.369	1.7	0.34			
Co_2MnSn	0.183	0.594	0.411	1.22	0.16			
Co_2VAl	-0.357	-0.119	0.238	1.6	0.03	-0.414	0.072	0.486
Co_2FeSi	-0.735	-0.589	0.146	2.7	0.71	-0.81	-0.028	0.782
Co_2FeGe	-0.517	-0.43	0.087	2.3	0.74			

bottom of the table) exhibit a gap at ϵ_F and behave like HMF within GGA. The band gap values for some of the compounds using electronic correlation are also listed in the Table 2.3. It is clear that electron-electron correlation may create or destroy the gap or shift ϵ_F outside the gap.

As one approaches towards high magnetic moment compounds, there is a reduction in the density of states of the majority spin states at ϵ_F. Only few compounds have a high majority DOS at the ϵ_F whereas, the remainder have small values. For some high magnetic moment compounds it is completely different. Instead of having a high majority DOS they have only a small DOS. Already the GGA calculations reveal the small DOS at ϵ_F. The important conclusion one can draw at this point is that the LSDA-GGA does not estimate the gap and magnetic moment of these compounds correctly and as a result, half-metallic behavior is not obtained.

The minority band gaps of Co_2YZ compounds, where ϵ_F lies outside of the gap within GGA are shown in Table 2.4. Their DOS values at ϵ_F for majority and minority states are also listed in the table.

The lattice parameter dependence as a function of the size of the minority gap is displayed in Figure 2.4 (a) GGA and (b) LDA+U. There is a tendency that larger lattice parameter of the compounds lead to smaller band gaps. This trend cannot be used quantitatively, but only as a starting guess to search for good candidates for HMF materials.

Low m compounds

The DOS for the low m compounds Co_2TiAl, Co_2TiSi, Co_2VAl and Co_2VSi are displayed in the different panels of Figure 2.5. The upper part of each panel displays the majority spin states and the lower one the minority spin states.

The large splitting of the minority states in the Co_2YSi compounds is remarkable on going from lower to higher valence electron concentration. This behavior is expected for such compounds due to the higher moments at Co and Y sites compared to Co_2TiAl and Co_2TiSi. The majority

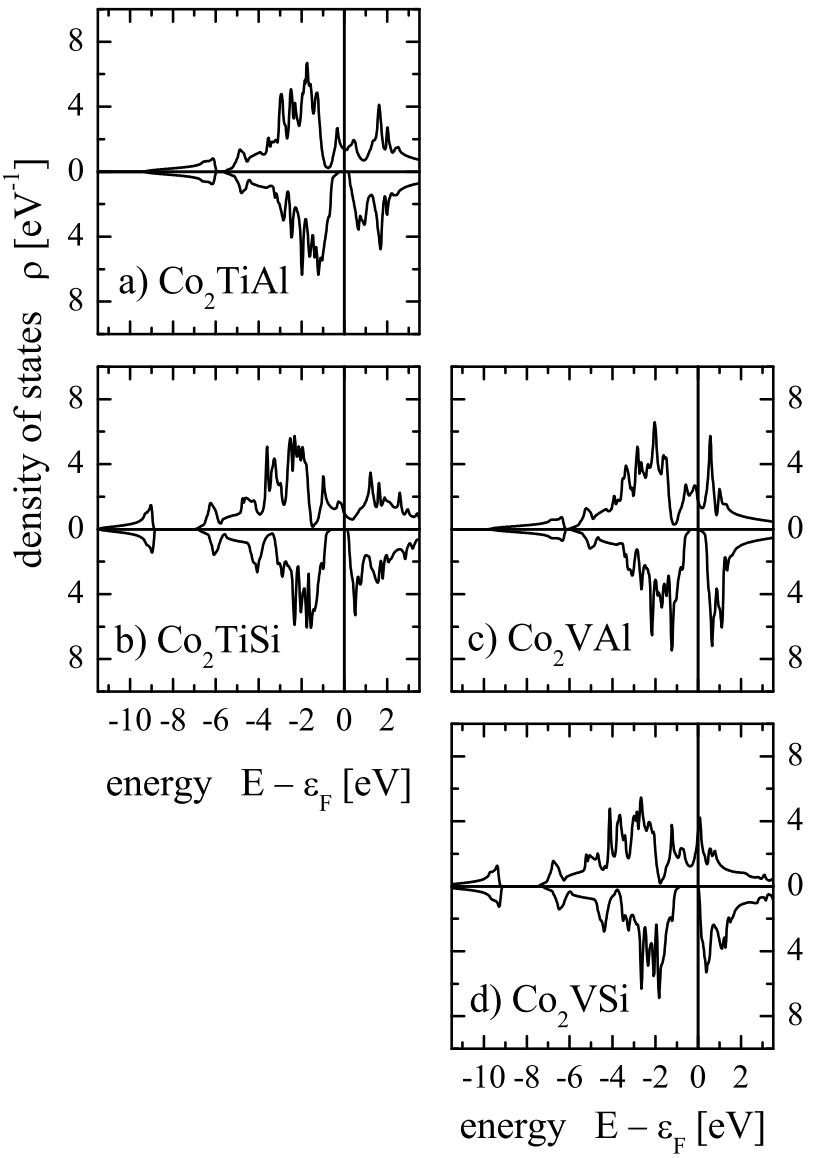

Figure 2.5: Density of states of selected low m Co_2YZ compounds. Shown are the spin resolved DOS for compounds with Y = Ti, V and Z = Al, Si. (Note: the upper and lower parts of the panels show the majority and minority DOS for each compound, respectively.)

and minority d states spread up to -6 eV below ϵ_F in Co_2TiAl. For Co_2TiSi and Co_2VSi, the band width is almost the same and the density of the d states spreads up to -7 eV below ϵ_F due to the larger crystal field splitting as well as larger exchange splitting in both compounds. Indeed, in all four compounds the states at and close to ϵ_F are strongly spin polarized and all four systems exhibit a gap in the minority states. The spin polarization is found to be 100 % which characterizes the systems to be half-metallic.

High m compounds

In the next step, the six compounds Co_2YZ (Y = Cr, Mn, Fe and Z = Al, Ga) with high m were chosen. The DOS for these compounds are displayed in the various panels of Figure 2.6. The situation is somewhat different from the low m (as explained in the previous subsection). All listed compounds exhibit almost the same band width. However, there are distinct differences in the shapes of the states. There are some minority states appearing near ϵ_F, which cause the decrease of the total spin polarization for these compounds. Again there is a larger splitting in case of Co_2FeGa, due to Co and Fe atoms which carry the high magnetic moment. The FLAPW spin polarized results predict an *approximate* half-metal behavior. The most interesting conclusion that can be drawn from the DOS of these Co_2YZ based Heusler compounds is that the states at and near ϵ_F are strongly spin polarized and the systems indeed exhibit half-metallic ferromagnetism. There are changes in the DOS while going from the low m compounds to the high m compounds with a gap in the minority states and decrease in the contribution from majority states just at ϵ_F.

It is very often observed that the Ga containing Heusler compounds based on Co_2 have a smaller gap at ϵ_F as compared to others. These compounds may have some minority states appearing close to ϵ_F.

High-m compounds and LDA+U

In this subsection, the influence of correlation on the electronic structure of various compounds is discussed and the results are displayed in Tables 2.1, 2.3 and 2.4 (correlation will be discussed in detail in Chapter 3). Out of these, only the band structures of the two compounds Co_2FeAl and Co_2FeGa will be discussed. These two compounds are selected as an example. The spin-resolved density of states for Co_2FeAl and Co_2FeGa that are calculated using the LSDA and LDA+U approximations are shown in Figure 2.7. The semi-empirical values corresponding to 7.5% of the atomic values of the Coulomb-exchange parameter (U_{eff}) [3](see Ref. [96]) have been used for all given examples as reported previously [96]. In particular, the values for U_{eff} were set to U_{Co} = 1.90 eV and U_{Fe} = 1.795 eV. Both compounds exhibit a very small minority band gap at

[3] U_{eff} values are given in Appendix B using Cowan's program

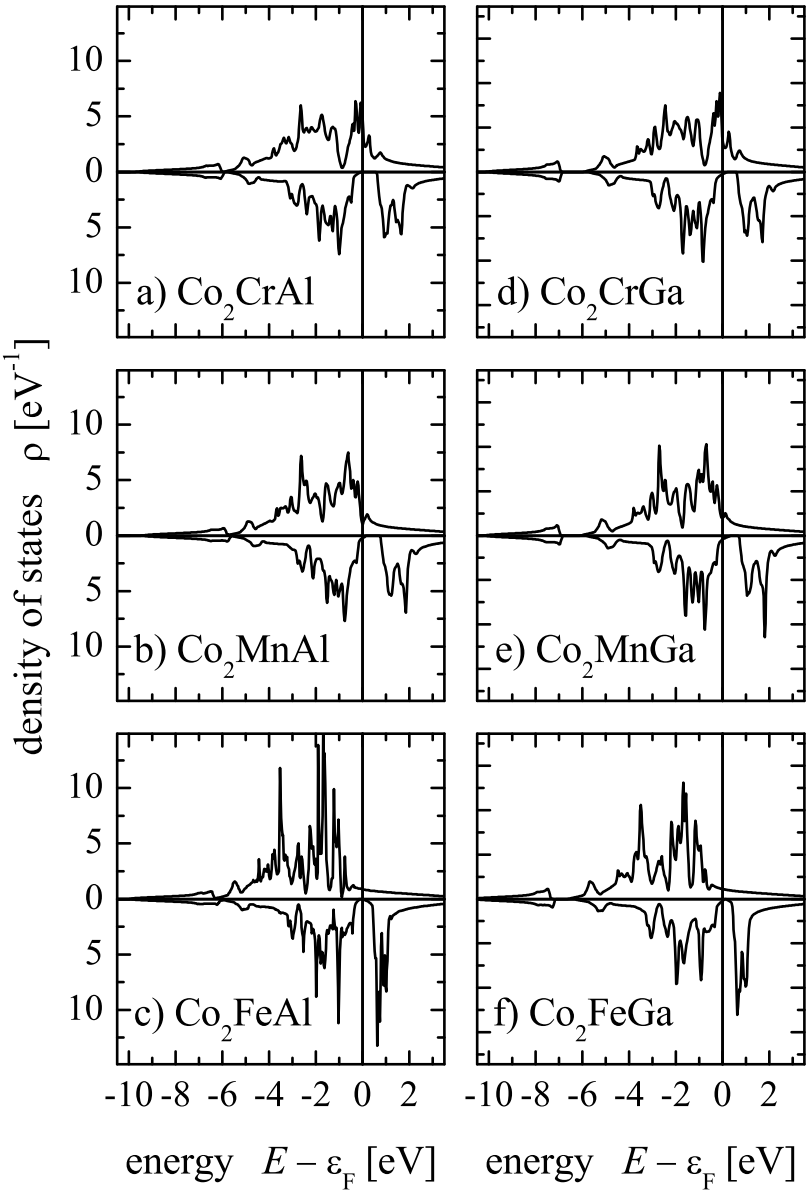

Figure 2.6: Density of states for low to high m Co_2YZ compounds. Shown are the spin resolved DOS for compounds with Y = Cr, Mn, Fe and Z = Al, Ga. (Note: upper and lower parts of the panels show for each compound the majority and minority DOS, respectively.)

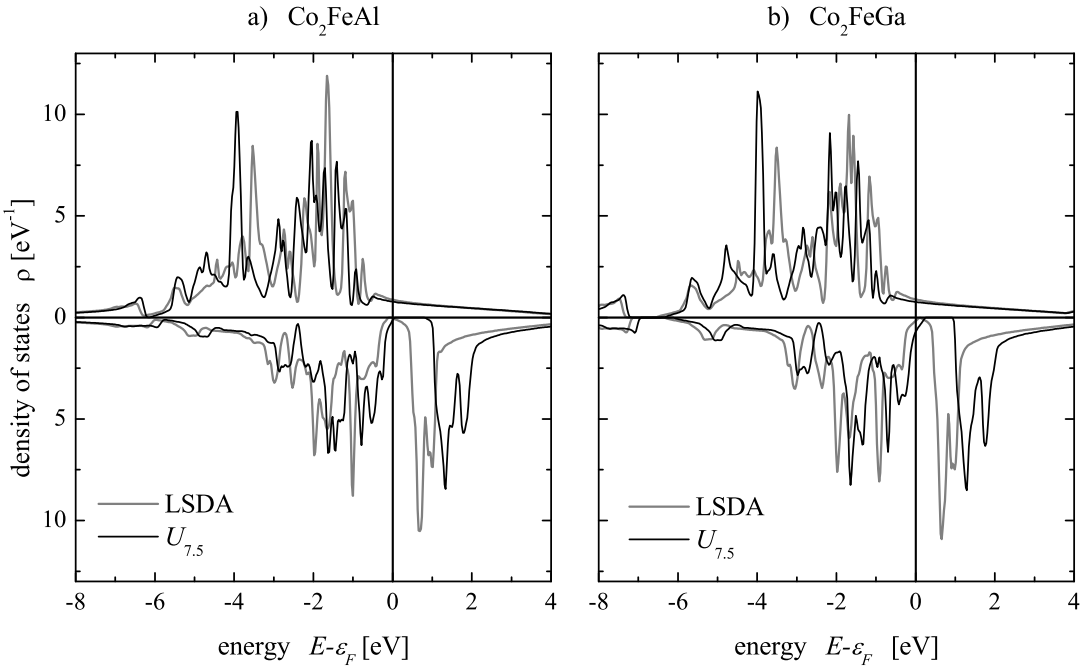

Figure 2.7: Spin-resolved density of states for Co_2FeAl and Co_2FeGa. Black lines indicate the DOS using the LDA+U with $U_{7.5}$ for Co_2FeAl (a) and $U_{7.5}$ for Co_2FeGa (b). Grey lines indicate the results from the LSDA. The upper and lower parts of the plots display the majority and minority states, respectively. (See the text for the particular values of U at the different sites.)

ϵ_F without U_{eff}. However, it becomes large when LDA+U is used in the calculations (for band gaps see Tables 2.3 and 2.4). It should be noted that the high m compounds are very sensitive to electron-electron correlation. In some cases it is required to explain their electronic and magnetic properties. The details of the change in the electronic structure are discussed in Chapter 3.

In most of the Co_2-based Heusler compounds, the minority gap becomes large with inclusion of U (see Tables 2.3 and 2.4). The ϵ_F shifts to inside or outside the gap. For the particular case of Co_2CrAl, ϵ_F falls outside the gap with U.

Distribution of the electrons

On careful examination of the magnetic moments on the Co sites in both series (Co_2YZ with Z = Al and Si), one finds that the Co site is carrying an average of 0.8 μ_B (Al series) and 1.0 μ_B (Si series). At this point it is not clear why the magnetic moment of Co is changing with exchange of Al by Si. Thus the question arises how Z affects the overall magnetic moment without directly contributing to it? To check this, it is necessary to look at the electron distribution of the system. A systematic study has been carefully carried out for these two series of compounds.

The total magnetic moment in the series is defined by the number of unoccupied d electrons in the majority and minority states. The total number of d electrons at the Co site is about 7.5 including majority and minority electrons (see Figure 2.8). The Co d states are split up into two states for majority and minority spin. The majority and minority spin d states are almost constant and contain 4 and 3.5 electrons, respectively. Their values are nearly constant and do not change much if going from Ti to Mn. This is one reason why the magnetic moment of Co is fixed at about 1 μ_B.

The distribution of the d electrons in majority and minority states for the Y element is shown in Figures 2.8(c, d). It is clear that filling of both majority and minority d electrons increases in parallel up to V and thereafter the electrons start to fill more majority states as compared to minority states. Al and Si contribute very less to the d states and in-fact they do not contribute directly to the overall magnetic moment.

Effect of different Z

To check how the different Z elements effect the magnetic moments and the number of electrons in d states, the Co_2YSi compounds with Y = Sc, Ti, V, Cr, Mn, Fe were studied in the same way as the Co_2YAl compounds. It was found that the trends are the same as for the Co_2YAl compounds.

At this point the question arises why the total magnetic moment increases by 1 μ_B when Al is replaced by Si. Taking simple examples like Co_2MnAl and Co_2MnSii, the first compound has

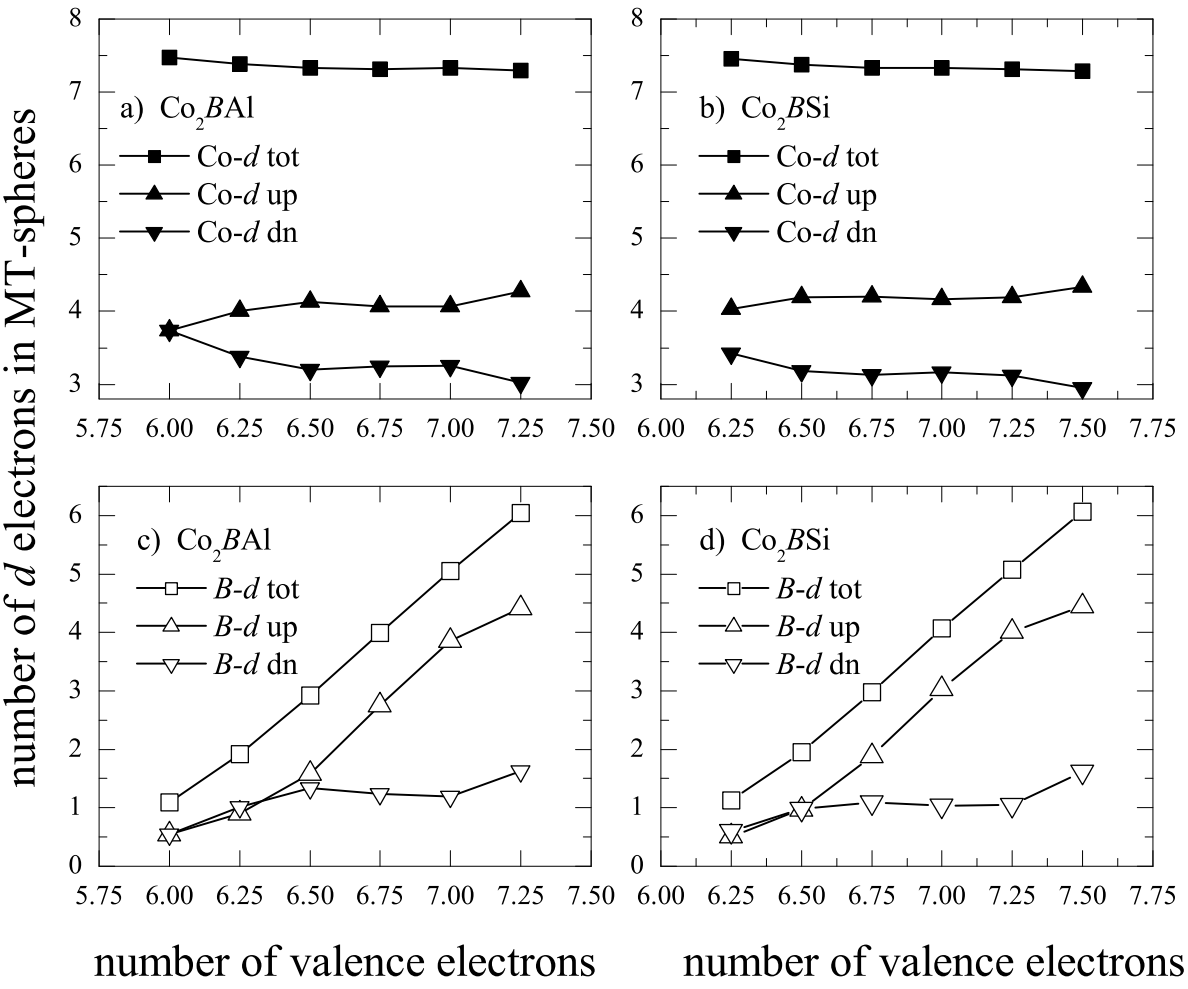

Figure 2.8: Total number of valence d electrons present in spin up and spin down channel for Co and Y sites in Co_2YAl and Co_2YSi; (Y = Sc, Ti, V, Cr, Mn, and Fe) with the average number of valence electrons.

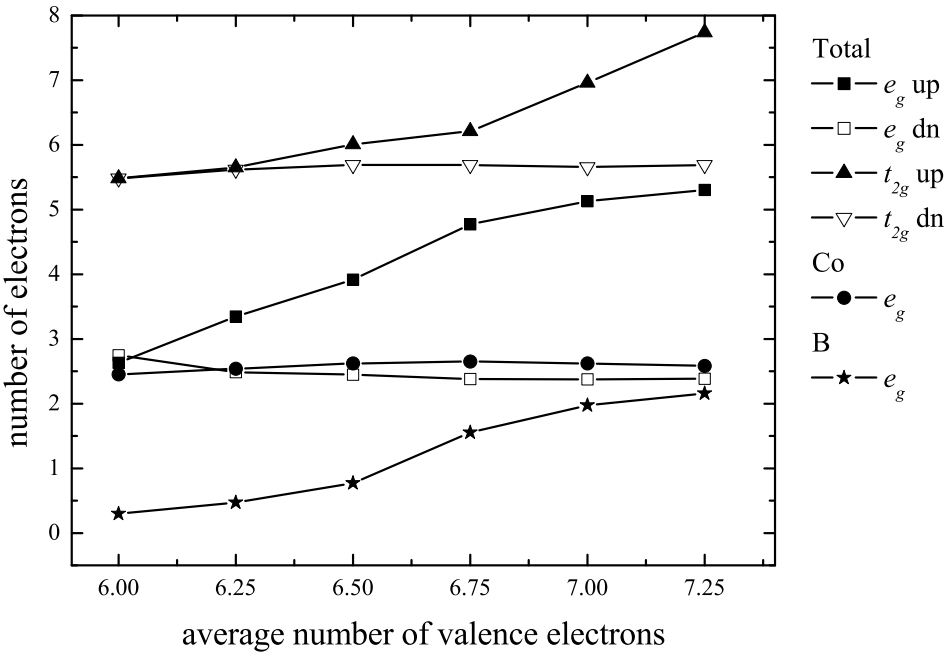

Figure 2.9: Distribution of the electrons in symmetry distinguished states (e_g and t_{2g}) in Co_2YAl compounds.

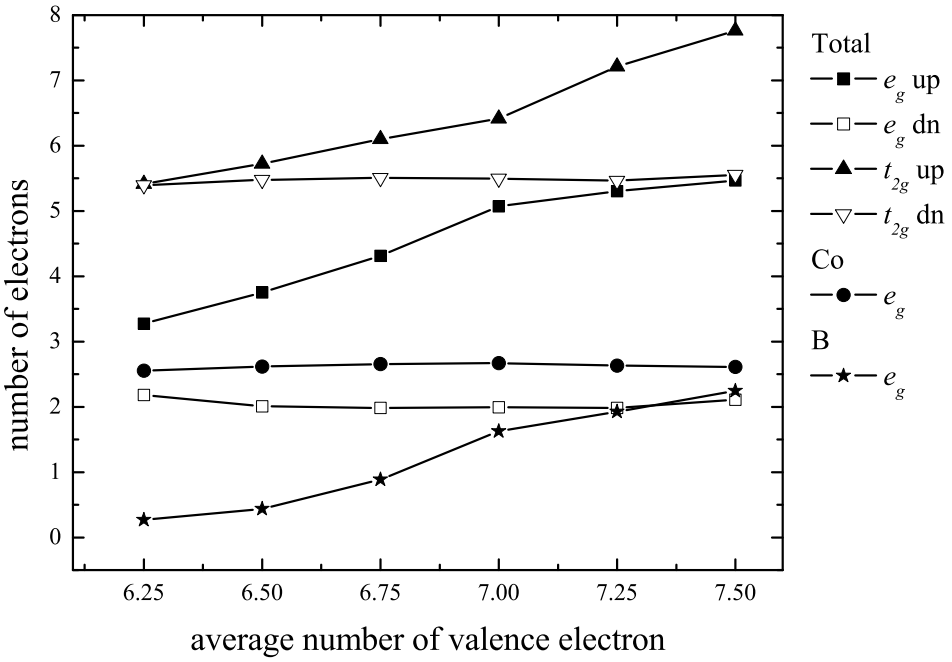

Figure 2.10: Distribution of the d electrons in symmetry distinguished states (e_g and t_{2g}) in Co_2YSi compounds.

a total magnetic moment of 4 μ_B and the second 5 μ_B. Al and Si do not contribute directly to the total magnetic moment. In order to understand the increase of the moment, the electron filling in different symmetry distinguished states are studied in the series of Co_2YAl and Co_2YSi.

As determined earlier by Kübler [101], to maximize the number of unpaired electrons, the minority states should be filled by 8 d electrons and the rest of the electrons fills the majority states.

In the Co_2YAl series, overall (average) 7.85 d electrons are in the minority states. There should be 8 d electrons to fill the d-states completely and to have a gap. The missing part of the electrons is found in the interstitial. That is, they are completely delocalized and cannot be attributed to a particular atom. When inspecting the Co_2YSi series, the number of total minority d electrons is in average 7.5. the remaining are found in the interstitial and overlap with the Si s and p states. To proof this situation in detail, LMTO-ASA [85] calculations were performed to obtain the crystal orbital Hamiltonian population (COHP) of Co-Al and Co-Si. It was found that the bonding interaction between Co and Si is much stronger than between Co and Al. This is expected from the higher electronegativity of Si to Al. Due to the stronger bonding interaction between Co and Si in Co_2YSi, some more electrons are in between the atoms and missing from the total count of 8. At

Table 2.5: Properties of $4d$ or $5d$ containing Co_2-based Heusler compounds. (For quantities see Tables 2.1 and 2.2.)

compound	a_{exp}	m_{exp}	m_{calc}	m_X	m_Y	N_V	ΔE	Ref.
Co_2ZrAl	6.078	0.79	1.00	0.62	-0.10	25	0.296	
Co_2HfAl	6.045	0.82	1.00	0.61	-0.09	25	0.363	
Co_2HfGa	6.032	0.60	1.00	0.60	-0.09	25	0.068	
Co_2NbAl	5.935	1.35	2.00	1.04	0.01	26	0.557	
Co_2NbGa	5.95	1.39	2.00	1.04	-0.01	26	0.527	
Co_2ZrSn	6.254	1.81	2.00	1.09	-0.09	26	0.540	
Co_2HfSn	6.227	1.57	2.00	1.07	-0.07	26	0.480	
Co_2NbSn	6.152	0.69	1.94	0.95	0.07	27	0.430	[5]

the same time, the electrons in the majority states redistribute to have more electrons and as results a higher magnetic moment.

Replacement of Al by Si or higher group members plays an important role for the filling of electrons in the various symmetry distinguished states (t_{2g} and e_g) at Co as well as at Y sites, as collectively shown in Figures 2.9 and 2.10. In-fact the overall number of d electrons remains the same. Addition of an extra electron by replacing Al by Si affects mostly all the symmetry distinguished states except the e_g states at the Y site. The symmetry resolved e_g states of Y are not affected by other states because there is no possible direct overlap to other states whereas, the t_{2g} states form the bonds with the atoms at the X-sites. The e_g states are mainly responsible for the localized magnetic moment at the Y sites.

2.3.3 Other Co_2 based half-metallic ferromagnets

Half-metallic ferromagnetism may not only being found in those Co_2YZ compounds where Y is a $3d$ element but also if Y is a $4d$ (Zr, Nb) or $5d$ (Hf) transition metal. There are various Co_2-based Heusler compounds of this type reported. Among those, it was found that most of them can be expected to exhibit half-metallic ferromagnetism.

The magnetic properties of several, reported Co_2-based Heusler compounds with Y being not a $3d$ transition metal are summarized in Table 2.5. There is obviously a large discrepancy between observed and calculated magnetic moments. For Co_2NbSn, neither the measured nor the calculated magnetic moment come close to the value expected for a half-metallic state. For the Hf containing compounds, spin-orbit interaction may play already an important role, which was not accounted in the calculations. The most interesting point is, however, that only the Co atoms are responsible for the magnetic moment. That means, in none of these compounds a localized magnetic moment at the Y atoms is present. This points on the important fact that the existence of a localized moment at the Y atoms is not a necessary condition for the occurrence of half-metallic ferromagnetism in Co_2-based Heusler compounds.

Table 2.6: Properties of "other" Heusler compounds exhibiting half-metallic ferromagnetism. (For quantities see Tables 2.1 and 2.2.) The crystal structures of Ru_2 based compounds are taken from Ref. [82].

compound	a_{cal}	m_{expt}	m_{calc}	m_X	m_Y	ΔE	N_V
Mn_2VAl	5.897	1.82	1.99	1.52	-0.95	0.318	22
Mn_2MnAl	5.804		0.002	1.423	-2.836	0.546	24
Mn_2MnGa	5.823		-0.012	1.539	-3.030	0.172	24
Mn_2MnSi	5.722		1.000	-0.88	2.69	0.624	25
Fe_2MnSi	5.671	2.33	3.00	0.2	2.63	0.633	27
Ir_2MnAl	6.025		3.99	0.24	3.5	0.351	28
Ru_2MnGe	5.985		3.03	-0.008	3.00	0.125	27
Ru_2MnSi	5.887		3.00	0.02	2.92	0.097	27
Ru_2MnSn	6.217		3.08	-0.06	3.21	0.136	27
Ru_2MnSb	6.200		4.02	0.22	3.55	0.280	28

2.3.4 Other Heusler compounds exhibiting half-metallic ferromagnetism

So far, only the properties of Heusler compounds based on Co_2 were considered. However, there exist also half-metallic ferromagnets in the remaining large group of Heusler compounds (Table 2.6). For example, Galanakis *et al.* [61] have proposed Rh_2-based compounds.

From the remaining group of known Heusler compounds, half-metallic ferromagnetism is only found in Mn containing compounds. Mn_2VAl is the only Heusler compound exhibiting a gap in the majority density of states, unlike the other Heusler compounds. The reason is that Mn_2VAl has only 22 valence electrons, that is less than 24, therefore, the completely filled bands appear in the majority states. Indeed, fixing the number of occupied states in the spin channel exhibiting the gap, which has the result that the other channel has to have less electrons occupied. This is expressed in the Slater-Pauling rule where m becomes virtually negative if $N_V < 24$.

Mn_3Al and Mn_3Ga are two binary compounds reported to order in the same space group as Heusler compounds. Both have zero total magnetic moments and thus are half-metallic completely compensated ferrimagnets (HMCCF) [178]. Fe_2MnSi and Ir_2MnAl are the two non Co_2-based Heusler compounds exhibiting HMF behavior. The other family of Heusler compounds studied are the Ru_2-based. They all have a gap above the ϵ_F. Note in this class, Ru atoms carry small spin moments, in some cases the Ru moment is even negative. However, the Mn moment is large and positive and is responsible for total magnetic moment. There is no compound found from other Ni_2, Cu_2 and Pd_2 based Heusler, which exhibits HMF. Most of them are paramagnetic or ferromagnetic without any gap.

2.4 Summary

In summary, it is proposed that the half-metallic properties in Co_2YZ Heusler compounds are dominated by the presence of Z atoms. According to the results described here, nearly all Co_2YZ compounds will be half-metal ferromagnets.

The magnetic moment carried by X and Y atoms is restricted by the Z atoms even though they do not directly contribute to the magnetic properties. When the main group element Al from Co_2YAl is replaced by Ga, the compound losses its HMF behavior. The influence of N_V on the partial magnetic moments was investigated in detail. It is found that Co_2YZ compounds strictly fulfill the Slater-Pauling rule, whereas other compounds exhibit pronounced deviations from the Slater-Pauling type behavior. The minority band gap decreases with increasing lattice parameter. The inclusion of electronic correlation on top of LSDA and GGA, does not distroy the HMF behavior of Co_2YZ compounds and non HMF compounds become HMF.

It was found that the existence of a localized moment at the Y atoms is not a necessary condition for the occurrence of half-metallic ferromagnetism. Some of these systems with more than 24 valence electrons which exhibit novel magnetic properties, namely half-metallic ferro and ferrimagnetism have been studied in detail. The large exchange splitting of the Y atoms are responsible for the half-metallic property of some of these systems.

Chapter 3

Correlation in the transition-metal based Heusler compounds

3.1 Introduction

Ferromagnetic Co_2-based Heusler compounds have generated increasing interest over the last few years because of their peculiar electronic structure. Half-metallic ferromagnets (HMF) are expected to exhibit a real gap in the minority (or majority) density of states (DOS). In compounds with integer site occupancies, this gap requires the magnetic moment to be an integer because the number of occupied minority states is integer. It should be noted that the HMF character is lost if even a small deviation from an integer value is observed. In Heusler as well as other compounds, the half-metallic ferromagnetism has not yet been unambiguously confirmed by experiments, although there is strong evidence in some cases. Despite a large amount of work on Heusler compounds that contain Co and Mn [19, 46, 59, 63, 68, 78, 83, 137, 138, 145, 179], a breakthrough is still required to prove the existence of half-metallic ferromagnetism in these materials.

In this Chapter, a comprehensive investigation of the equilibrium structural, electronic and magnetic properties of Co_2FeSi is presented and compared to the properties of Co_2MnSi. The dependence of the magnetic moment on the lattice parameter was analyzed, focusing on the differences between the LSDA (local spin density approximation) and the GGA (generalized gradient approximation) treatments. A series of calculations for Heusler compounds based on Co_2 was performed, and showed that almost all Heusler compounds based on Co_2 exhibit half-metallic ferromagnetism [52], results that are in agreement with Ref. [61]. The Slater-Pauling rule [61, 101, 126, 156, 176] applies to most Heusler compounds based on Co_2 and may be used to estimate their magnetic moments. According to this rule, the magnetic moment of Co_2FeSi is expected to be 6 μ_B per unit cell.

To provide a concise picture of the Co_2YSi systems (Y = Mn, Fe), a theoretical investigation will be presented utilizing the local (spin) density approximation (LSDA), the GGA, and the LDA+U methods.

3.2 Results and discussion

The main focus was on the magnetic moment as this shows a very strong discrepancy when the experimental and calculated values reported for Co_2FeSi are compared. Niculescu *et al.* [123] have already reported a magnetic moment of 5.9 μ_B per unit cell at 10K, whereas band structure calculations using the screened Korringa-Kohn-Rostocker method (KKR) later predicted a magnetic moment of only 5.27 μ_B [61]. The present LSDA calculations (FLAPW) also produced a total magnetic moment of only 5.29 μ_B. This value is much lower than the measured value of approximately 6 μ_B measured by Wurmehl *et al.* [176] from our group. Such a large discrepancy clearly indicates that the actual electronic structure of this compound is different from the calculated structure. Although the calculations for Co_2MnSi agree with the experiment in regard to the magnetic moment, their reliability concerning the details of the electronic structure may have to be called into question as long as the differences obtained for Co_2FeSi remain unexplained.

The discrepancy between experiment and calculation was not removed when the GGA parametrization was used, resulting in a value that was still too low (5.56 μ_B). Inspecting the spin-resolved density of states (DOS) and the band structure revealed the appearance of a gap in the minority bands, but located below the Fermi energy (see Figures 3.7(b), 3.8(e) in Sec. 3.2.5). This is one reason why the magnetic moment is too low and not an integer. In the following, details of the electronic structure calculations will be discussed.

3.2.1 Structure optimization

A structural optimization was first performed for Co_2FeSi and Co_2MnSi to determine if the experimental lattice parameter minimizes the total energy. It was found that the optimized lattice parameter from the calculation agrees very well with the experimental values of $a_{exp,Fe}$ = 5.64 Å and $a_{exp,Mn}$ = 5.645 Å. Within the FLAPW scheme, the structure optimization for Co_2YSi (Y = Mn, Fe) was performed using the GGA parametrization and a spin polarized (ferromagnetic) setup. The initial crystal structural parameter for $\Delta a/a = 0$ is taken from the experimental value a_{exp} and varied in steps of 2 %. For each of the different a parameters, the iteration procedure was performed until self-consistency was reached. The energy minimum defines the optimal value of a.

For Co_2FeSi, the energy minimum (ferromagnetic) was found to appear at a = 5.63 Å (corresponding to $\Delta a/a_{exp} \approx -0.2$ %, see Figure 3.1 GGA). It was also found that the ferromagnetic

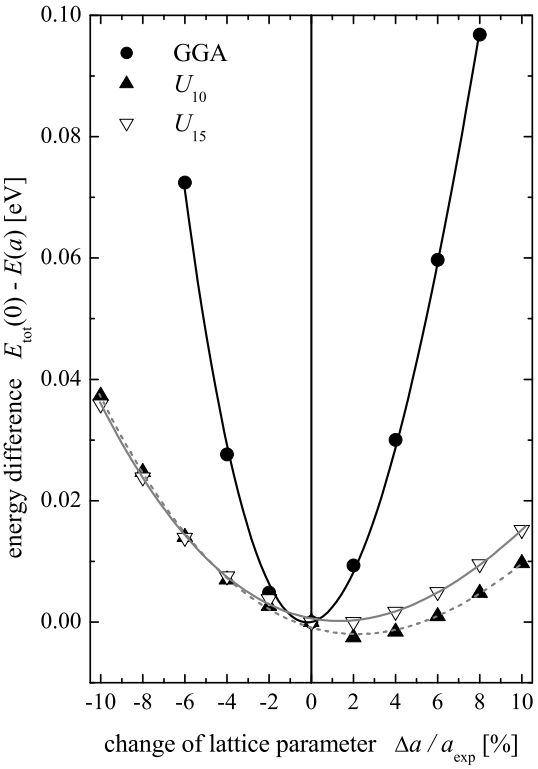

Figure 3.1: Structural optimization of Co_2FeSi. The change of the total energy as a function of the lattice parameter (a_0 = 5.64 Å) is shown. The GGA results are compared to the LDA+U calculations with different U_{eff} (see text). Note that all energy scales are shifted to $E_{tot}(0) = 0$ for better comparison. The lines are results from a polynomial fit.

(spin polarized) configuration has a lower minimum total energy than that found in the paramagnetic (non spin polarized) case, which is not shown here. Similar calculations for Co_2MnSi showed that the energy minimum appears at $a = 5.651$ Å (corresponding to $\Delta a/a_{exp} \approx +0.1$ %).

In addition, Figure 3.1 displays the results of a structural optimization using the LDA+U scheme with U_{eff} as a variational parameter. The results of this optimization, which were performed for different values of U_{eff}, will be discussed below in Sec.3.2.3.

3.2.2 Electronic structure and lattice parameter

To understand why the LSDA and the GGA do not produce the expected magnetic moment and position of the gap, the dependence of both observables on the lattice parameter was carefully examined for Co_2FeSi as well as Co_2MnSi. It is important to compare the electronic structure of

Co_2FeSi with Co_2MnSi as the latter is predicted to be a half-metallic ferromagnet with a measured magnetic moment of 5 μ_B, which is found in calculations that use the experimental lattice parameter. However, a spin polarization of only about 55 % was determined by point contact Andreev reflection spectroscopy [149, 154]. The spin polarization at the ϵ_F determined by means of photoemission was even lower (8 . . . 11 %) [170].

The calculated total and site specific magnetic moments for Co_2FeSi and Co_2MnSi are shown in Figure 3.2. In Co_2FeSi (Figure 3.2(b), the calculated atomic resolved magnetic moments of both Co and Fe increase with a, and the overall magnetic moment follows the same trend, increasing from 4.96 μ_B to more than 6 μ_B as a increases. The experimental value of 6 μ_B is found when the lattice parameter is increased by approximately 6 . . . 10 %. When the lattice parameter changes by more than +6 %, the site specific moments appear to saturate at about 1.5 μ_B and 3 μ_B for Co and Fe, respectively. (Slightly higher values are compensated by an anti-parallel alignment of the moments at the Si sites and in the interstitial space betwen the muffin tin spheres.)

The total magnetic moment of Co_2MnSi (Figure 3.2(a)) also increases slightly with the lattice parameter, but it stays at 5 μ_B when a changes in the range of ±6 %. There is a significant change in the magnetic moment at Mn sites; it increases as the lattice parameter increases. At the same time, the magnetic moment of Co decreases. Thus the Co moment counterbalances the Mn moment such that the overall magnetic moment remains constant as the lattice parameter changes.

Thus a moderate change of the lattice parameter does not change the overall magnetic moment of Co_2MnSi. The case of Co_2FeSi is completely different: an overall change of about 1 μ_B is observed in the same range of $\Delta a/a$ as for Co_2MnSi. Overall, the magnetic moment of Co_2FeSi is less stable against variations of the lattice parameter (at least if using the same parameters for integration and convergence criteria as for the Co_2MnSi calculations). It exhibits some fluctuations about the integer value at very large values of the lattice parameter.

As was explained in detail by Kübler *et al.* [101, 102], the formation of the gap and the localized magnetic moments in Heusler compounds is due to hybridization. There is a close relationship between the magnetic moment and the HMF character. The appearance of the gap in the minority density constrains the number of minority electrons to be integer[1]. However, an integer value of the magnetic moment may not automatically result in a real gap in the minority (or majority) DOS. The band structure of Co_2FeSi (see also below in Sec.3.2.5) already displayed a small gap in the minority states in the calculation for the experimental lattice parameter, but this gap is located below ϵ_F. Therefore, the band structure was examined more closely to check if the integer moment is related to the appearance of a real HMF minority gap.

Figure 3.3 shows the dependence of the external energies of the lower (valence) band and

[1]This is true for ternary Heusler compounds, but may be different in quaternary compounds with non-integer site occupancies.

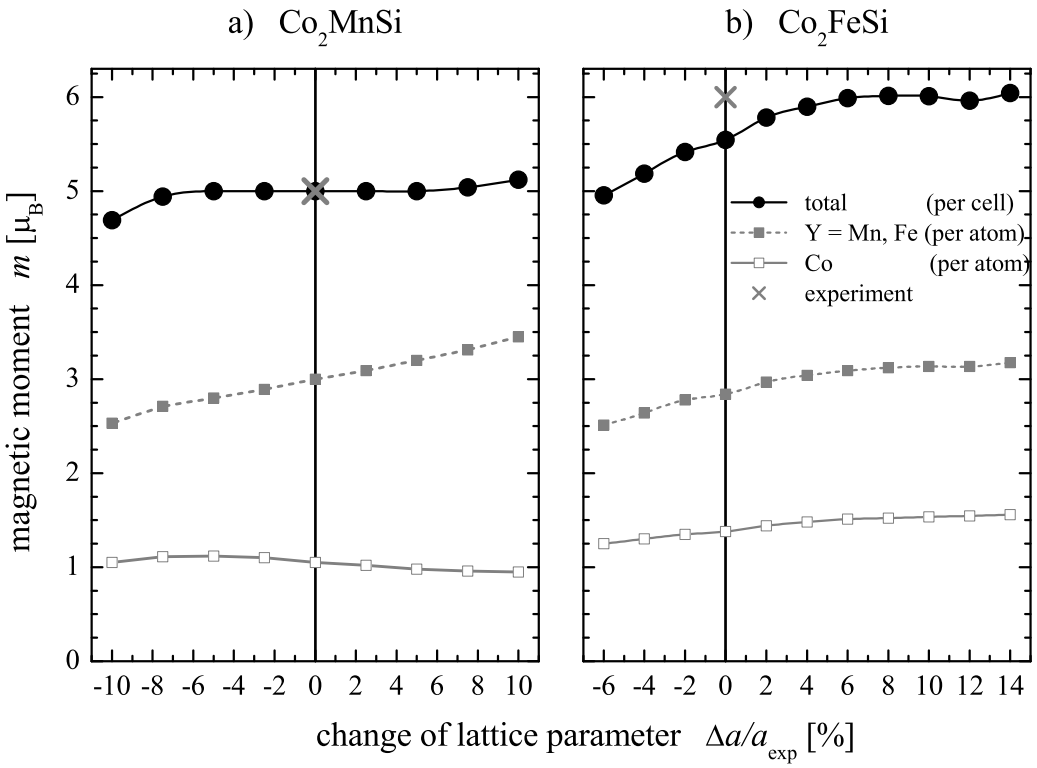

Figure 3.2: Lattice parameter dependence of the magnetic moments. The total and site specific magnetic moments of (a) Co_2MnSi and (b) Co_2FeSi as functions of the lattice parameter are shown. Experimental values are indicated by a cross. The experimental lattice parameters are $a_{Co_2MnSi} = 5.645$ Å and $a_{Co_2FeSi} = 5.64$ Å. Lines are drawn through the calculated values for clarity.

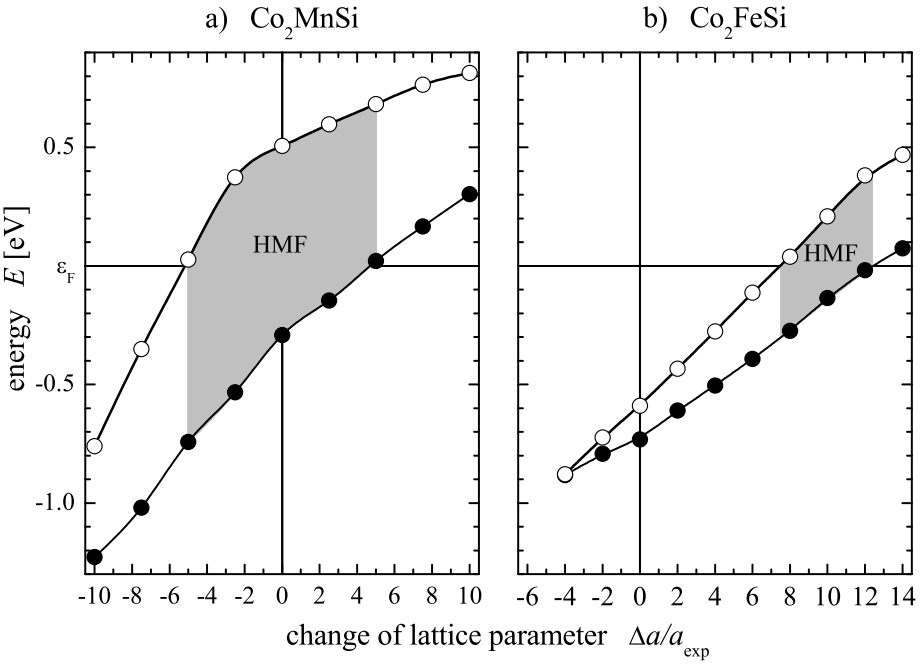

Figure 3.3: Dependence of the minority band gap on the lattice parameter. The external energies of the gap involving states for (a) Co_2MnSi and (b) Co_2FeSi are shown. The shaded areas indicate the region of half-metallic ferromagnetism. Lines are drawn for clarity.

the upper (conduction) band of the minority states enveloping the gap. For both materials, the magnetic moment must be an integer in the region where ϵ_F falls into the gap (gray shaded areas in Figure 3.3), which is the region of half-metallic ferromagnetism.

Figure 3.3(a) shows the dependence of the gap on the lattice parameter for Co_2MnSi. The shaded area corresponds to the region of half-metallic ferromagnetism. It is clearly seen that Co_2MnSi behaves like a HMF within a ± 5 % change of the lattice parameter. Therefore, a moderate change of the lattice parameter does not change the HMF behavior of Co_2MnSi. Figure 3.3(b) shows the dependence of the gap on the lattice parameter for Co_2FeSi. It is seen that the gap encloses the Fermi energy for a 7.5 % to 12 % increase in the lattice parameter. The gap is completely closed for lattice parameters that are 4 % less than a_{exp}. The gap ($\Delta E_{max} = 0.4$ eV at +12 %) is obviously smaller than that for Co_2MnSi ($\Delta E_{max} = 0.9$ eV at -2.5 %), and appears in a narrower range of the lattice parameter. It can be seen that the HMF character and thus the integer magnetic moment is more stable against a variation of the lattice parameter in Co_2MnSi than in Co_2FeSi.

An increase in the lattice parameter by $8 \ldots 12$ %, which is needed to explain the magnetic moment of Co_2FeSi, corresponds to a volume expansion of about $26 \ldots 40$ %. Such a large expansion of the crystal volume by about 1/3 is rather unrealistic and is far greater than the expected uncertainties in the experimental determination of a. However, it may be interesting to check what

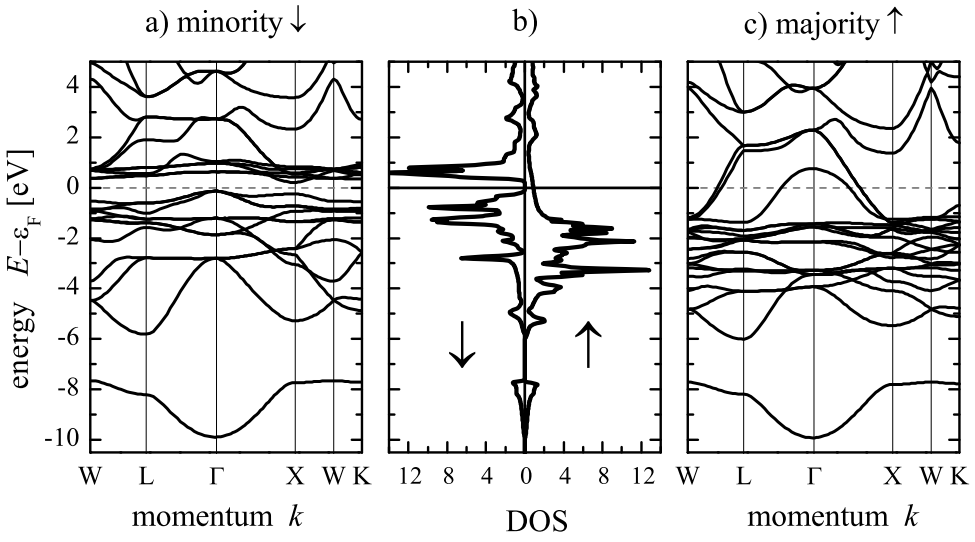

Figure 3.4: Electronic structure of Co_2FeSi with increased lattice parameter. (GGA, $a = 6.2$ Å)

changes in the electronic structure are caused by such an expansion.

The density of states (DOS) and the band structure of Co_2FeSi are shown in Figure 3.4 for the increased lattice parameter. The calculations were performed using the GGA scheme. An expansion of $\Delta a/a = 10$ % was used in the calculation (for $\Delta a/a$ =0 see Sec.3.2.5 and also Ref. [176]). This particular value was chosen because it is the value at which ϵ_f lies just in the middle of the gap of the minority DOS (see Figure 3.4(a),(b), securely placing the material in an HMF state).

There are no minority states at ϵ_F, confirming that the compound is in an HMF state. The high density below ϵ_F is dominated by d states located at Co and Fe sites. The small density of states near ϵ_F in the majority DOS emerges from the strongly dispersing majority bands crossing the ϵ_F. From the spin-resolved bands, it is seen that the majority bands cross or touch the Fermi energy (ϵ_F) in rather all directions of high symmetry. On the other hand, the minority bands exhibit a clear gap around ϵ_F. For Co_2FeSi, the width of the gap is given by the energies of the highest occupied band at the Γ-point and the lowest unoccupied band at the Γ or X-point. The smaller value is found between Γ and X; thus it is an indirect gap. The conclusion drawn from the displayed electronic structure is that the states around the Fermi energy are strongly spin polarized and that, according to the calculations, the system is indeed a half-metallic ferromagnet, at least for an increased lattice parameter. The gap in the minority DOS has the compelling result that the magnetic moment is integer with a value of 6 μ_B, a result that is expected from experiment.

The change of the electronic structure with the lattice parameter is clear for two reasons.

First, a change of the band gradients is expected from a free electron-like band structure, as well as a mere shift of ϵ_F due to the accompanying changes in the DOS. Second, a difference in both overlap and hopping integrals is expected from a tight binding-like approach. In particular, they will be smaller for larger values of the lattice parameter. With a decrease in a, the interaction between the atoms becomes stronger and the higher overlap results in a stronger delocalization of the electrons. The overlap is obviously too large in the calculation that uses the experimental lattice parameter of Co_2FeSi.

The major conclusion that can be drawn from the required increase of the lattice parameter of Co_2FeSi is that LSDA (GGA) calculations are not sufficient to simultaneously explain both its electronic and geometric structure, and thus may also fail for similar compounds. Moreover, it suggests that electron-electron correlation might play an important role in opening the gap in the minority states and for obtaining a magnetic moment with an integer value. For both the lattice parameter and the magnetic moment, the experimental results must be verified independently of the material. In the following section, an analysis will be performed to examine if this goal can possibly be reached by inclusion of correlation.

3.2.3 Electron correlation

The relative importance of itinerant versus localized character of d electrons in metal alloys has already been discussed by van Vleck [165] and Slater [156, 157]. As was first mentioned by Pauling for Cu_2MnAl [126], Heusler compounds are generally thought of as systems that exhibit localized magnetic moments. In particular, the magnetic moments of the Co_2YZ half-metallic ferromagnets strictly follow the *localized* part of the well known Slater-Pauling curve [176]. It is clear that the d electrons are delocalized in metals. Thus, the question about correlation in transition metal based compounds is as follows: to what extent is the on-site Coulomb interaction between d electrons preserved so that important atomic properties like Hund's rule are significant and magnetic properties are at least partially determined [60]?

After structural optimization failed to explain the magnetic moment of Co_2FeSi, it was thought that inclusion of electron-electron correlation may be necessary in order to respect a partial *localization* of the d electrons in a better way. For this reason, the LDA+U method was used to recalculate the electronic structure of Co_2MnSi and Co_2FeSi.

The LDA+U scheme is designed to model localized states when on-site Coulomb interactions become important. It provides a self energy correction to localized states that are embedded in delocalized states. The energy U of the Coulomb interaction is rather large in free atoms (17 eV to 27 eV in $3d$ transition metals, see Appendix B), while screening in solids results in much smaller values [159] (for example, 4.5 eV in bcc Fe). In the present work, the value of the effective Coulomb

Table 3.1: Magnetic moments of Co_2FeSi. Values calculated for $a = 5.64$ Å using different calculation schemes are given (see text). All values are given in μ_B. Total moments (m_{tot}) are given per unit cell and site-resolved values (spin moment m_s, orbital moment m_l) are per atom. U was set to 15 % of the atomic values. +SO indicates calculations that include the spin-orbit interaction.

	Co		Fe		Co_2FeSi
	m_s	m_l	m_s	m_l	m_{tot}
LSDA (vBH)	1.31		2.72		5.29
LSDA (VWN)	1.40		2.87		5.59
GGA (PBE)	1.39		2.85		5.56
GGA + SO	1.38	0.04	2.83	0.06	5.56
LDA+U	1.53		3.25		6.0
LDA+U + SO	1.56	0.08	3.24	0.07	6.0

exchange interaction $U_{eff} = U - J$ was varied in order to reproduce the measured magnetic moment. A magnetic moment of 6 μ_B resulted for a U_{eff} of 2.5 eV to 5.0 eV for Co and, simultaneously, for a U_{eff} of 2.4 eV to 4.8 eV for Fe. As calculated from the corresponding Slater integrals by using Cowan's program [40], these values for U_{eff} correspond to about $7 \ldots 20$ % of the free atom values.

A structural optimization was first performed for Co_2FeSi using different values of U_{eff} in the calculations (see also Sec.3.2.1). It can be seen from Figure 3.1 that adding U_{eff} results in a less pronounced change of the $E(a)$ dependence and shifts the energy minimum slightly to larger values of a. The minima are found at 5.72 Å and 5.75 Å for U_{10} and U_{15}, respectively. These values correspond to a $\Delta a/a_{exp}$ of approximately +1.6 %, and are thus slightly higher than the experimental value. The effect of U_{eff} is that the total energies at the experimental lattice parameter are approximately 3 eV lower for U_{15} than for U_{10}. At the same lattice parameter, the total energy from the LSDA calculation is about 6 eV higher than it is for U_{10}. It should be noted that the total energy given by the LDA+U calculation no longer corresponds to the LDA ground state energy and thus may lead to erroneous conclusions about the structure. However, $E(a, U_{eff})$ will still give an indication of the optimal structure.

3.2.4 Magnetic moment and minority gap in the LDA+U

In the following, the dependence of the magnetic moments on the type of exchange-correlation functional is examined and compared with experimental values. The results of the calculations for Co_2FeSi, using different approximations for the potential as well as the parametrization of the exchange-correlation, are summarized in Table 3.1.

Table 3.1 gives the site-resolved moments at Co and Fe sites and the total magnetic moment. The induced moment at the Si sites (not given in Table 3.1) was in all cases aligned anti-parallel to that at the transition metal sites. Likewise, the magnetic moment located in the interstitial is omitted in Table 3.1; however, both quantities must be included to find the correct total moment.

The lowest value for the total magnetic moment was found using the von Barth-Hedin (vBH) [12] parametrization, and it differed from experiment by -0.7 μ_B. The results from the Vosko-Wilk-Nussair [168] parametrization and the GGA [129] are very similar but still too low compared to the experimental value. It is seen that both site-specific moments are too low to reach the experimental value, which may need values of approximately 1.5 μ_B and 3 μ_B per atom at Co and Fe sites, respectively. This indicates that the LSDA or the GGA approaches are not sufficient for explaining the magnetic structure of Co_2FeSi, independent of the type of parametrization that is used.

The correct magnetic moment at the experimental value of the lattice parameter was only found if the $+U$ functional was used. The LDA+U scheme improves the total magnetic moment considerably (U_{15} was used for the calculations in Table 3.1). The ratio of the magnetic moments of Co and Fe was measured to be $m_{Fe}/m_{Co} = 2.2$ at 300K in an induction field of 0.4T [176]. The ratio of 2.1 found from the LDA+U calculations agrees very well with this value. The spin-orbit interaction (SO) was also included in some of the calculations to examine its influence on the total and partial magnetic moments. Including the SO in the GGA calculations does not improve the total moment. The experiments delivered orbital to spin magnetic moment ratios (m_l/m_s) of approximately 0.05 for Fe and 0.1 for Co. The LDA+U+SO calculations produced values of 0.02 for Fe and 0.05 for Co, values that were factors of 2 smaller than the experimental values. Overall, the agreement of both ratios (m_{Fe}/m_{Co} and m_l/m_s) with experiment is better for the LDA+U than the pure LSDA or the GGA parametrization of the exchange-correlation functional. This may indicate that U corrects, at least partially, the missing orbital dependence of the potential in the LSDA.

Figure 3.5 compares the dependence of the magnetic moment on U_{eff} for Co_2FeSi and Co_2MnSi. For Co_2FeSi, it is found that the total magnetic moment increases from 5.6 μ_B to 6 μ_B as U_{eff} increases from 0 to $U_{7.5}$, and stays at the integer value up to U_{20}. Above that value, the moment exhibits a further increase. The situation is different for Co_2MnSi, which has a total magnetic moment of 5 μ_B at a $U_{eff} = 0$. The moment remains an integer up to approximately $U_{7.5}$, and then increases with increasing U_{eff}.

In Co_2MnSi, the moment at the Mn sites increases almost linearly with U_{eff}. At the same time, the moment decreases at the Co sites up to U_{10}, counterbalancing the Mn moments. At higher U_{eff}, the Co moment increases and the HMF character is lost. The situation is different in Co_2FeSi where both site specific moments show an overall slight increase with increasing U_{eff}. Moreover, they stay rather constant in the range of $U_{7.5}$ to U_{20} so that the total moment remains an integer in this region. Being above the region of integer total moments in both materials, the moment at the Co sites reacts more strongly to U_{eff} than the moments at Y sites react to U_{eff}. The increase in the site specific moments is much less pronounced in Co_2FeSi than in Co_2MnSi. This indicates that the Fe compound is much more stable against correlation effects than the Mn compound, at least

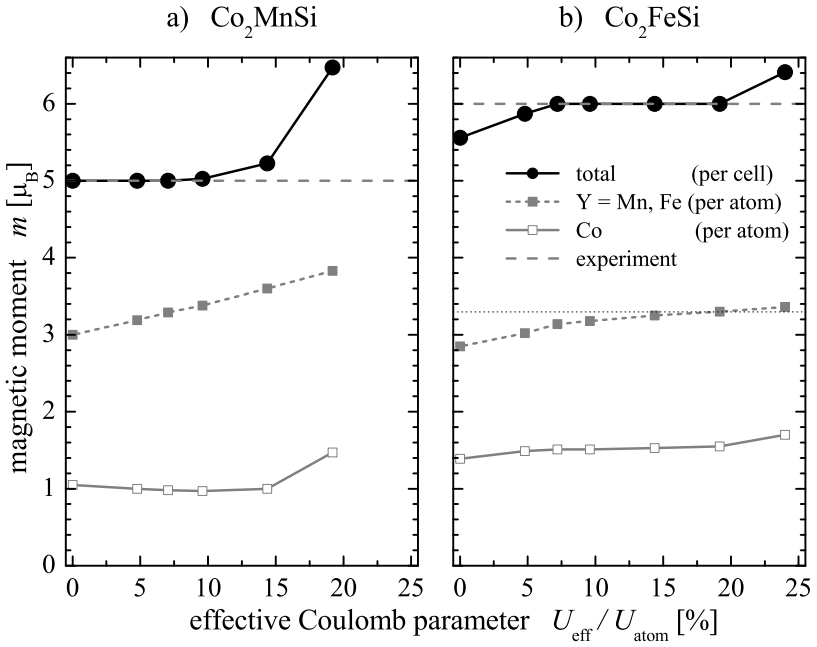

Figure 3.5: Dependence of the magnetic moments on U_{eff}. The dashed horizontal lines indicate the experimental values of the magnetic moments for (a) Co_2MnSi and (b) Co_2FeSi. The calculated values are connected by solid lines for clarity.

as far as the magnetic moments are concerned.

It is again interesting to examine if the integer magnetic moment of Co_2FeSi is related to a real HMF gap in the minority band structure, and to compare the behavior of the Co_2FeSi gap to the Co_2MnSi gap. The external energies of the gap enveloping bands are shown for both compounds in Figure 3.6.

In both cases, the size of the gap increases with increasing U_{eff}. From Figure 3.6(a), it is found that Co_2MnSi stays in an HMF state up to approximately U_8, which is the range of the integer magnetic moment. Larger values shift ϵ_F outside the gap. In Co_2FeSi (Figure 3.6(b), the minority gap includes ϵ_F from approximately U_8 to U_{20}. This means that the integer value of the magnetic moment is related to the minority gap in both compounds and is therefore a direct consequence of the HMF state.

In both compounds, the gap is completely destroyed at very large values of U_{eff} (≥ 8 eV). The effect of the Coulomb exchange interaction on single atoms (Co, Mn, or Fe) on the minority band gap was also investigated. As expected, it was found that the minority gap is destroyed in both materials if U_{eff} is added to only one of the $3d$ elements. However, small changes in only one of the U_{eff} values about the balanced value did not change the general behavior.

3.2.5 Electronic structure in the LDA+U

In the following, the influence of the correlation on the electronic structure will be discussed in more detail. Figure 3.7 compares the spin-resolved density of states for Co_2MnSi and Co_2FeSi that are calculated using the LSDA and the LDA+U approximations. The low lying sp bands emerging from Γ_{5g} (majority) and Γ_{6g} (minority) s states are located at $(-8 \ldots -10)$ eV. They are not shown here (compare with Figure 3.4). These states are coupled to p states ($\Gamma_{5u,6u}$) and are mainly located at the Si atoms.

In both materials, the majority d states range from 8 eV below to approximately 4 eV above ϵ_F, where the onset of the high lying, unoccupied s states becomes visible. s states are also present at below -4 eV due to the $s-d$ coupling of the Γ_{5g} states. p states contribute to the density over the entire range of the d bands. When going away from the Γ-point, they are mixed to s and d states because of the coupling of states with even and odd parity. The high density of states at -1 eV in Co_2MnSi or -2 eV in Co_2FeSi emerges mainly from Γ_{8g} -like states.

The situation is similar in the minority density of states where, in addition, a gap exists. This gap splits the minority d states and the unoccupied part above ϵ_F is mainly of Γ_{7g} character. As already has been discussed above, the minority gap is clearly different in both compounds and depends strongly on the applied effective Coulomb exchange interaction.

In the case of Co_2FeSi, where the experiment clearly indicates the total magnetic moment

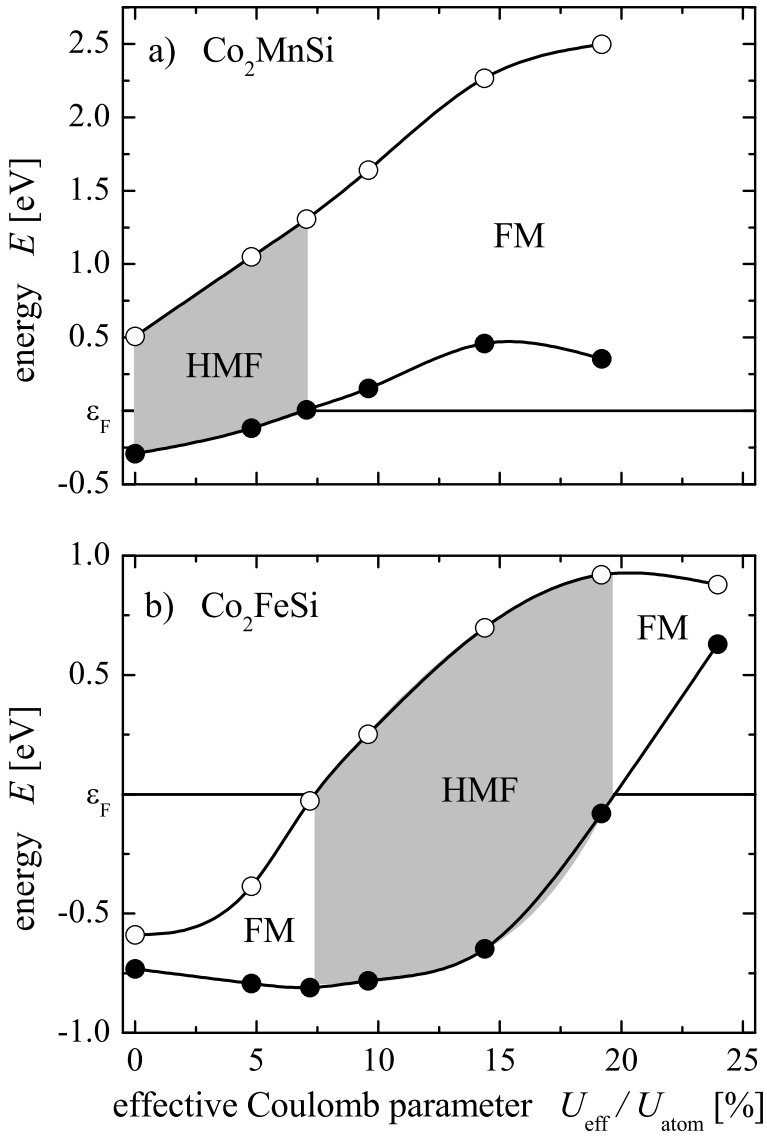

Figure 3.6: Dependence of the minority gap on the effective Coulomb exchange parameter. The external energies of the gap involving states for (a) Co_2MnSi and (b) Co_2FeSi are shown. The shaded areas indicate the region of half-metallic ferromagnetism. Lines are drawn for clarity.

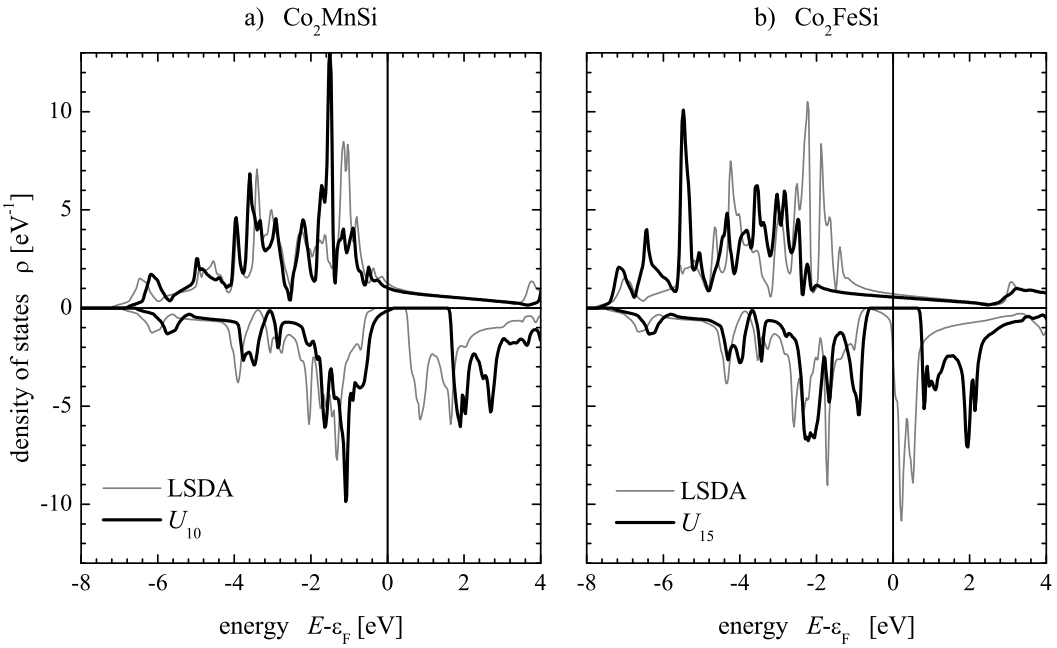

Figure 3.7: Spin-resolved density of states for Co_2MnSi and Co_2FeSi. Grey lines indicate the DOS using the LDA+U with U_{10} for (a) Co_2MnSi and U_{15} for (b) Co_2FeSi. Black lines indicate the results from the LSDA. The upper and lower parts of the plots display the majority and minority states, respectively. (See text for the particular values of U at the different sites.)

to be an integer, the LSDA result seems to be incorrect. On the other hand, it should be noted that the unoccupied d states are sharply peaked at ϵ_F, resulting in a DOS that would imply an inherently unstable system in usual, simple ferromagnetic materials. This is despite the spin polarization. The system is, however, stabilized by the gap in the minority states that fixes the number of occupied states not only in the minority but also – and more importantly – in the majority channel. In the LDA, the paramagnetic e_g and t_{2g} states (located at the Co and Fe sites, respectively) are rather narrow at ϵ_F suggesting that a Coulomb correlation of the Hubbard U type, which is ignored in the LSDA, will make Co_2FeSi insulating in the minority states. By attempting to treat electron correlation using the LDA+U method, the electrons become more strongly localized. One of the major issues here is that the LDA+U type correlation is important for the electronic and magnetic structure of Co_2FeSi. In more detail, the majority states at approximately -4 eV (arising from t_{2g} states in the paramagnetic case) are shifted by U_{15} to -6 eV below ϵ_F. At the same time, the unoccupied minority states, seen in the LSDA calculation just above ϵ_F, exhibit a larger shift of the paramagnetic e_g states (to 2 eV above ϵ_F) compared to the paramagnetic t_{2g} states (to 0.5 eV above ϵ_F). The occupied states of the minority DOS exhibit a less complicated behavior; they are mainly shifted towards ϵ_F.

As shown in Figure 3.7(b) for Co_2FeSi, U_{15} was chosen because the ϵ_F lies just in the middle of the gap for this value. It is clearly seen that the splitting between the occupied Γ_{8g} and

the unoccupied Γ_{7g} states becomes larger. The minority Γ_{7g} states exhibit an additional splitting after applying $+U$, whereas the unoccupied majority states stay rather unaffected. At the same time, the gap in the minority states becomes considerably larger and the ϵ_F is clearly within this gap, confirming that the compound is in an HMF state.

In Figure 3.7(a), the DOS of Co_2MnSi is compared in the LSDA and the LDA+U approximations using U_{10}, which is above the limit for the HMF state. Being mainly located at the Co and Mn sites, the majority d states are clearly seen below ϵ_F and possess a width of approximately 7 eV. A low density of majority states emerging from strongly dispersing d bands is mainly found near ϵ_F. In the LSDA, there are hardly any minority states at ϵ_F, confirming that the compound is a half-metallic ferromagnet. Using LDA+U, the d densities are found to be shifting away from ϵ_F, which is similar to what happens in Co_2FeSi. However, the occupied part of the minority DOS also changes if U_{eff} is applied: it shifts closer to the ϵ_F and crosses it for high values of U_{eff}. Once it reaches ϵ_F, the maximum value of U_{eff} that still results in the HMF state is attained, which is approximately $U_{7.5}$ in this case.

Figure 3.8 shows the changes in the band structure of Co_2FeSi when the LDA+U method is applied. For easier comparison, details of the band structures are shown along $\Gamma - X$, which is the Δ-direction of the paramagnetic state. The Δ-direction is perpendicular to the Co_2 (100) planes. As was shown earlier [53] and as was also pointed out by Öğüt and Rabe [124], only the Δ-direction plays the important role in understanding the HMF character and magnetic properties of Heusler compounds

The development of the band structure with increasing U_{eff} is shown in Figure 3.8 for values of 1.26 eV, 2.52 eV and 3.78 eV at the Co sites and, simultaneously, for values of 1.2 eV, 2.38 eV and 3.56 eV at the Fe sites (U_5, U_{10} and U_{15}). The upper panels (a-d) display majority band structures and the lower panels (e-h) display the minority band structures. It is seen that only slight changes appear in the majority band structure, that the width of the visible bands at Γ stays rather unaffected, and that the main changes appear close to X.

More interesting is the behavior of the minority bands as these determine the HMF character of the compound. It is found that the energies of the occupied states at Γ stay nearly the same. The shapes of the bands close to Γ are similar as well. The situation is different at X, where the unoccupied states are shifted away from ϵ_F, resulting in a gap that increases with U_{eff}. It is clearly seen that this is an indirect gap. At U_{10}, the Fermi energy falls within the gap and the HMF state is reached. The minority gap is larger at Γ or at other points of high symmetry (not shown here) than at X. Therefore, it is obvious that the states at X determine the HMF character of the compound.

At this stage, it is clear that the gap in the minority states stays only within a certain range of the effective Coulomb exchange interaction. Outside of that limit, the Fermi energy no

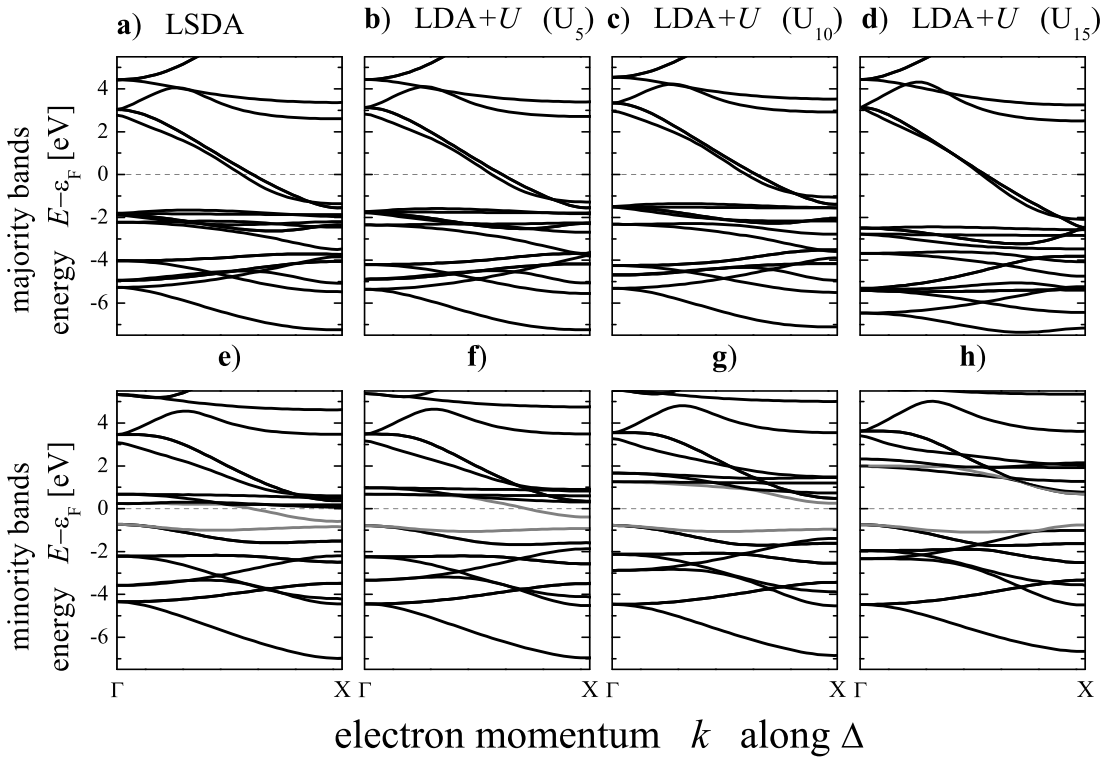

Figure 3.8: Band structure of Co_2FeSi with variation of the Coulomb exchange interaction. The gray lines indicate the upper and lower bands defining the gap at the X-point in the minority states. (See text for the particular values of $U_{\%}$ at the different sites.)

longer falls inside the gap, and the material loses its HMF character. It is also obvious that the same mechanism that leads to the half-metallic ferromagnetism in Co_2FeSi serves to destroy it in Co_2MnSi. The worst case for both materials would appear to be at approximately $7 \ldots 8$ % of the atomic values of U_{eff}, which is where the LDA+U still predicts values very close to the measured magnetic moments but which is also the borderline for the loss of the HMF character. This indicates that nearly integer magnetic moments alone do not verify the half-metallic ferromagnetism and that it may be necessary to search for alternative materials.

Previous band structure calculations using the LSDA predicted Co_2MnSi to be an HMF at the experimental lattice parameter [61, 136]. LDA+U calculations were performed to examine the influence of on-site electron correlation in this compound. It was found that the gap in the minority DOS stays up to a $U_{eff} = 2.3$ eV for Mn, and a $U_{eff} = 2.5$ eV for Co. For larger values of U_{eff}, meaning for stronger correlation, the system loses its HMF character because ϵ_F is shifted outside the minority gap. Co_2MnSi is expected to exhibit 100 % spin polarization at the Fermi energy. This was not verified until now. Wang *et al.* [170] found only about 10 % spin polarization at room temperature from a spin-resolved photoemission experiment. The spectra shown in Ref. [170] give no indication of the existence of a surface state that may serve to lower the spin polarization at ϵ_F. In the present work, it was found that even a moderate correlation will destroy the gap. If U_{10} is applied, then the spin polarization at ϵ_F is 75 %, a value that is compatible to the approximately 55 % found in Ref. [154]. This indicates that on-site correlation might be one more reason why no complete spin polarization was found in this compound (for others, see [47]).

Many effects have been considered in attempting to explain the missing experimental proof for complete spin polarization in predicted half-metallic ferromagnets [47]. Each of these effects may of course serve to reduce the spin polarization at the Fermi energy. On the other hand, none of these effects is able to explain a difference of 15 % between the observed and calculated magnetic moments, as is the case for Co_2FeSi. The appearance of surface or interface states [84, 42] may decrease the spin polarization in certain layers but will not drastically influence the measurements of the magnetization of bulk samples. Magnon excitations [20, 37, 75, 74, 86] will lead to a decrease of the magnetic moment with temperature rather than an increase, and thus can be disregarded here. The spin-orbit interaction does indeed couple spin-up and spin-down states [115], but, as was shown above, does not enhance the magnetic moment. This may indicate that correlation might be one of the main causes for the too low spin polarization that is observed in experiments. In the presented work, a static correction was used in the LDA+U approximation. Dynamic correlation effects may be included in the LDA+$DMFT$ approximation by using dynamical mean field theory (DMFT). Using this method for NiMnSb, it was shown by Chioncel *et al.* [33] that non quasi-particle effects may also serve to change the properties of the gap in the minority states. The use of bulk sensitive angle-, energy-, and spin- resolved photoemission becomes highly desirable for

Table 3.2: Properties of the minority gap of ordered $Co_2Mn_{1-x}Fe_xSi$. Given are the external energies of the valence band maximum (VB_{max}), the conduction band minimum (CB_{min}), and the resulting gap (ΔE) in the minority states as found from LDA+U calculations. The external energies are given with respect to ϵ_F. All energies are given in eV.

x	VB_{max}	CB_{min}	ΔE
0	0.003	1.307	1.3
1/4	-0.181	0.970	1.15
1/2	-0.386	0.495	0.88
3/4	-0.582	0.181	0.86
1	-0.810	-0.028	0.78

explaining the details of the band structure in the most complete experimental manner, as well as for proving the existence of correlation in predicted half-metallic ferromagnets and the actual existence of half-metallic ferromagnetism.

3.2.6 Electronic structure of $Co_2Mn_{1-x}Fe_xSi$ with U

The electronic structure of the substitutional series $Co_2Mn_{(1-x)}Fe_xSi$ with x=0, 0.25, 0.5, 0.75 and 1 was calculated using the LDA+U method. Semi-empirical values corresponding to 7.5 % of the atomic values (see: Ref. [96]) is used and discussed here for the case of the FLAPW calculations.

While inspecting electronic structure of Co_2MnSi and Co_2FeSi, It is found that the ϵ_F shifts from the top of the minority valence band (Co_2MnSi) to the bottom of the minority conduction band (Co_2FeSi). These particular positions of the minority gap with respect to the Fermi energy make both systems rather unstable with respect to their electronic and magnetic properties. Any small change in a physically relevant quantity may serve to destroy the HMF character by shifting the Fermi energy completely outside of the minority gap. As long as the shift is assumed to be small, the magnetic moment may still be similar to the one expected from a Slater-Pauling behavior, even so, the minority gap is destroyed. For this reason, the magnetic moment may not provide evidence for a half-metallic state. Therefore it is to be expected that the situation improves in the mixed compounds containing both Mn and Fe. Figure 3.9 shows the spin resolved total density of states for the compounds with an intermediate Fe concentration ($x \neq 0, 1$). In all cases, the gap in the minority bands is remain there.

The shift of the majority d-states with low dispersion away from the Fermi energy is clearly visible in Figure 3.9. The additional charge (with increasing Fe concentration x) is filling the strongly dispersing d-states in the majority channel. At the same time, the minority DOS is shifted with respect to the Fermi energy such that ϵ_F moves from the top of the minority valence bands at low x to the bottom of the minority conduction bands at high x. In general, it can be concluded that the additional electrons affect both majority and minority states.

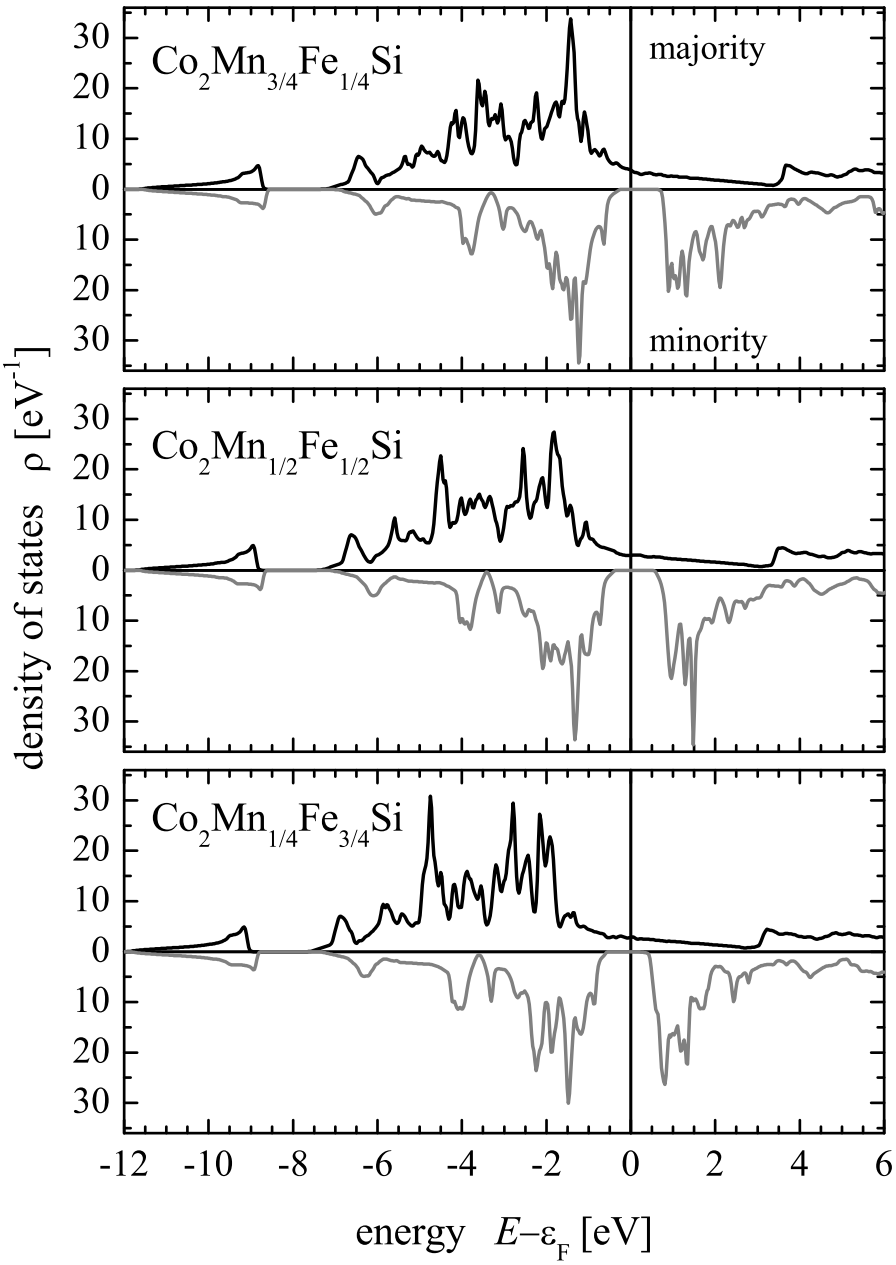

Figure 3.9: Spin resolved density of states of $Co_2Mn_{1-x}Fe_xSi$ for $x = 1/4, 1/2$, and $3/4$.

Table 3.3: Total magnetic moments of ordered $Co_2Mn_{1-x}Fe_xSi$. All moments were calculated for the given super-cells. Their values are in μ_B.

compound	x	GGA	LDA+U
Co_2MnSi	0	5.00	5.00
$Co_8Mn_3FeSi_4$	1/4	5.21	5.25
$Co_4MnFeSi_2$	1/2	5.44	5.50
$Co_8MnFe_3Si_4$	3/4	5.55	5.75
Co_2FeSi	1	5.56	6.00

Table 3.2 summarizes the results for the gap in the minority states as found from LDA+U calculations. The largest gap in the minority states is found for Co_2MnSi. The size of the gap decreases with increasing Fe content x, and at the same time, the position of the Fermi energy is moved from the top of the valence band to the bottom of the conduction band. It is also seen that the compounds with $x = 0$ and 1 are on the borderline to half-metallic ferromagnetism, as the Fermi energy just touches the top of the valence band or the bottom of the conduction band. In both cases, a slight change of U_{eff} in the calculation is able to shift ϵ_F outside of the gap in the minority states.

For intermediate Fe concentration, the Fermi energy falls close to the middle of the gap in the minority states (see also Figure 3.9). This situation makes the magnetic and electronic properties of the compound very stable against external influences that will not be able to change the number of minority electrons. This applies both to the parameters in the theoretical calculations as well as the actual experimental situation. From this observation it can be concluded that $Co_2Mn_{1/2}Fe_{1/2}Si$ exhibits a very stable half-metallic character in this series of compounds, as well as those with a concentration close to $x = 0.5$.

The results found from the LDA+U calculations for the magnetic moments are summarized in Table 3.3 and compared to pure GGA calculations without the inclusion of the U type correlation. It is evident from Table 3.3 that the GGA derived values do not follow the Slater-Pauling curve (with the exception of Co_2MnSi), whereas the values from the LDA+U follow the curve closely. These results again indicate the loss of the minority gap - and thus the loss of half-metallicity - if the on-site correlation is not included.

3.3 Summary

Structural parameters, magnetic moments and electronic properties of the Heusler compounds Co_2MnSi and Co_2FeSi were presented. Using LSDA or GGA calculations, the optimized lattice parameter that is obtained for Co_2FeSi results in a magnetic moment that is too small. The measured value of the magnetic moment was only found for a lattice parameter that was approx-

imately 10 % greater than the experimental value. In the LSDA or GGA approaches, it was also shown that the magnetic moment of Co_2MnSi is more stable against structural changes. At this time, it appears that simple LSDA and GGA methods are not sufficient for explaining the electronic structure of Heusler compounds in detail. At least for Co_2FeSi, these methods fail.

In a step beyond the basic LSDA and for the case of Co_2FeSi, it was shown that electron correlation is able to explain the experimental magnetic moment at the experimentally observed lattice parameter. It was found that the LDA+U scheme satisfactorily reproduces the experimental observations. At moderate effective Coulomb exchange-correlation energies of approximately 2.5 eV to 4.5 eV, the LDA+U calculations agreed very well with the measured total and site specific magnetic moments. At the same time, the compound was clearly predicted to be a half-metallic ferromagnet.

How the inclusion of correlation would change the calculated properties of similar Heusler compounds was also examined. Co_2MnSi is a compound that is close to Co_2FeSi in the series of known Heusler compounds based on Co_2. It is obvious that on-site correlation will also play an important role in the Mn compound if it plays an important role in the Fe compound. It was found that a small correlation energy of only approximately 2.5 eV destroys the half-metallic ferromagnetism, which may explain why a complete spin polarization was not observed in this compound until now.

The substitutional series of the quaternary Heusler compound $Co_2Mn_{1-x}Fe_xSi$ was investigated theoretically. The results found from the LDA+U calculations for the magnetic moments $m(x)$ closely follow the Slater-Pauling curve. The shift of the minority gap with respect to the Fermi energy, from the top of the minority valence band for Co_2MnSi to the bottom of the minority conduction band for Co_2FeSi, makes both systems rather unstable with respect to their electronic and magnetic properties. The calculated band structures suggest that the most stable compound in a half-metallic state will occur at an intermediate Fe concentration. The results qualitatively confirm experimental studies on magnetic behavior on quaternary Heusler compound $Co_2Mn_{1-x}Fe_xSi$.

In conclusion, it is suggested that the inclusion of electron-electron correlation beyond the LSDA and the GGA will be necessary to obtain a theoretical description of all potential half-metallic ferromagnets, and in particular for Heusler compounds.

Chapter 4

Electronic structure, magnetism, and disorder in the Heusler compound Co_2TiSn

4.1 Introduction

In this Chapter, the properties of the Co_2TiSn Heusler compound are analyzed theoretically as well as experimentally. The impetus for this work was a recent experimental study that was devoted to measuring the magnetic transition in this Heusler compound. Co_2TiSn is predicted to be half-metallic ferromagnet. A number of electronic structural and magnetic studies have been carried out on one specific Heusler compound Co_2TiSn. For example, Majumdar *et al.* [110] have observed a semiconductor-metal transition at the Curie temperature of this compound at 350 K, for which they invoked low carrier concentration at the ϵ_F. Pierre *et al.* [140] have systematic studied the magnetic behavior of Co_2TiSn. A number of theoretical studies on this compound have also been carried out [71, 107, 119]. Despite this rich theoretical and experimental literature, some of the behavior of Co_2TiSn remains ambiguous.

The goal of this contribution is two-fold. A combination of X-ray diffraction and magnetization measurements on a well-annealed polycrystalline sample of Co_2TiSn have been used to establish that it seems, by these techniques, to be well-ordered. The *local* probes of ^{119}Sn Mössbauer spectroscopy and ^{59}Co spin-echo nuclear magnetic resonance spectroscopy are used to accurately establish the degree of antisite disorder in this seemingly well-ordered compound. Finally, it can be established that different levels of density functional theory provide distinctly different results re-

garding whether the compound is half-metallic. Using the highest level of these computations, it is demonstrated that as much as 12.5% antisite Co/Ti disorder does not destroy the half-metallic character.

4.2 Experimental methods

Starting from the elements, the preparation of Co_2TiSn was achieved by arc-melting under an argon atmosphere after many pump/purge steps using a 10^{-4} mBar vacuum. The arc-melting procedure was repeated three times to ensure homogeneity. The product was subsequently sealed in an evacuated silica tube and annealed at 800 K for 14 days. The room temperature X-ray diffraction pattern of Co_2TiSn was measured on a Bruker D8 instrument operated in reflection geometry with a MoK_α X-ray source. SQUID magnetization measurements on the annealed sample were performed on a Quantum Design MPMS 5XL magnetometer. The measured saturation magnetic moment was $2\,\mu_B$ per formula unit at 5 K.

Mössbauer measurements on powder samples were performed in the transmission geometry using a constant-acceleration spectrometer and a He bath cryostat. ^{119}Sn Mössbauer spectra were measured using a 10 mCi ^{119}Sn ($CaSnO_3$) source. The RECOIL 1.03 Mössbauer analysis software was used to fit the experimental spectra [160]. ^{59}Co NMR experiments on samples of powdered Co_2TiSn were carried out at 4.2 K using a broadband phase-sensitive spin-echo spectrometer [121]. The NMR spectra were recorded by measuring spin-echo intensities. In the final NMR spectrum, these were corrected for the enhancement factor and for the usual ω^2 dependence of spectrum intensity, to obtain relative intensities that are proportional to the number of nuclei with a given NMR resonance frequency. The external magnetic field was zero, and a constant excitation RF field was used [17].

4.3 Results and discussion

4.3.1 Experiments

Figure 4.1 displays the Mo-Kα X-ray powder diffraction pattern of the annealed Co_2TiSn sample. Experimental data are displayed as points. The data were subject to refinement using the Rietveld method as implemented in the XND code [15]. The gray line is the Rietveld fit (R_{Bragg} = 3.7%) to the cubic $Fm\overline{3}m$ Heusler structure with a cell parameter that refined to 6.0718(3) Å. Since the atomic number of Sn ($Z = 50$) is well distinguished from the atomic numbers of Ti ($Z = 22$) and Co ($Z = 27$), a number of simulations were performed where the Sn site was partially occupied by these lighter atoms. These simulations suggested that Sn is fully ordered in this compound. The small Z difference between Co and Ti did not allow for their relative occupancies in the two sites

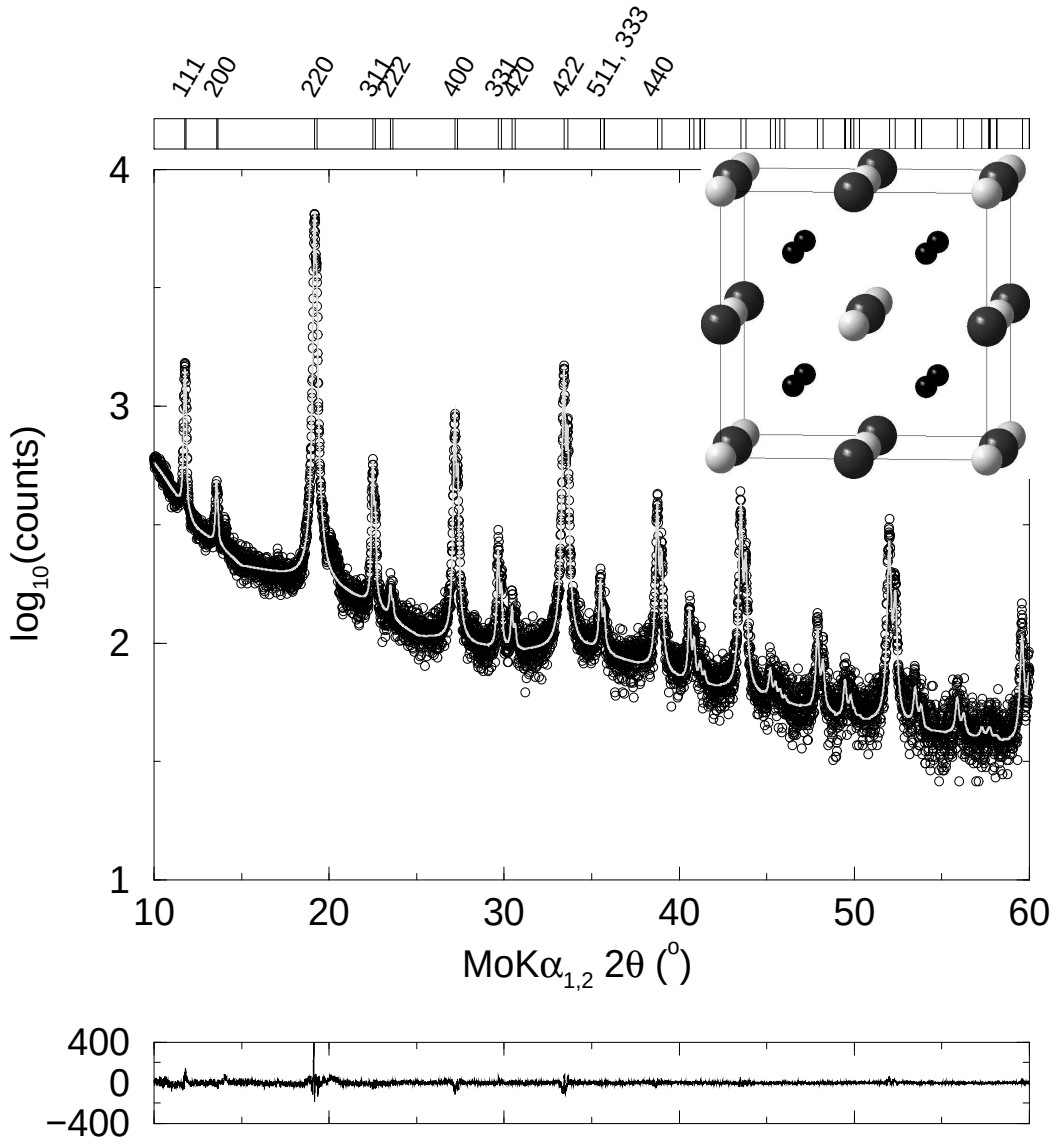

Figure 4.1: MoK_α X-ray powder diffraction pattern of an annealed Co_2TiSn sample, plotted on a semilog scale. Points are data, and the gray line is the Rietveld fit. The difference profile is also displayed in the panel below, in linear counts. The inset is the Heusler crystal structure showing Co atoms (small black spheres) at 8*a* ($\frac{1}{4}\frac{1}{4}\frac{1}{4}$), Ti atoms (small light-gray spheres) at 4*a* (000), and Sn atoms (large dark-gray spheres) at 4*b* ($\frac{1}{2}\frac{1}{2}\frac{1}{2}$). Vertical lines at the top of the plot are the expected α_1 and α_2 peak positions. The low angle peaks are indexed.

to be refined, so that in the refinement model, their occupancies were fixed to one corresponding to 8.8% antisite Co/Ti disorder as suggested by the other *local* probes presented here. The refined isotropic thermal parameters for all atoms were somewhat large but reasonable, in the range of B = 1.4 to 1.7 Å^2.

The ^{119}Sn Mössbauer spectrum of annealed sample of Co_2TiSn measured at room temperature is shown in Figure 4.2(a). To fit the spectrum a magnetic hyperfine field distribution model was employed. The Co_2TiSn spectrum can be decomposed into three sub-spectra with the same isomer shift IS = 1.48(2) mms^{-1} and zero quadrupole splitting. The partial intensities and hyperfine magnetic fields of the three sub-spectra are provided in the caption of Figure 4.2. A resolved hyperfine structure is revealed in the distribution $p(H)$ displayed Figure 4.2(b). The asymmetrical distribution has a maximum at 65.9(1) kOe and small intensity at zero value of the hyperfine field. Note that the hyperfine field density distribution curve for a completely ordered compound should contain only one symmetrical peak. The asymmetry in the $p(H)$ distribution as a function of the hyperfine field suggests partial disordering of the environment around Sn. To complete the interpretation, ^{59}Co NMR spectroscopy was used.

The ^{59}Co NMR spectrum of Co_2TiSn acquired at 5K is presented in Figure 3. The resonance frequencies f are related to the hyperfine fields (indicated on the upper abscissa) through the gyromagnetic ratio, $g = 1.0103$ kHz Oe^{-1}. The spectrum can be decomposed into five Gaussian peaks A through E with the parameters described in the caption. The dominant line in the spectrum at frequency $f_C = 21.1(3)$ MHz is unsplit in agreement with the cubic structure of Co_2TiSn. Two satellite lines located at $f_D = 27(3)$ MHz and $f_E = 35(4)$ MHz correspond to Co atoms experiencing higher hyperfine fields in comparison to the main line. The main line as originating from Co atoms is considered in ordered stoichiometric surroundings, whereas the satellites stem from the Co positions with Co atoms in their first coordination sphere. The first coordination sphere of Co atoms in the fully ordered structure would be 4 Ti and 4 Sn atoms. Statistical mixing of Ti and Co atoms should obey the expression for the probability to find n impurity atoms from amongst N neighbors:

$$W_n = \frac{N!}{n!(N-n)!}(1-x)^n x^{N-n}$$

where x is fraction of "extrinsic" atoms. For example, the probability corresponding to a single extra Co atom substituting a Ti would correspond to $N = 4$ (for the four usual Ti neighbors) and n = 1 (for the Co atom substituent). A binomial distribution describing the probability of observing the "undisturbed" first coordination sphere suggests 7.8% of Co atoms substituting Ti atoms. The resonance line at $f_D = 27(3)$ MHz originates from a Co atom with one Co atom substituting one of the 4 Ti in its first coordination shell, and at $f_E = 35(4)$ MHz, the Co atoms being probed has two Co atoms substituting for Ti.

The second coordination sphere of Co atoms comprises six Co atoms. Substitution of the

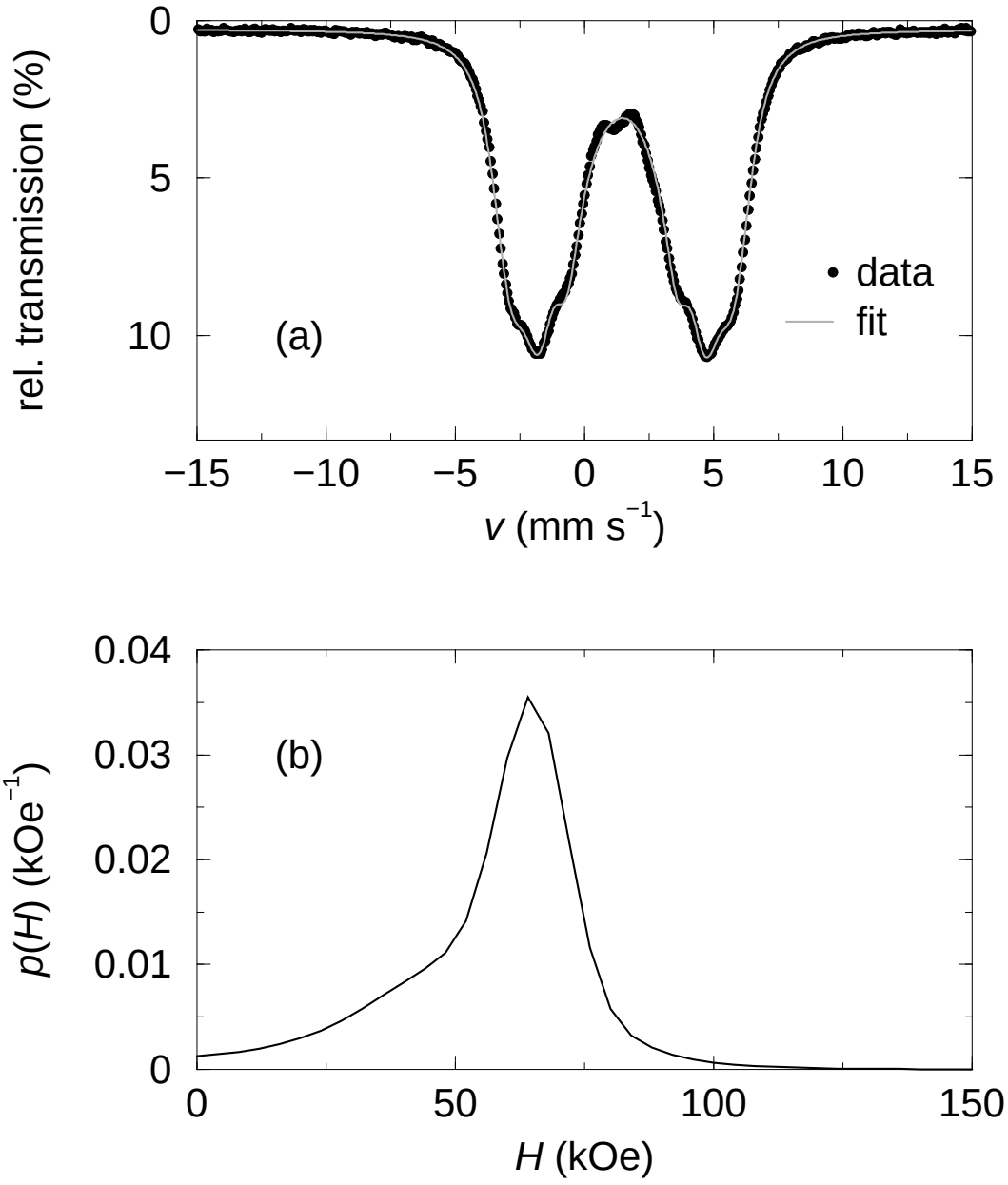

Figure 4.2: (a) ^{119}Sn Mössbauer spectrum of annealed Co_2TiSn sample recorded at 295 K and (b) the hyperfine magnetic field distribution on Sn atoms in Co2TiSn. The spectrum is fit using a single isomer shift but assuming the following distribution of hyperfine fields and their relative intensities: 65.9(1) kOe (49%), 56.4(8) kOe (39%), and 20(1) kOe (12%).

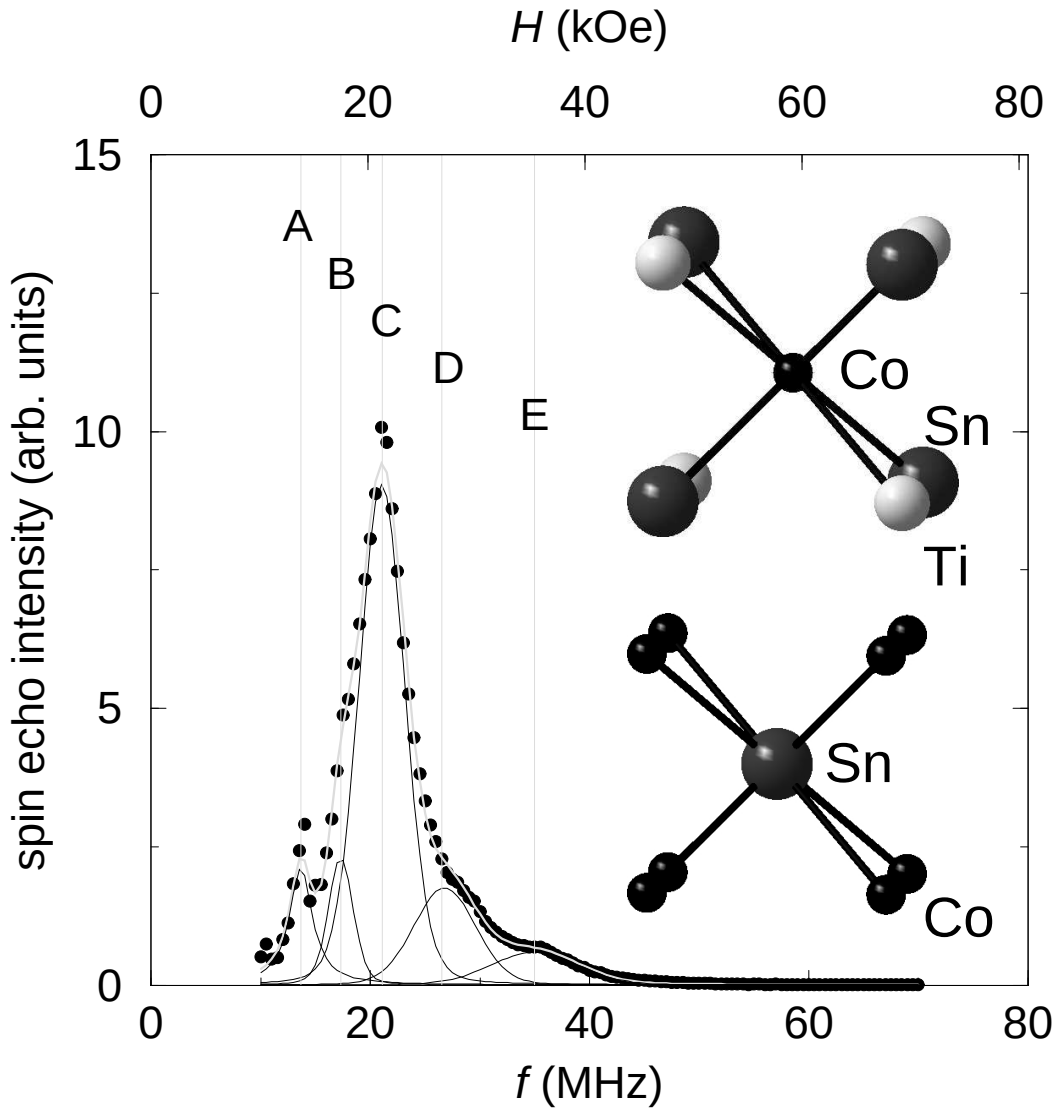

Figure 4.3: ^{59}Co NMR spectrum of Co_2TiSn. The data could be fit using five Gaussian peaks whose centers are indicated by vertical gray lines. The resonance frequencies (relative intensities) of the five peaks (labeled A through E) are: $f_A = 13.7(3)$ MHz (10%), $f_B = 17.3(4)$ MHz (8%), $f_C = 21.1(3)$ MHz (60%), $f_D = 27(3)$ MHz (15%), and $f_E = 35(4)$ MHz (7%). The upper abscissa displays the equivalent hyperfine fields. The insets show the (4Ti + 4Sn) coordination of Co and the 8Co coordination of Sn.

Co atoms in the second coordination sphere by nonmagnetic Ti atoms should decrease the hyperfine magnetic field and hence the resonance frequency. The resonance line at $f_B = 17.3(4)$ MHz is attributed to a Co having one of its six Co in the second coordination sphere being replaced by Ti, and the line at $f_A = 13.7(3)$ MHz is then attributed to a Co with two Ti atoms, substituting for two Co atoms in its second coordination sphere. The binomial distribution model gives the amount of Ti atoms substituting Co atoms to be 8.8%. Taking into account the amount of Co atoms substituting Ti atoms, the final composition describing the antisite disordering, can be approximately written: $[Co_{(2-0.09)}Ti_{(0.09)}][Ti_{(1-0.09)}Co_{(0.09)}]Sn$ or more consisely as $(Co_{1.91}Ti_{0.09})(Ti_{0.91}Co_{0.09})Sn$.

With an understanding of disorder from NMR, one can return to the X-ray diffraction in order to understand why it is unable to discern the disorder. The exchange of Ti with Co atoms on both 8*a* positions, as suggested by NMR, is indicative of the structure being partially DO_3-like. Because both the usual Heusler ($L2_1$) and the DO_3 structure type have the same space group ($Fm\bar{3}m$) symmetry, and because the scattering factors of Ti and Co are not well distinguished in X-ray diffraction, the determined composition $(Co_{1.91}Ti_{0.09})(Ti_{0.91}Co_{0.09})Sn$ is not easily distinguished by X-ray diffraction from pristine Co_2TiSn.

The site assignment of Sn atoms follows from the statistical analysis of intensities obtained from Mössbauer spectroscopic measurements. First coordination sphere of Sn atoms comprises eight Co atoms. Partial substitution of Co atoms by Ti atoms should diminish the hyperfine magnetic field on Sn atoms. This effect clearly follows from the hyperfine field distribution presented in the caption of Figure 4.2. The sub-spectrum with a hyperfine field of 65.9(1) kOe is to be assigned to the "undisturbed" configuration of Sn atoms. The sub-spectrum with the reduced hyperfine field of 56.4(8) kOe corresponds to Sn with seven Co and one Ti neighbors. The part of distribution with a hyperfine field of 20(1) kOe indicates the further increase in the amount of Ti atoms substituting Co atoms in the first coordination sphere of Sn; six Co and 2 Ti. The binomial distribution then suggests 8.6% of Ti atoms substituting Co on average which is in excellent agreement with the 8.8% proposed based on the ^{59}Co NMR experiment. The composition $(Co_{1.91}Ti_{0.09})(Ti_{0.91}Co_{0.09})Sn$ is therefore consistent with the ^{119}Sn Mössbauer data as well.

4.3.2 Computation

Densities of state of ordered Co_2TiSn obtained using the different methods are shown in Figure 4.4. It is seen that the methods using spherical potentials (LMTO-ASA and SPRKKR) fail to obtain the correct, measured half-metallic ground state, and panel (a) of this figure shows that within these computational schemes, minority spin state are occupied. This results in reduced moments as well. The full potential schemes embodied in the WIEN2K and FPLMTO codes however do correctly obtain a minority gap in this compound, and the full, measured magnetic moment of $2\,\mu_B$ *per* formula

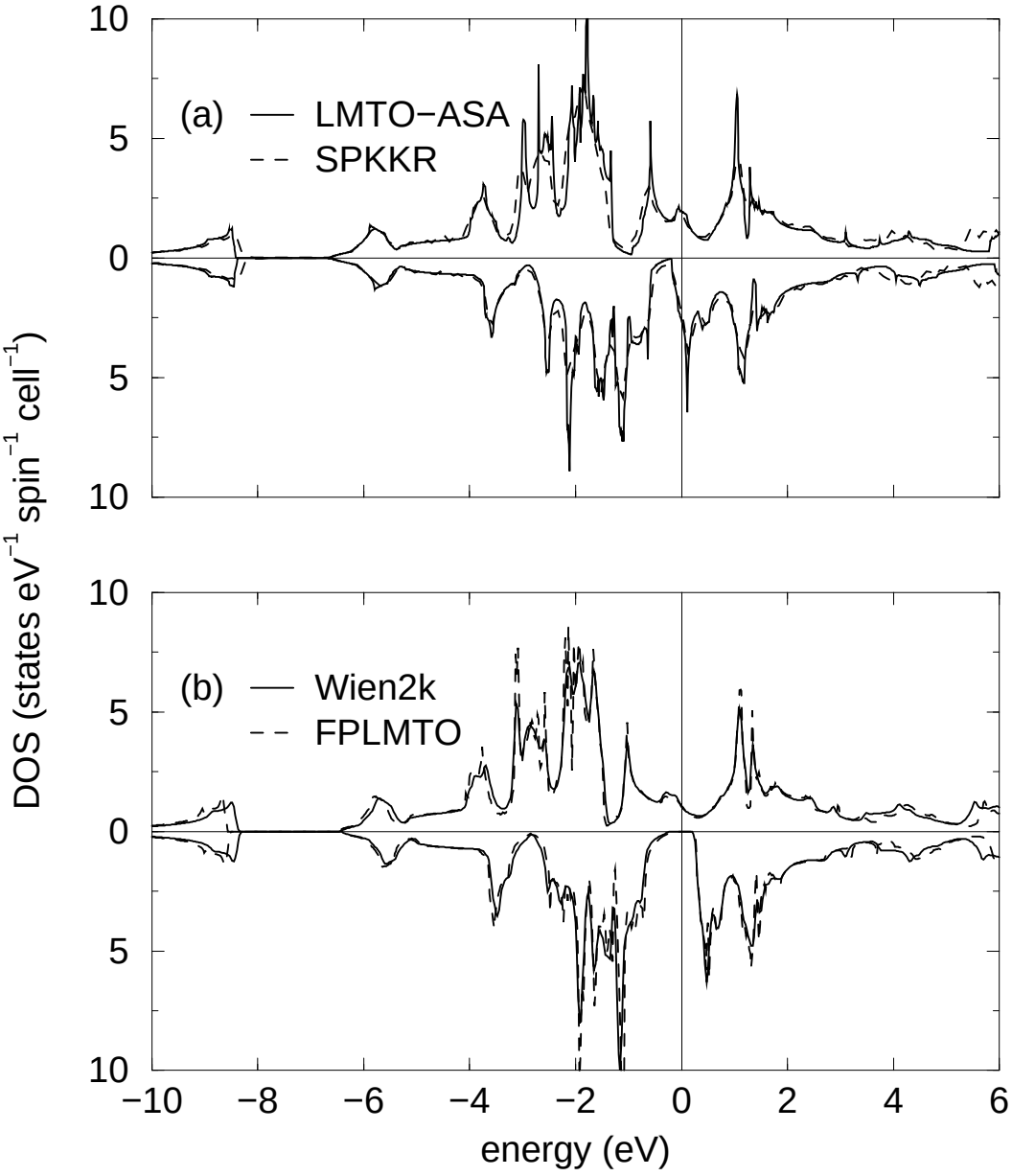

Figure 4.4: (a) Densities of state of ordered Co_2TiSn obtained using the LMTO-ASA and SPRKKR codes. (b) Densities of state of ordered Co_2TiSn obtained using the WIEN2K and FPLMTO codes. 0 on the energy axis is ϵ_F. All the calculations used the generalized gradient approximation.

Table 4.1: Magnetic moments of ordered Co_2TiSn calculated using different schemes.

Code	LDA moment (μ_B)	GGA moment (μ_B)
LMTO-ASA	0.84	1.40
SPRKKR	1.11	1.55
WIEN2K	1.99	2.00
FPLMTO	1.99	2.00

unit. Very little, if any, difference is seen between the two spherical potential codes, and between the two full-potential methods. The calculated moments using different codes, and using LDA and GGA are summarized in Table 4.1. The calculated total magnetic moments are in the range from 0.84 to 2.00 μ_B. It is also noted that in addition to using full-potential methods, gradient corrections (GGA) are necessary as well in order to obtain the correct electronic structural description of this compound.

In accordance with our NMR and Mössbauer experiments, the most probable defects in Co_2TiSn are Co-Ti swap, which give rise to the general formula $(Co_{2-z}Ti_z)(Ti_{1-z}Co_z)Sn$, with z in this case being close to 0.09. Two other kinds of disorder can be considered: A Co-antisite where a Ti atom is replaced by Co, and a Ti-antisite where a Co atom is replaced by Ti. Disordering of Sn atom is not considered since neither the local probes, nor X-ray diffraction give any suggestion of it. All three cases of disordering have been considered in band structure calculations, with disordering rate of 12.5%. This value was chosen because it is easily implemented in supercells involving doubling lattice parameters in all three directions. It is also close to what is experimentally observed. It should be noted that all three modes of disorder require lowering of symmetry from cubic.

Figure 4.5 shows the WIEN2K-GGA densities of state, scaled to one Co_2TiSn formula unit, for the three cases of disordering. In order to focus on the gap in the minority spin direction, the data are displayed in a small window of energy around ϵ_F. It is seen that in all cases, the minority gap at ϵ_F (half-metallic character) is retained. All three modes of disorder results in new states being created in the minority gap of pure Co_2TiSn. The majority states are nearly unaffected by the disorder. Excess Co substituting for Ti is seen to create states above ϵ_F, whereas excess Ti substituting for Co is seen to create states below ϵ_F. The swapping of Co and Ti does a little of both, and the gap as a consequence, is almost lost. All three calculations suggested that the average moment *per* formula unit remains near 2 μ_B suggesting once again, that even computationally, the magnetic moment is a poor indicator of disorder. In general, these Heusler compounds seem to be robust half-metals. While the calculations refer to zero Kelvin, it can be expected that smearing of states at finite temperature will further diminish the gap, and at least for the last case (c) of the Co/To swap, the consequence of disorder in conjunction with finite temperatures can be expected to be deleterious for half-metallic behavior.

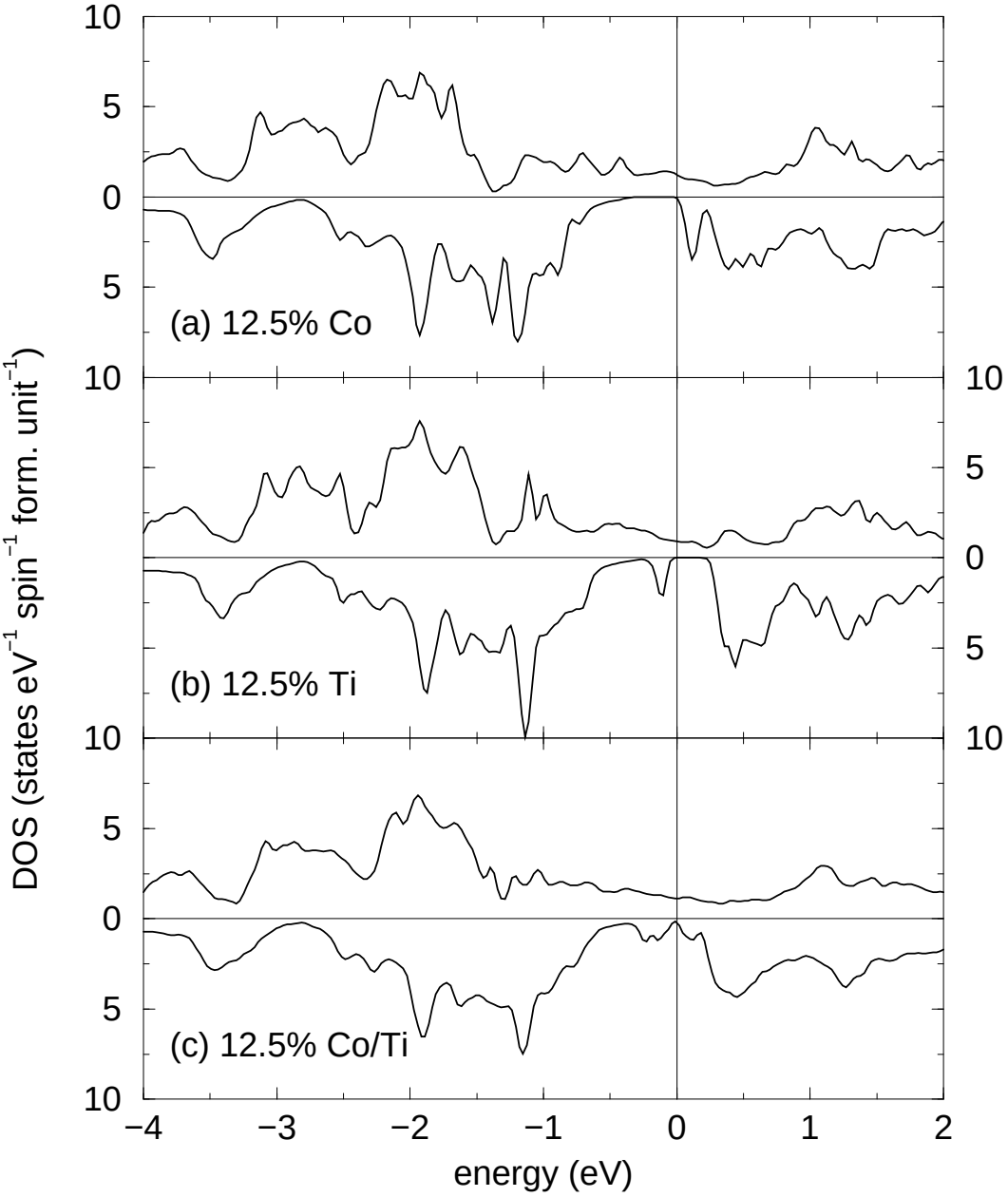

Figure 4.5: Densities of state of disordered Co_2TiSn obtained using the WIEN2K code: (a) 12.5% Co substituting Ti; (b) 12.5% Ti substituting Co; (c) 12.5% Co/Ti swap.

4.4 Summary

This work allows a number of conclusions to be drawn from the combination of experiments and computation on an important Heusler compound. From experiments, it has been observed that compounds that seem to be ordered, from X-ray diffraction, and from magnetization measurements, can through *local* probes such as Mössbauer and NMR be found to possess significant and quantifiable antisite disorder. In this particular case, the precise nature of the disorder is consistent with approximately 9% of Co and Ti exchanging their lattice sites. The power of Mössbauer and NMR used together in establishing local disorder have been demonstrated.

Computationally, the very interesting result is demonstrated that different implementations of density functional theory provide distinctly different results. To correctly reproduce the half-metallic ground state of Co_2TiSn, both non-local descriptions of the exchange correlation functional (GGA) as well as, more importantly, non-spherical potentials are required to be used in the calculations. Thus, it is only the full-potential methods that are able to correctly represent the electronic structure of Co_2TiSn. DFT does not do a very good job of calculating the hyperfine fields on the different atoms, and a very sensitive dependence of these on correlation effects is found. In agreement with experiment, the system can accommodate quite a large degree of antisite disorder without loosing its half-metallic character.

Chapter 5

Covalent bonding and the nature of the band gaps in some cubic $C1_b$ compounds

5.1 Introduction

The cubic $C1_b$ phases XYZ, constitute an important class of materials with particular regard to their magnetic properties. de Groot [41] and coworkers showed a number of years ago that the $C1_b$ structure compound NiMnSb can be described as a half-metallic ferromagnet, whose computed band structure resembles a metal in one spin direction, and a semiconductor in the other. Since then, and indeed, even prior to that, it has been recognized that the electronic structure and hence properties of Heulser compounds [102] and $C1_b$ compounds [141, 162] are very sensitive to the valence electron count.

A number of electronic structural studies have been carried out on the $C1_b$ compounds. From the viewpoint of chemical bonding in these compounds, Whangbo and coworkers [93] have examined the non-magnetic band structures, using the extended Hückel method, of a number of $C1_b$ compounds with varying valence electron counts. These authors have recognized that many XYZ $C1_b$ compounds can be thought of as comprising an X^{n+} ion stuffing a zinc blende $(YZ)^{n-}$ sublattice where the number of valence electrons associated with YZ^{n-} are 18 ($d^{10} + s^2 + p^6$). 18 electron compounds are therefore closed shell species; non-magnetic and semiconducting. They further suggest that the 17 and 19 electron XYZ would undergo a Stoner instability [161] to a ferromagnetic ground state, while the 22 electron compounds (typically with Mn^{3+} at the X site)

should be localized moment ferromagnets. The 22 electrons divide themselves into 13 in the majority spin and 9 in the minority spin direction, resulting in a semiconducting gap (half-metallic behavior) in the minority spin direction. Recently, Galanakis *et al.* [61] have placed this "18 electron" rule on a more formal footing.

Pierre *et al.* [141] were amongst the first to recognize the importance of the valence electron count in the $C1_b$ compounds [1]. In more recent work, Tobola and Pierre [162] have emphasized the importance of covalency in these compounds. The Z element is often a pnictogen (As, Sb or Bi) or some other main group element because only covalent bonding would justify the somewhat open $C1_b$ structure. Öğüt and Rabe [124] have examined the electronic structures of the compounds XNiSn with X = Ti, Zr, or Hf, and interpreted phase stability and the nature of band gaps. Nanda and Dasgupta [122] have examined nearly 20 different $C1_b$ compounds using the FP-LMTO and LMTO-ASA methods, including a detailed analysis of the bonding and the nature of the band gaps. They argue as presented in this chapter, for the very important role played by covalent bonding in these systems. They ascribe half-metallicity to arise in some of the $C1_b$ compounds due to the large Y-Z covalency, in conjunction with large exchange -splitting due to highly magnetic X ions.

This chapter focuses on chemical bonding in 8, 18-electrons and magnetic $C1_b$ compounds, and attempt to relate the electronic structure to simple concepts such as the electronegativity of the component species. The covalency and the local nature of the magnetic moment is discussed in the magnetic compounds using real-space descriptors derived from first principles theory.

5.2 Results and discussion

5.2.1 8-electron compounds

In this section, 7 compounds LiYZ with the $C1_b$ structure were investigated using LAPW and LMTO calculations. Results from the calculations are summarized in Table 5.1. The calculated cell parameters match very well with experimental cell parameters obtained from standard tabulations [167]. For LiMgN, the experimental cell parameter is from Kuriyama *et al.* [104] This suggests that in all cases, the assignment of atomic positions, which is not always a simple matter to determine from x-ray diffraction, is well justified.

In the three panels of Figure 5.1, density of states near the Fermi energy (taken as the top of the valence band, and set as the origin) are compared for 6 different LiYZ $C1_b$ compounds. In panel (a) of this figure two compounds LiMgN and LiMgBi are compared. Both compounds have a well defined band gap. Replacing N with the heavier pnictogens P, As, (DOS not shown) or Bi found to narrow the band gap due to the increasing band width of both the valence and conduction

[1] FLPW calculated results are listed in Appendix E

Table 5.1: Results of density functional calculations on LiYZ phases, with experimental cell parameters for comparison. Cell parameters and bulk moduli are from LAPW calculations, and band gaps from LMTO calculations.

8 electron compounds with X = Li							
XYZ	$a_{\text{Calc.}}$ (Å)	$a_{\text{Exp.}}$ (Å)	χ_X	χ_Y	χ_Z	Gap (eV)	B (GPa)
LiMgN	5.072	4.955	0.98	1.31	3.04	2.51	80.1
LiMgP	6.028	6.021	0.98	1.31	2.19	1.92	49.6
LiMgAs	6.218	6.19	0.98	1.31	2.18	1.55	42.9
LiMgBi	6.803	6.74	0.98	1.31	2.02	0.64	30.3
LiZnP	5.707	5.779	0.98	1.65	2.19	1.23	65.4
LiCdP	6.118	6.087	0.98	1.69	2.19	0.85	52.8
LiAlSi	5.937	5.930	0.98	1.61	1.90	0.45	62.8

bands. If the X and Z ions are held constant, as in LiMgP and LiCdP, it is observed that replacing the more ionic Mg by the softer Cd also results in a narrowing of the band gap. In panel (c) LiAlSi with isoelectronic Si are compared in the diamond structure. The electronic structures display a remarkable similarity in the nature and extents of the valence and conduction bands. This strong similarity has been noted previously by Christenson [34] and is fully in keeping with the description of LiAlSi being a Zintl or valence compound, [182] wherein the identical electron counts of $(AlSi)^-$ and (SiSi) in turn imply that the structures would be similar. It should be noted that Mg_2Si in the fluorite structure also obeys the same rule, it can be recast as $Mg^{2+}(MgSi)^{2-}$ with the $(MgSi)^{2-}$ crystallizing in a zinc blende lattice. Indeed the electronic structure of $MgSi_2$ [57] is quite similar to what found for LiAlSi. The change in the space group, comparing ($Fm\bar{3}m$) Mg_2Si and ($F\bar{4}3m$) LiAlSi arises because the atoms in the X and Y sites in the former are identical.

The similarity in the electronic structures of Si and stuffed zinc blende compounds is further emphasized through an analysis of the Si-Si, the Al-Si, and the Mg-N COHPs of the three different compounds: Si, LiAlSi, and LiMgN, shown in Figure 5.2. The dashed line in this figure is an integration of the COHP up to Fermi energy (ϵ_F), yielding a number that is indicative of the strength of the bonding. Not only are the extents of the bonding and antibonding COHPs of Si and LiAlSi very similar, but so is the value of the integrated COHP: near -1.5 eV *per* interaction for Si and for LiAlSi. This is interpreted as indicative of very similar extents of covalency in the diamond lattice of Si and the zinc blende sublattice of LiAlSi. This value is slightly reduced in the more polar LiMgN, and the nature of the COHP is different as well.

In Figure 5.3, the electron localization function (ELF) for the three compounds, Si, LiAlSi, and LiMgN are compared. Panels (a), (b), and (c) display isosurfaces of the electron localization function for values of 0.90, 0.90, and 0.825 respectively. These are high values of localization (the ELF scale as used here [152] runs from 0 through 1) and indicate highly covalent bonding between Si (cyan spheres) in the elemental structure, as well as between Al (blue) and Si (cyan) in LiAlSi,

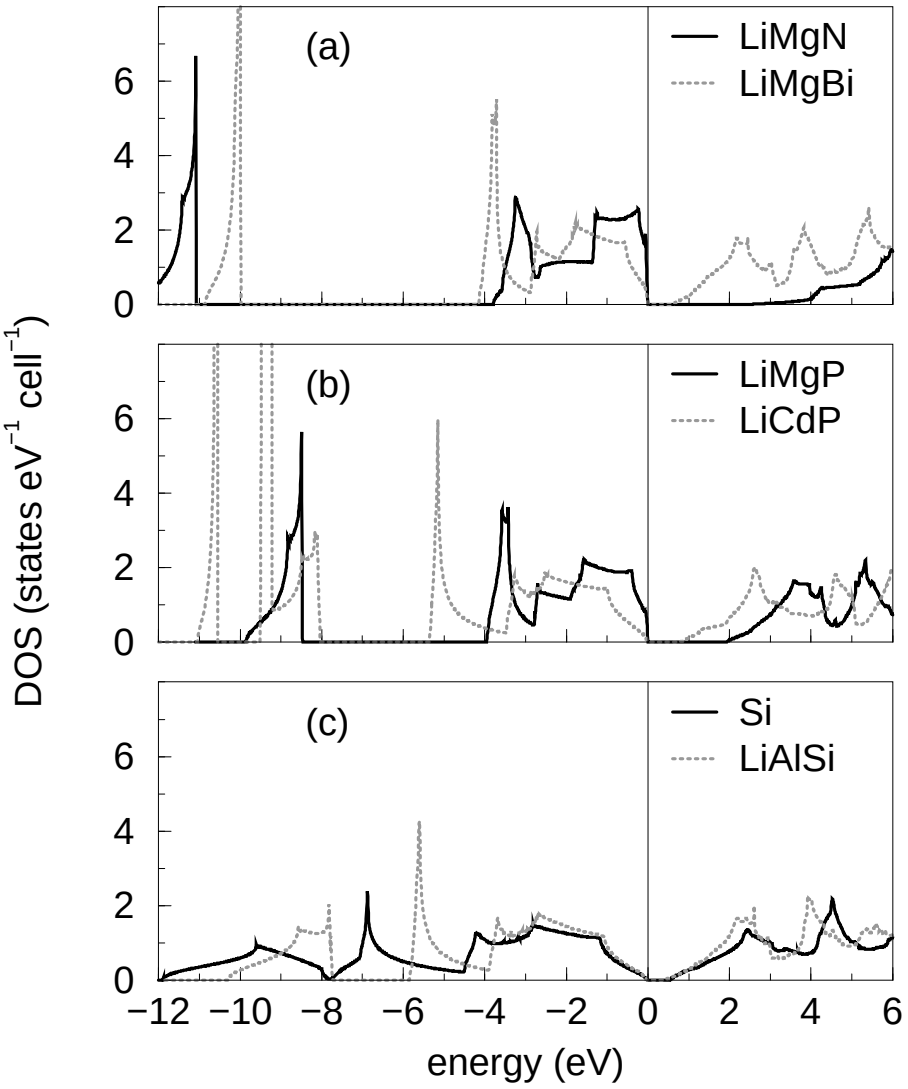

Figure 5.1: LMTO densities of state for a number of different Li-based $C1_b$ phases compared with Si (as diamond).

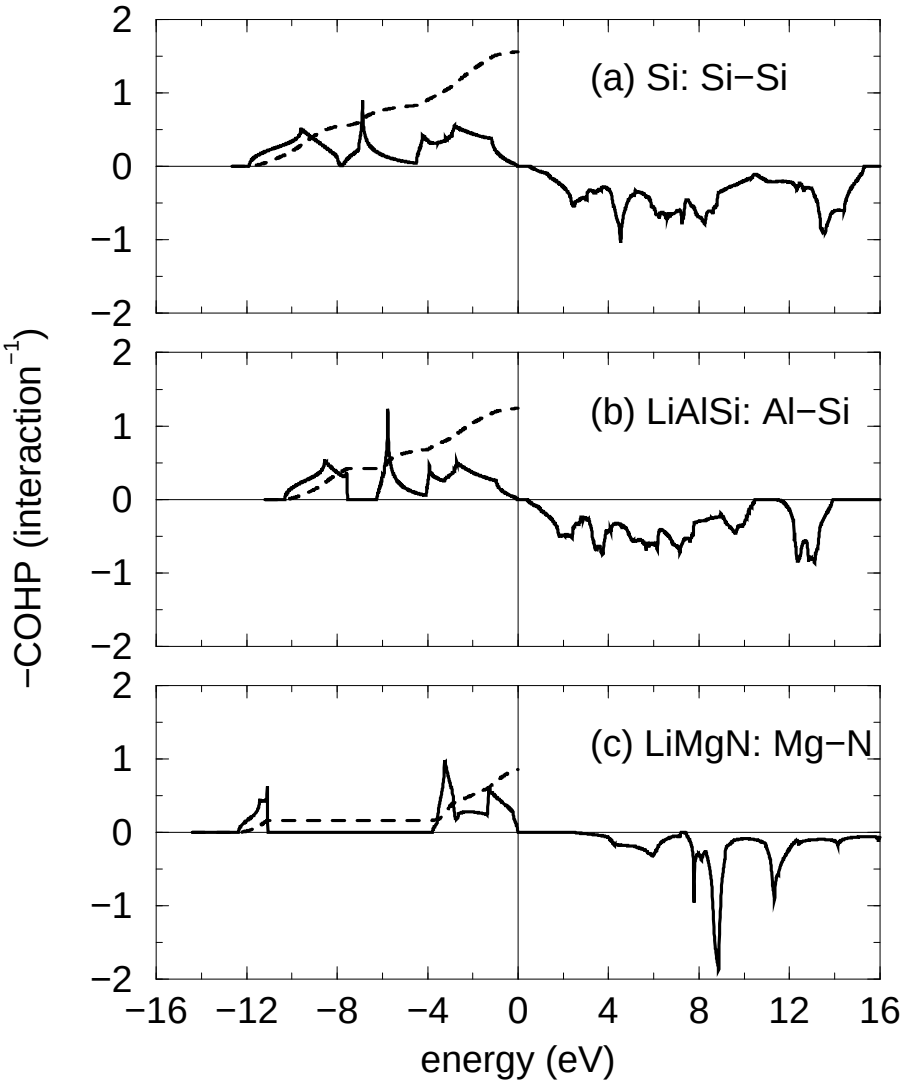

Figure 5.2: Crystal orbital Hamiltonian populations (COHPs) for pairwise interactions in diamond Si, LiAlSi, and LiMgN. The dashed lines are integrations of the COHPs.

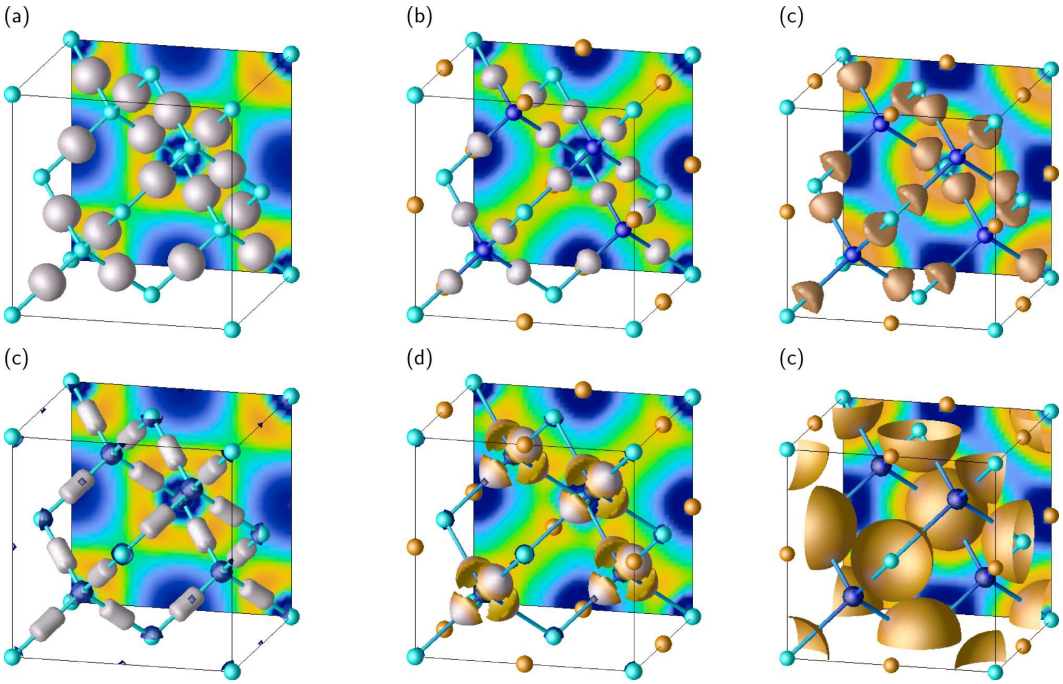

Figure 5.3: (a), (b), and (c) are electron localization isosurfaces for ELF values of 0.9, 0.9, and 0.825 respectively for the three compounds Si, LiAlSi, and LiMgN. (d), (e), and (f) are isosurfaces of constant charge density at a value of $0.06\,e\,\text{Å}^{-1}$. The isosurfaces are decorated by the value of the electron localization function. The color-bar at the bottom of the figure indicates increasing localization from left (0.0) to right (1.0).

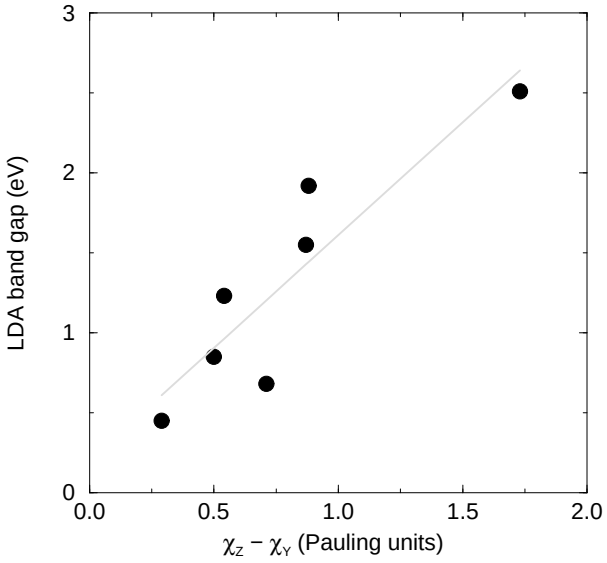

Figure 5.4: Dependence of the LMTO energy gap of LiYZ compounds on the difference in the Pauling electronegativities (χ) of the Y and Z species.

and between Mg (blue) and N (cyan) in LiMgN. The ELF takes on a curious hemispherical shape in LiMgN, reflecting the large electronegativity difference between Mg and N. The blob of localization is also closer to N than it is to Mg. It must be noted that there is no localization around Li (orange spheres) in either LiAlSi, or LiMgN, as seen also from the map of the ELF projected on the (010) plane at the rear of the unit cells. Li behaves effectively like ionic Li^+. In panels (d), (e), and (f) of this figure, isosurfaces of charge are displayed for a value of $0.06\,e\,\text{Å}^{-3}$ within the space of the unit cell. The charge isosurfaces have been decorated by the ELF. Bonds distort charges from being spherical, so distortions should be interpreted as covalency. Ionic species on the other hand, would have spherical charge around the nucleus. The highly covalent nature of the diamond lattice in Si, and the zinc blende sublattice in LiAlSi was observed. For LiMgN, while the bonding is still covalent, the charge is closer to the more electronegative nitrogen.

Having established that at least the XYZ $C1_b$ compounds with X = Li can be written $Li^+(YZ)^-$, to examine systematics in the band gaps of these compounds, data from Table 5.1 are used. It was found that the computed (LMTO) gaps of LiYZ to vary approximately as the difference of the Pauling electronegativities of Y and Z (Figure 5.4). The larger the difference in electronegativity of the species in the zinc-blende sublattice (Y and Z), the greater the band gap as a result of band narrowing. The trend cannot be used quantitatively, but only as and indicator of the Phillips-van Vechten-like [134] behavior that is seen in these complex semiconductors. It should be noted that the siting of Y in the tetrahedral position simultaneously allows the more polar pair

18 electron compounds with X = Y							
XYZ	$a_{\text{Calc.}}$ (Å)	$a_{\text{Exp.}}$ (Å)	χ_X	χ_Y	χ_Z	Gap (eV)	B (GPa)
YNiAs	6.104	6.171	1.22	1.91	2.18	0.53	100.0
YNiSb	6.350	6.312	1.22	1.91	2.05	0.28	92.8
YNiBi	6.475	6.411	1.22	1.91	2.02	0.13	80.9
YPdSb	6.599	6.527	1.22	2.20	2.05	0.16	92.0
YAuPb	6.842	6.729	1.22	2.54	2.33	0	70.6

Table 5.2: Results of density functional calculations for a number of 18-electron compounds with X = Y.

of X and Z to form a stable rock salt structure. From the viewpoint of lattice energy, this is perhaps the greater stabilizing influence on the C1$_b$ structure.

5.2.2 18-electron compounds

To examine whether similar rules hold for 18-electron C1$_b$ compounds, the results of density functional calculations on a series of XYZ compounds where X is electropositive yttrium are presented in Table 5.2. The zinc blende lattice is formed by a later transition metal Y, and a main group element Z. All the compounds are semiconductors according to LMTO calculations, with band gaps ranging from 0 eV for YAuPb to 0.53 eV for YNiAs. The existence of band gaps allows to formulate these phases according to the Zintl (or "extended Zintl") rule $X^{3+}(YZ)^{3-}$ where $(YZ)^{3-}$ becomes isoelectronic with a diamond-structure semiconductor such as GaSb. Once again, a simple trend was found that the band gap with the difference in electronegativities of Y and Z, as seen from Figure 5.5.

A systematic examination of the electronic structure of select 18-electron C1$_b$ compounds with different X, Y, and Z elements have been carried out. Figure 5.6(a) displays the LMTO densities of state VFeSb, TiCoSb, and YNiSb, allowing the trends with changing the later transition metal Y to emerge. Projections of the densities of state on the different atomic levels (not displayed) reveal that the valence band has Y d character and Z p character. The conduction band has some of the character from these states, but in addition, has empty d states from the X atom. This fits with the expectation of the X atom being nearly fully ionized (or more accurately, having attained the group valence) and the d shell of the Y atom being filled as a result. The gap is largest for TiCoSb, and smallest for YNiSb. When both X and Y are changed, it is more difficult to seek trends in the gap. The gap in VFeSb is reduced due to V and Fe not being well separated in electronegativity. The gap in YNiSn is reduced because the unoccupied Y 4d states are rather broad, at least within LSDA. What is evident is that compounds with Co on the Y site have a strong propensity to maintain "clean" gaps as further seen in panel (b) of this figure where the DOS of TiCoSb, VCoSn, and NbCoSn are displayed.

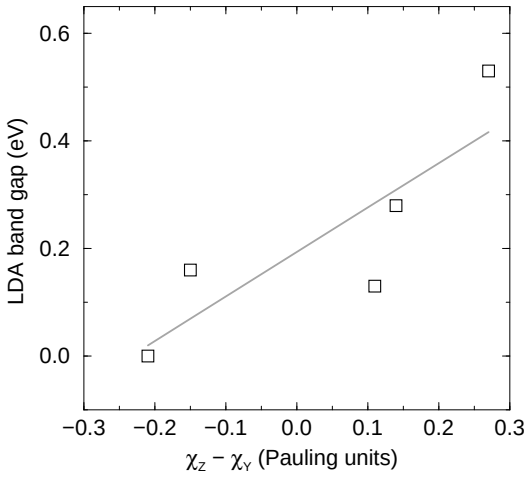

Figure 5.5: Dependence of the LMTO energy gap of YYZ compounds on the difference in the Pauling electronegativities (χ) of the Y and Z species.

A bonding analysis based on COHPs was performed for these transition-metal rich phases (Figure 5.7). These are shown for all pairwise interactions in the two $C1_b$ compounds VFeSb and TiCoSb. Integrating the COHPs, the strongest bonding interactions are found in between Y and Z (Co and Sb, and Fe and Sb) while the interactions between the early and late transition metal (Ti and Co, and V and Fe) are also significant. The compounds are electronically very stable as seen from a complete absence of any antibonding interaction below the top of the valence band. The fact that the 18-electron compounds are clearly valence compounds with the band gap being located between bonding and antibonding levels supports our description of these phases being Zintl-like. The band gaps in VFeSb and TiCoSb would seem to be determined by bonding between X and Y, so at first sight, it would seem that at least these two transition-metal rich phases should not be described simply as cation-stuffed zinc blendes. However, it will be seen from the ELF analysis, the *localized* bonding remains in the zinc blende YZ lattice. Weak bonding and antibonding COHPs between X and Z (Ti and Sb, and V and Sb) support the view that the XZ rock salt sublattice is ionic in character.

Figure 5.8, displays electron localization functions for the two 18-electron $C1_b$ compounds for which the COHPs are displayed in Figure 5.7, namely TiCoSb and VFeSb. The ELFSs, visualized respectively, for values of 0.73 and 0.71 in Figure 5.8(a) and (b) are clearly indicative of strongly covalent bonding in the zinc blende sublattice, with TiCoSb displaying the greater tendency to covalent bonding. As one observed in the 8-electron compounds, localization isosurface is closer to the more electronegative Sb atoms. It must be pointed out that the ELF is notoriously difficult to apply in d electron system, and the fact that the localization emerges so clearly here is compelling

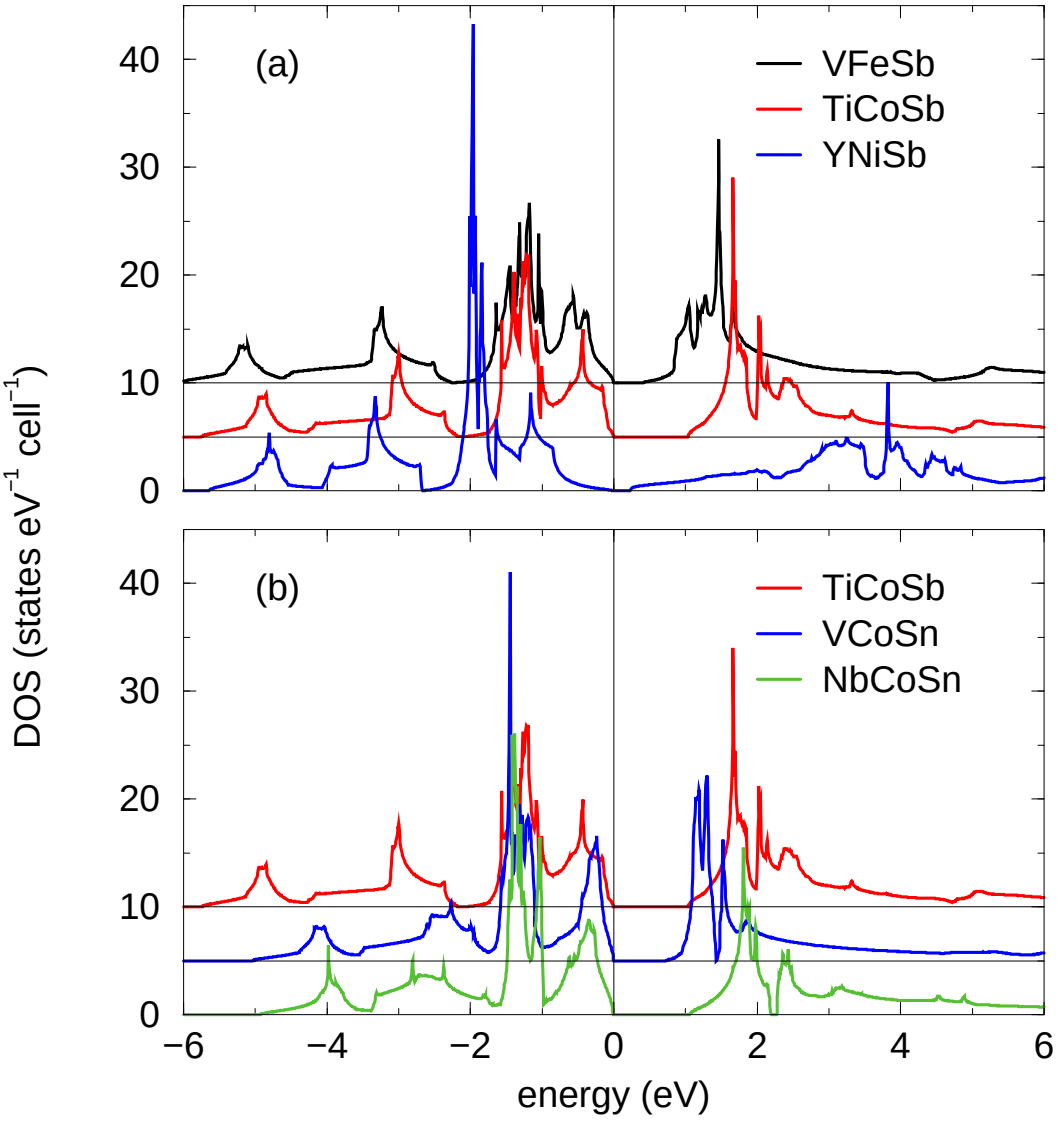

Figure 5.6: LMTO densities of state for the 18-electron $C1_b$ compounds (a) VFeSb, TiCoSb, and YNiSb, showing how changing the nature of the Y atom affects the band gap, and for (b) TiCoSb, VCoSn, and NbCoSn emphasizing the propensity of Co-based $C1_b$ compounds to posses a "clean" gap. The plots have been offset for clarity.

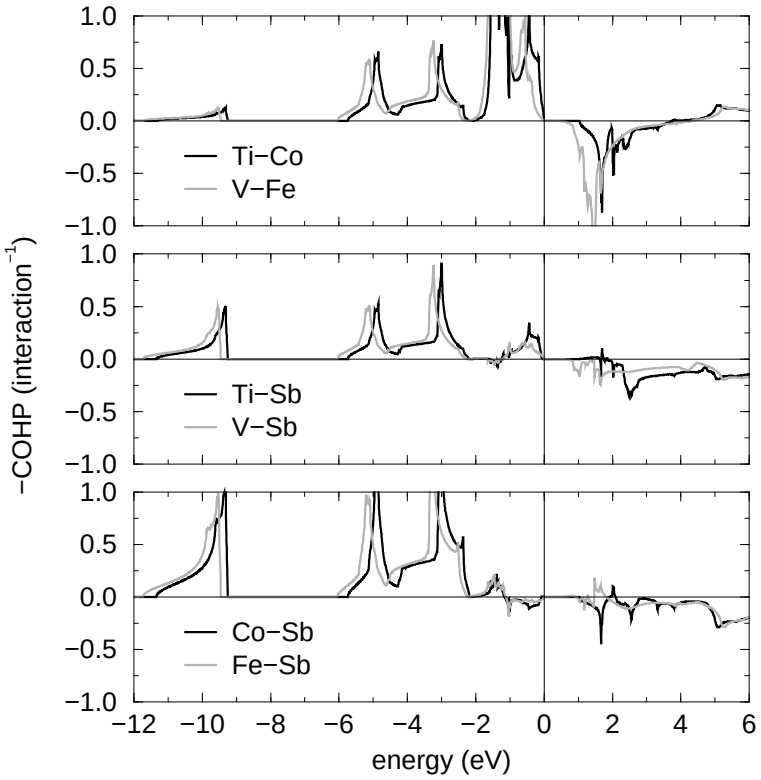

Figure 5.7: Crystal orbital Hamiltonian populations for all pairwise interactions in VFeSb and TiCoSb.

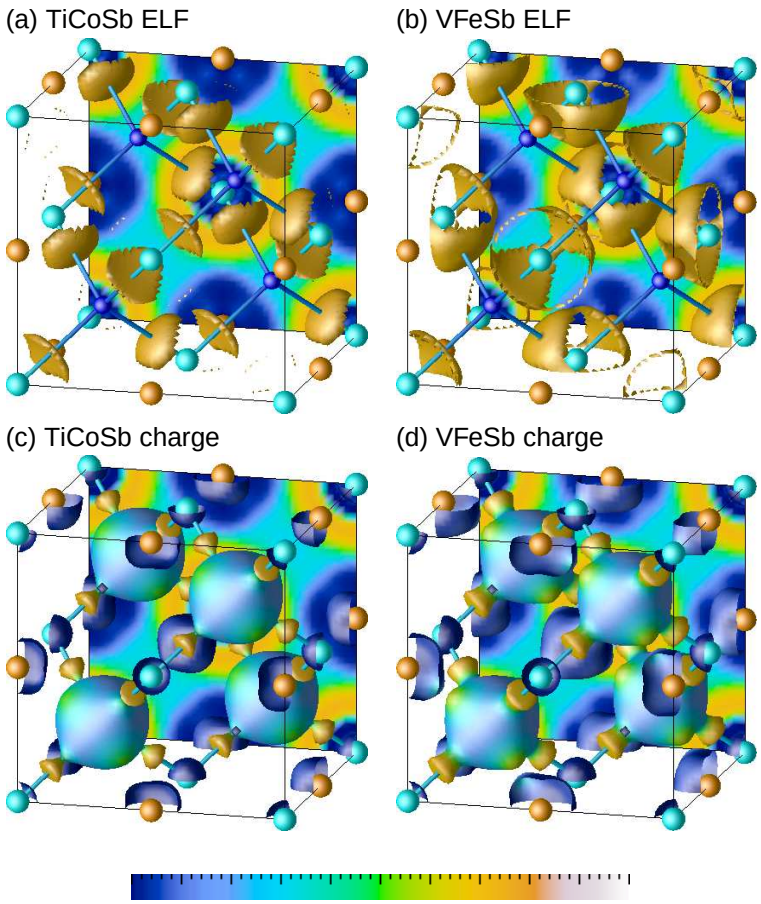

Figure 5.8: (a) and (b) are ELF isosurfaces for TiCoSb and VFeSb for values of 0.73 and 0.71 respectively. (c) and (d) are charge densities for a value of $0.06\,e\,\text{Å}^{-3}$, decorated by the ELF.

evidence for dealing with these systems as if they were valence compounds with strongly covalent bonding.

The valence charge densities displayed in Figure 5.8(c) and 9(d) are very distinct from what was seen for the 8-electron compounds, because the filled d shell on Y forms a large nearly spherical blobs around that atom, visualized for a charge density of $0.06\,e\,\text{Å}^{-3}$. One can find that these blobs of charge are pulled out into four strongly localized (as seen from the coloring) lobes arranged tetrahedrally and facing Z. Interestingly, in VFeSb, there is also some d-like localization around V, and there is some little localization seen on the isosurface between V and Fe. The smaller electronegativity difference between V and Fe, when compared with the electronegativity difference between Ti and Co, in conjunction with the nature of COHPs displayed in Figure 5.7 leads to point this out as the origin for the smaller band gap of VFeSb. Another argument that one can proffer is that TiCoSb has greater polar intermetallic character, [1, 21, 26] with strong Ti-Co bonds that are

XCoSb					
X	$a_{\text{Calc.}}$	$a_{\text{Exp.}}$	B (GPa)	n_V	M
Sc	6.095	N.A.	110.5	17	0
Ti	5.888	5.884	151.5	18	0
V	5.823	5.802	150.8	19	1
Cr	5.820	N.A.	135.4	20	2
Mn	5.810	5.875	139.1	21	3

Table 5.3: Optimized (LAPW) and experimental cell parameters for C1$_b$ compounds XCoSb. The computed bulk moduli are also indicated. n_V is the number of valence electrons and M is the magnetic moment obtained from LMTO calculations.

heterocovalent. V and Fe are closer together in electronegativity, and the high formal charge state (V^{5+}) is much more covalent. This results in a smaller band gap in VFeSb.

In the next subsection, these simple ideas of covalent bonding are carried over to the important magnetic C1$_b$ compounds.

5.2.3 Magnetic compounds

The results of LAPW optimization of XCoSb compounds are presented in Table 5.3, with experimental cell parameters presented for comparison for the known compounds (X = Ti, V, and Mn). The table also presents the computed (LAPW) bulk modulus, which is seen to go through a maximum for TiCoSb, associated, as would be observed in the COHPs, with a completely filled *bonding* valence band and an empty, *antibonding* conduction band. Figure 5.9 displays densities of state for XCoSb phases with X = Sc, Ti, V, Cr, and Mn. The number of valence electrons n_V per formula unit are indicated within each panel. The DOS are plotted in the two spin directions in each panel, even for the non-magnetic compounds. The compound ScCoSb is not known, and neither is CrCoSb. The non-existence of CrCoSb could be associated with the high peak in the densities of state at ϵ_F or this compound. The (hypothetical) compound ScCoSb is non magnetic within LMTO-LSDA because the bands are too broad for the Stoner criterion to be fulfilled.

All compounds except ScCoSb obey the Slater-Pauling rules for cubic C1$_b$ compounds, $M = n_V - 18$. TiCoSb with $n_V = 18$ is a non-magnetic semiconductor, and the calculated moments (Table 5.3) for VCoSb, CrCoSb, and MnCoSb are precisely 1, 2, and 3 μ_{B}. This means that these three compounds are half-metals, as seen from the densities of states in Figure 5.9. In particular, CrCoSb, and MnCoSb have "clean" gaps in the minority spin direction. With increasing n_V, it was noticed that the d states above the ϵ_F, which are derived from the electropositive X atom drop down with respect to the filled d states on Co both because of their partial filling as well as because of the well known tendency of transition metal d levels to be stabilized in energy on going across the d series [87, 180]. One of the consequences of the narrowing of the d separation between Y and X

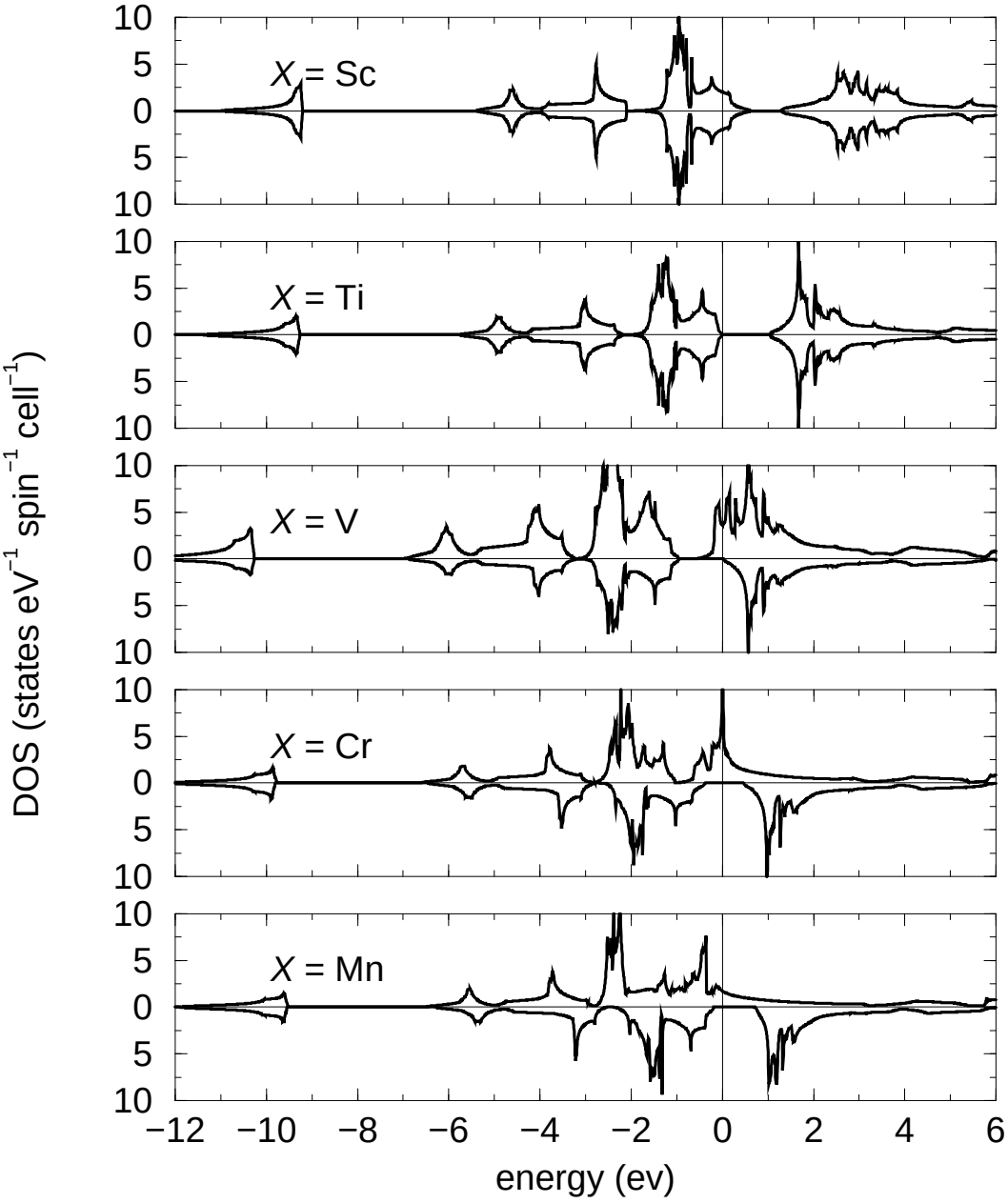

Figure 5.9: Densities of state of the $C1_b$ compounds XCoSb, plotted separately in the two spin directions.

is that for larger valence electron counts than 21 or 22 (found when Y = Ni), cubic C1$_b$ compounds become unstable with respect to other structure types.

In the different panels of Figure 5.10, COHPs for X-Co, X-Sb, and Co-Sb interactions (X = V or Mn) are displayed. These are half-metallic ferromagnets with 19 (VCoSb) or 21 (MnCoSb) so the COHPs are spin-resolved. While the X-Sb interaction within the rock-salt sublattice is clearly negligible, both X-Co and Co-Sb are seen to be important. The X-Co interaction is seen to be highly spin-polarized. The origin of the half-metallicity is revealed by the clear separation of antibonding *majority* states which cross the ϵ_F from the antibonding *minority* states which are separated by a gap equal to the exchange energy. This allows to make the following generalization: The 18-electron cubic C1$_b$ compounds are the most stable phases, with well separated bonding and antibonding states. Additional electrons (more than 18) must go into antibonding states and these are split by spin-polarization and separated into majority and minority states. While these compounds are intrinsically less stable than the 18-electron compounds, they maximize their stability by ensuring that minority antibonding states remain unoccupied. The Co-Sb interaction in these two compounds is seen to be strongly covalent, but not very much affected by spin-polarization. There remains a clear separation of bonding from antibonding states as was observed in the 18-electron semiconductors.

Real-space visualizations of the electronic structure in Figure 5.11 reveal that even in the magnetic compounds XCoSb with X = V or Mn, the ELFs are strongly localized on the bonds of the zinc blende CoSb network. As could be anticipated from the similarities in the COHPs, there is almost no change in the Co-Sb localization pattern on going from 19-electron VCoSb to 21 electron MnCoSb [Figure 5.11(a) and (d)]. There is a strongly localized region slightly closer to the more electronegative Sb atoms in both these compounds. Again, the charge density decorated by the ELF [(b) and (e)] confirm this localization. The d electron density around Co is spherical apart from the four lobes facing Sb. What is interesting is that the magnetic moment, as visualized from an isosurface of constant spin density is clearly located on the stuffing X atom in both in VCoSb and in MnCoSb, as seen in Figure 5.11(c) and (f). The magnetic C1$_b$ compounds can therefore be regarded as zinc-blende lattices of a late transition metal and a main group element, stuffed by relatively electropositive magnetic ions. Despite the presence of magnetic X^{n+} transition metal ions, the YZ^{n-} network can still be described in simple valence terms. This is reminiscent of compounds prepared by Kauzlarich and coworkers [103, 148] wherein magnetic ions such as Mn^{3+} are found to behave like electropositive cations such as Al^{3+} which donate charge to an anionic sublattice which is in turn a closed shell.

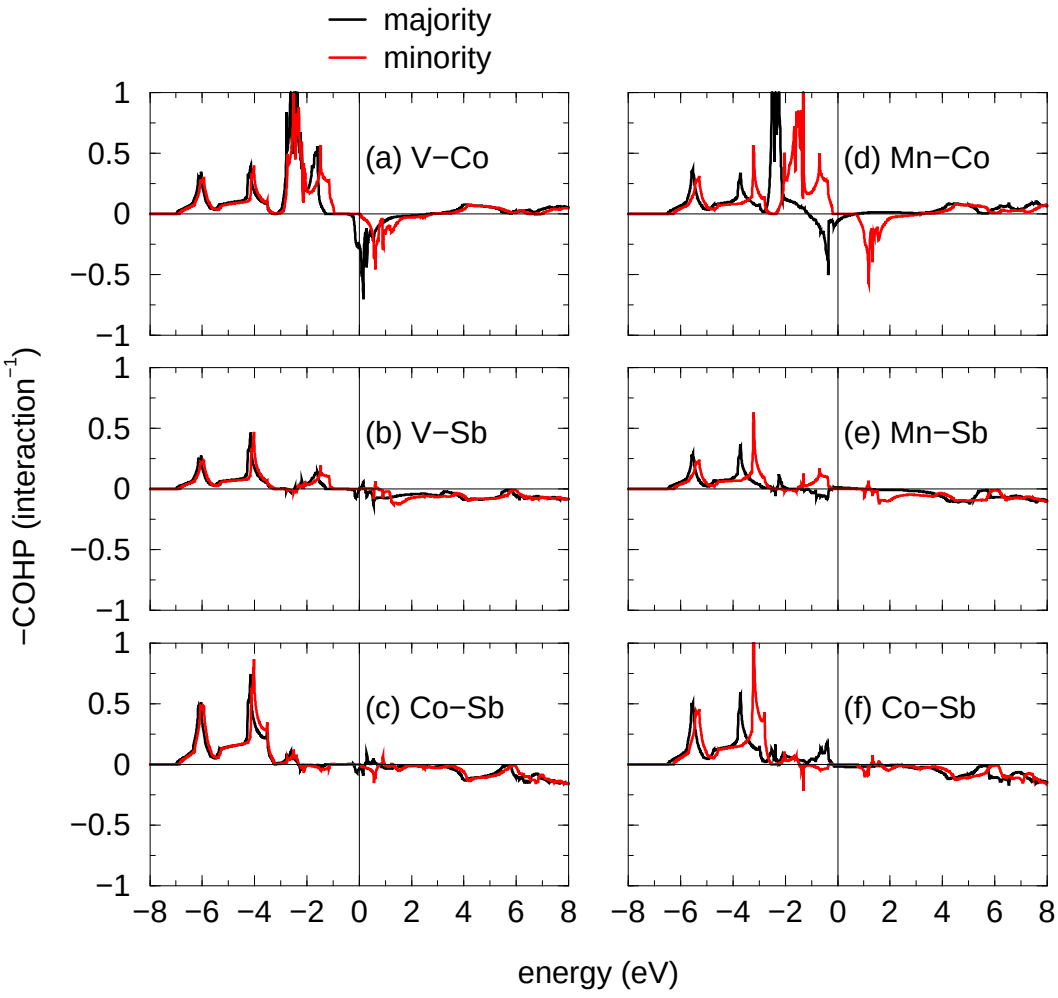

Figure 5.10: COHPs of VCoSb and MnCoSb in the two spin directions. In the absence of spin-orbit coupling, majority and minority spin states do not interact.

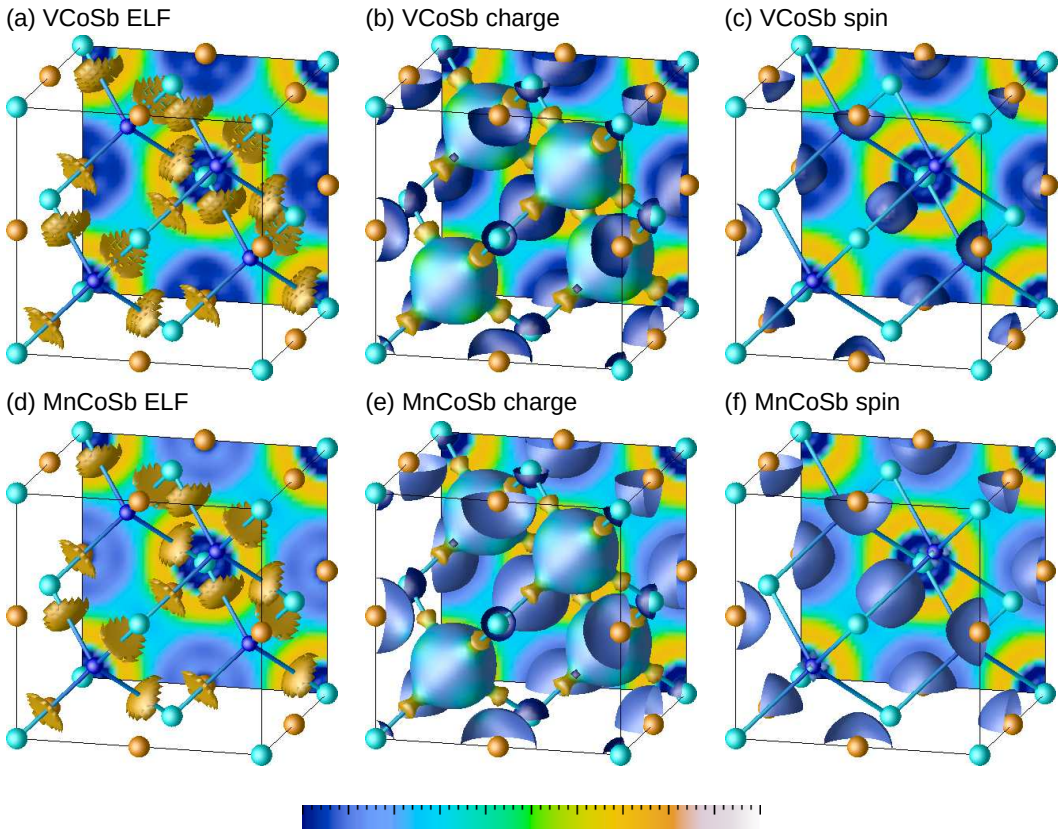

Figure 5.11: (a) and (d) are ELF isosurfaces for VCoSb and MnCoSb for ELF values of 0.71. (b) and (e) are charge densities for a value of $0.06\,e\,\text{Å}^{-3}$, decorated by the ELF. (c) and (f) are isosurfaces of constant spin of value $0.05\,\text{spins}\,\text{Å}^{-3}$.

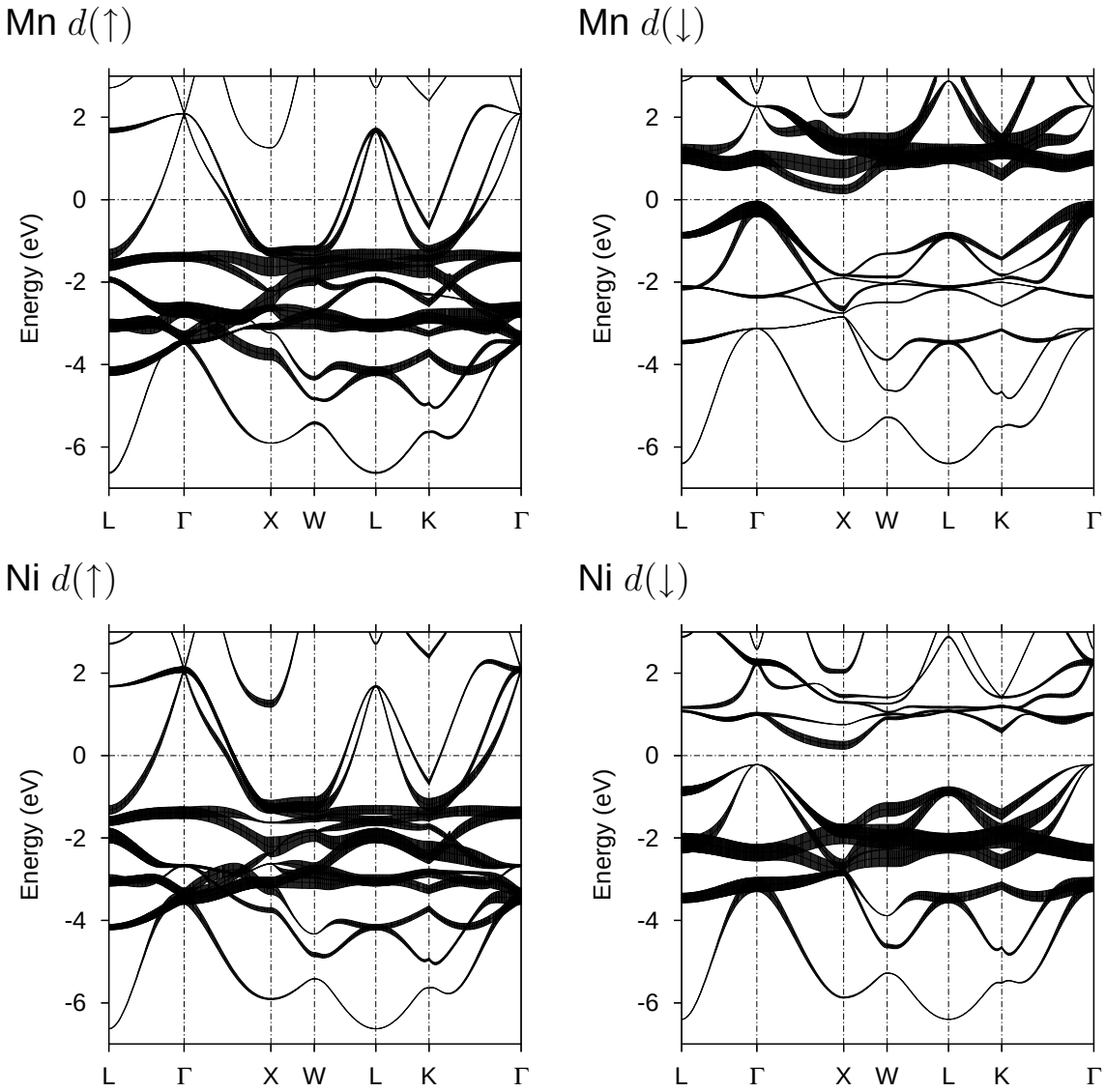

Figure 5.12: (a) Partial DOS of the different states (indicated) in MnNiSb, in the two spin directions. (b) COHP showing Mn-Ni interactions in the two spin directions. The Mn-Ni COHP for the nonmagnetic MnNiSb is also displayed.

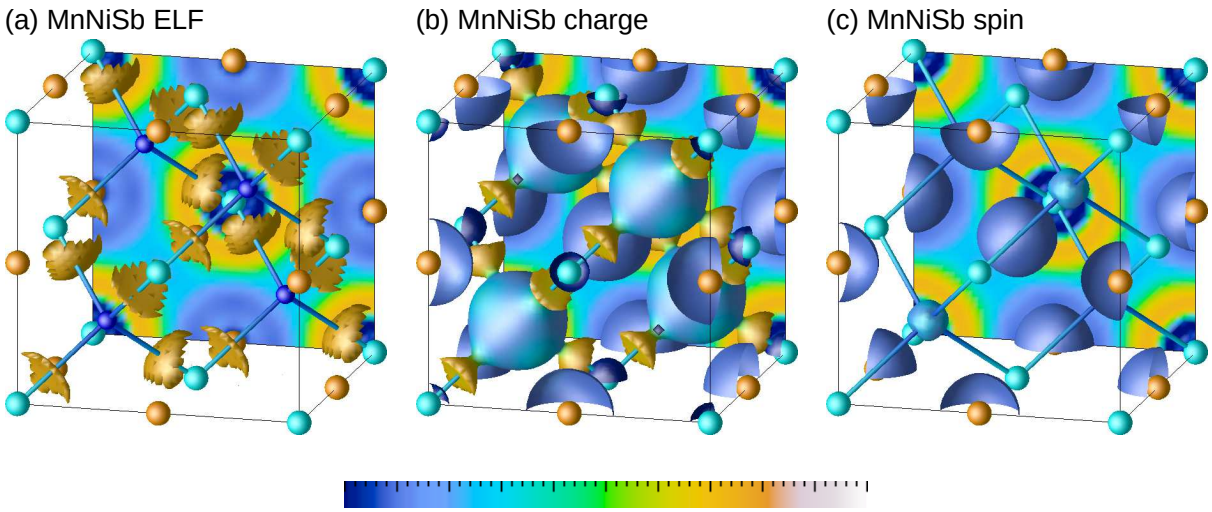

Figure 5.13: (a) is ELF isosurfaces of MnNiSb for an ELF value of 0.73. (b) is the charge density isosurface for a value of $0.055\,e\,\text{Å}^{-3}$, decorated by the ELF. (c) is an isosurfaces of constant spin density corresponding to $0.05\,\text{spins}\,\text{Å}^{-3}$.

5.2.4 MnNiSb

For completion, the electronic structure of the canonical 22-electron $C1_b$ compound, MnNiSb [41] is discussed in this subsection. Partial density of states for this compound are displayed in Figure 5.12(a). The partial DOS have been offset for clarity. Mn d states are seen to approximately half-full (expected for d^4 Mn^{3+}) and strongly spin-polarized with an exchange splitting of more than 3 eV. While The Mn can be regarded as tetrahedral in the $C1_b$ compounds, it is difficult to ascertain a crystal field. Looking at filled, spin up Mn states, it would seem that the crystal field splitting is approximately 1 eV. This splitting is not observed in the Mn minority d states. While a few Ni d states are found at ϵ_F, and beyond, the d manifold of Ni is mostly filled, in keeping with what was observed for the Co compounds such as MnCoSb. The extent of spin-polarization on Ni is therefore much less than on Mn. Sb p states are almost fully filled.

Mn-Ni COHPs in the two spin directions are displayed in Figure 5.12(b). It is seen that both magnetism and conductivity are dominated by Mn-Ni interactions. Majority Mn-Ni interactions are both bonding and antibonding below the ϵ_F while Mn-Ni antibonding interactions are all above ϵ_F Note that the minority antibonding interactions are not at all strong, suggesting why these states do not display any crystal field splitting. Comparing the COHP in ferromagnetic MnNiSb with non-magnetic MnNiSb is instructive. It is seen from Figure 5.12(b) that the effect of exchange splitting is to repartition antibonding states at the ϵ_F into filled majority and empty minority states, thereby increasing the total bonding in the unit cell. This exchange gap creates a half-metal.

Real-space visualizations of the electronic structure of MnNiSb in Figure 5.13 confirm what

was seen for MnCoSb; that the covalent zinc blende YSb network is retained, and the stuffing Mn is quite ionic, with spin density mostly localized around it. At the selected spin density, there is some small localization around Ni as well.

5.3 Summary

A systematic examination have been carried out for XYZ cubic $C1_b$ compounds that are 8- and 18-electron semiconductors or half-metallic ferromagnets when the electron counts are other than 18. It was found that the most illuminating way of considering these systems is to think of them as being built up of a zinc blende YZ framework that is stuffed with a (more) electropositive X ion that can also be magnetic. The tendency of the zinc blende sublattice is to open up a semiconducting gap provided the correct (8- or 18-) electron count is carried over to the half-metallic compositions, except that the semiconducting gap becomes the half-metallic gap. This suggests that an effective strategy for new half-metals might be to look for semiconductors which can be 'stuffed' by magnetic ions.

Chapter 6

GdPdSb: a possible half-metallic weak ferromagnet at low temperature

6.1 Introduction

A class of compounds that has attracted a great attention in recent years is $REYZ$, where RE is a lanthanide element, Y a transition element and Z a main group element. This class offers a broad variety of different structure types [72, 143] with interesting electronic and magnetic properties that are heavy Fermion behavior [43, 97], half metallic properties (Ce based compounds) [58, 158], mixed valent behavior in Eu, Yb and Ce compounds [2, 27, 36, 55, 100, 163], giant magneto resistance [139], superconductivity [27, 111], etc. Usually $REYZ$ order magnetically at low temperatures due to the magnetism confined to the rare earth sublattice.

Approximately 50 hexagonal $REYZ$ compounds crystallize in the LiGaGe structure, which can be thought of as a RE^{n+} ion stuffing a wurtzite $(YZ)^{n-}$ sublattice. In the past few years, many $REYZ$ compounds were determined as in the $CaIn_2$ structure type (random distribution of Y and Z atoms). Later it was found that their correct structure is LiGaGe type with Y and Z atoms form separate lattices [9, 10, 11, 30]. Its crystal structure is completely described by four parameters, the hexagonal cell parameters a, c and the internal Y and Z atoms positional parameter z in $(\frac{1}{3}, \frac{2}{3}, z)$ (Chapter 3). Their electronic structure properties depend on the internal z parameter. If the hexagonal sheets comprise Y and Z atoms are planar (graphite-type sheets), then the bonding interaction is exclusively within the layers. For the compounds of 18 valence electrons, the electronic

structure	energy/eV
ferromagnet	-1240937.183
antiferromagnet	-1240937.258

Table 6.1: Total energies for the different magnetic structures of GdPdSb

structure is two-dimensional and shows only a pseudogap at ϵ_F. Increasing the interaction between the layers (by means LiGaGe) by puckering the layers opens a gap at ϵ_F, leading to a semiconducting behavior. It seems puckering of the layers not only stabilizing the structure but it also affects the electronic properties. A number of experimental studies has been carried out on LiGage structure type compounds. For example, Baran *et al.* [7, 8, 10, 184] have observed antiferromagnetic transition at low temperatures for RASn (R = Gd-Er, A = Cu and Ag) ternary compounds. Later Casper *et al.* [31] have systematically studied the structural and magnetic behavior of GdAuSn compound.

A deeper understanding of the electronic structure of such complex compounds has become important both from a fundamental and materials science point of view. This research focuses on the GdPdSb compound with LiGaGe structure type which exhibits antiferromagnetic behavior at low temperature.

6.2 Results and discussions

To explore the possibility of ferromagnetism in the hexagonal compound GdPdSb, FLAPW total energy calculations were performed for an antiferromagnetic and ferromagnetic structures using the program Wien2k. The calculated total energy for the antiferromagnetic structure is slightly lower than the one for ferromagnetic structure (Table 6.1). Since the difference between the energies is marginal, one could expect a ferromagnetic ordering in the ground state. Such type of energy dependent magnetic structure was also observed by Felser *et al.* for layered compound $LaSr_2Mn_2O_7$ [56]. The antiferromagnetic structures were obtained by constructing a hypothetical supercell of GdPdSb by doubling lattice parameters in all the three directions. Where Gd atoms lying in one planes are aligned parallel to each others and the next nearest neighbor Gd atoms are aligned in opposite direction. Such arrangement of spins of Gd atoms avoid the possibility of spin frustration state within triangular network of Gd atoms.

The calculations of the DOS and band structure for this compound in the ferromagnetic state was based on the experimental crystal structure. The band structures of anti-ferromagnetic and ferromagnetic GdPdSb are displayed in Figure 6.1 and Figure 6.2 respectively. In Figure 6.1 only majority band structure is shown for antiferromagnetic GdPdSb because they are similar to the minority band.

The band structures are shown along Λ and Δ directions for both anti-ferromagnetic and

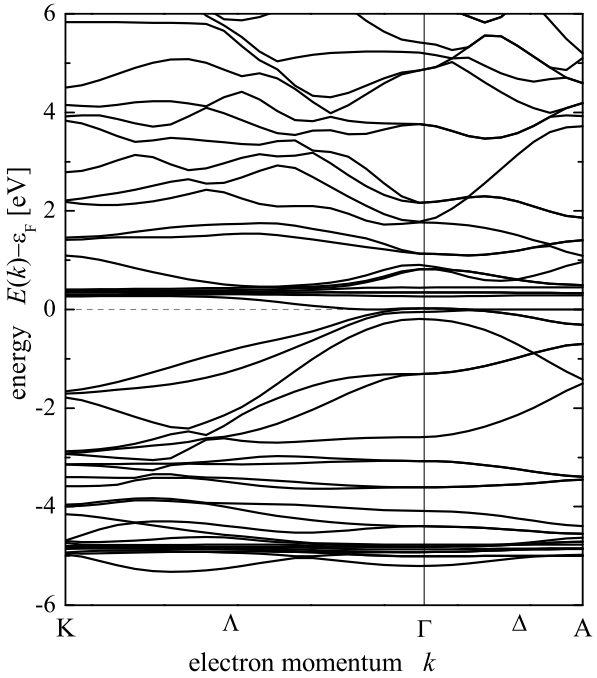

Figure 6.1: LAPW spin resolved band structure of antiferromagnetic GdPdSb for spin-up states

ferromagnetic GdPdSb. From the spin-resolved bands of antiferromagnetic GdPdSb, it is seen that the majority bands cross or touch the ϵ_F at Γ point in k-space and shows a clear gap in all directions of high symmetry. A pseudo gap appears close to the ϵ_F for antiferromagnetic structure. The band structure of ferromagnetic GdPdSb reveals a gap in minority bands and metallic behavior in majority bands. Most of the flat bands are above the ϵ_F. Indeed, the gap in minority bands is very small as one can find for such systems without considering the Coulomb correlation of the Hubbard U-type in the calculations.

Next, the density of states (DOS) of ferromagnetic GdPdSb is studied with and without considering electronic correlation. Figure 6.3 compares the total density of states of GdPdSb from spin polarized within (a) GGA, (b) LDA + U and (c) SPKKR methods. The values of Coulomb (U) and exchange (J) interaction energies were taken 6.70 eV and 0.70 eV respectively. These values are based on the literature and later were confirmed by results of photoemission experiments [30]. In both plots, ϵ_F is taken as the origin on the energy axis. The upper panel of each plot displays majority (up) spin density and the lower panel minority (down) spin density.

In Figure 6.3(a), total and partial DOSs of Gd-f, Pd-d, and Sb-p states for ferromagnetic GdPdSb are displayed. The filled Gd-f states are appeared at approximately -5 eV below the ϵ_F and are well localized. These Gd-f states are split with a separation of 5 eV. Gd-f spin-down states are just above the ϵ_F at 0.1 eV. One could think that the Gd-f states might mixed with the other states at ϵ_F, which is not realistic because of their strong localization behavior. To avoid mixing

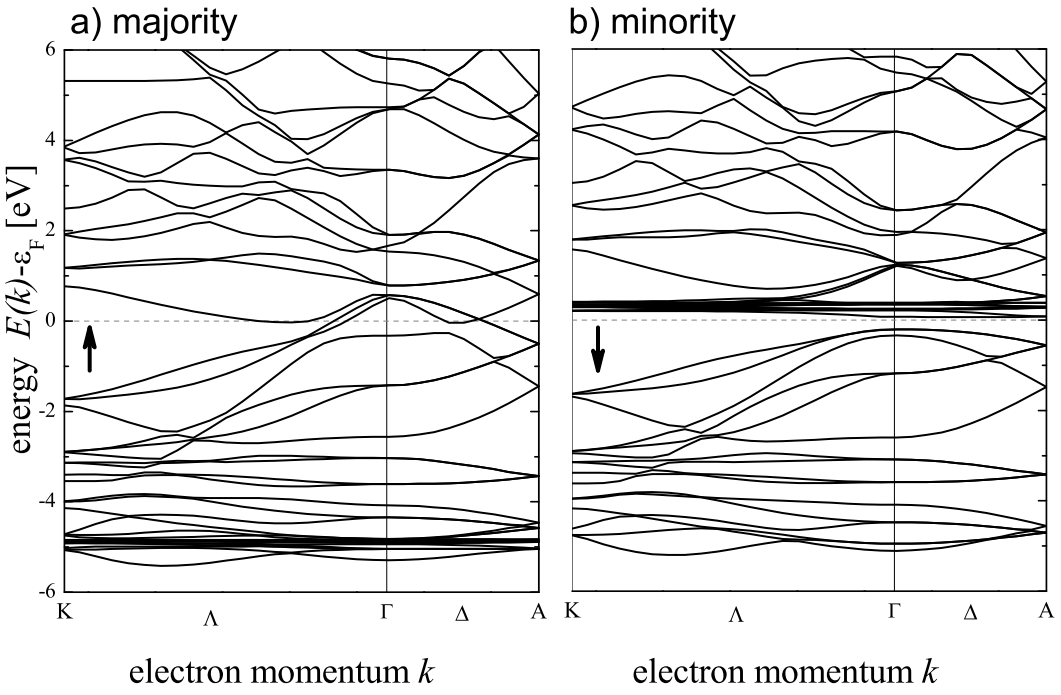

Figure 6.2: LAPW spin-resolved band structure of ferromagnetic GdPdSb for spin-up and spin-down states

of Gd-f states to the other states at the ϵ_F, electronic correlation is used in the calculation. The corresponding total DOS is displayed in Figure 6.3(b). When LDA+U is used, the Gd-f states shift away from ϵ_F and centered at approximate -8 eV below ϵ_F. This implies that the Gd-f states of GdPdSb are highly localized and hardly affect the other states near the ϵ_F. There are no minority states appear at the ϵ_F confirming that the compound is a half metal. Differences due to the addition of correlation in the two plots arise only as a result of larger splitting between occupied and unoccupied Gd-f states in panel Figure 6.3(b). The important conclusion that can be drawn from the DOS of GdPdSb is that states at and near ϵ_F are spin polarized and the system may represent half metal. The spin polarized calculations for GdPdSb yield a magnetic moment of 7 μ_B per formula unit. This is expected for a half-filled f band.

The fully relativistic calculation using the SPRKKR method (shown in Figure 6.3(c)) reveals a splitting within the $4f$ bands. The semi-conducting minority gap becomes closed by Gd-f bands crossing ϵ_F in the Δ direction. The reason is that in full relativistic calculations, due to the coupling between spin-up and spin-down states a very small DOS persist at ϵ_F.

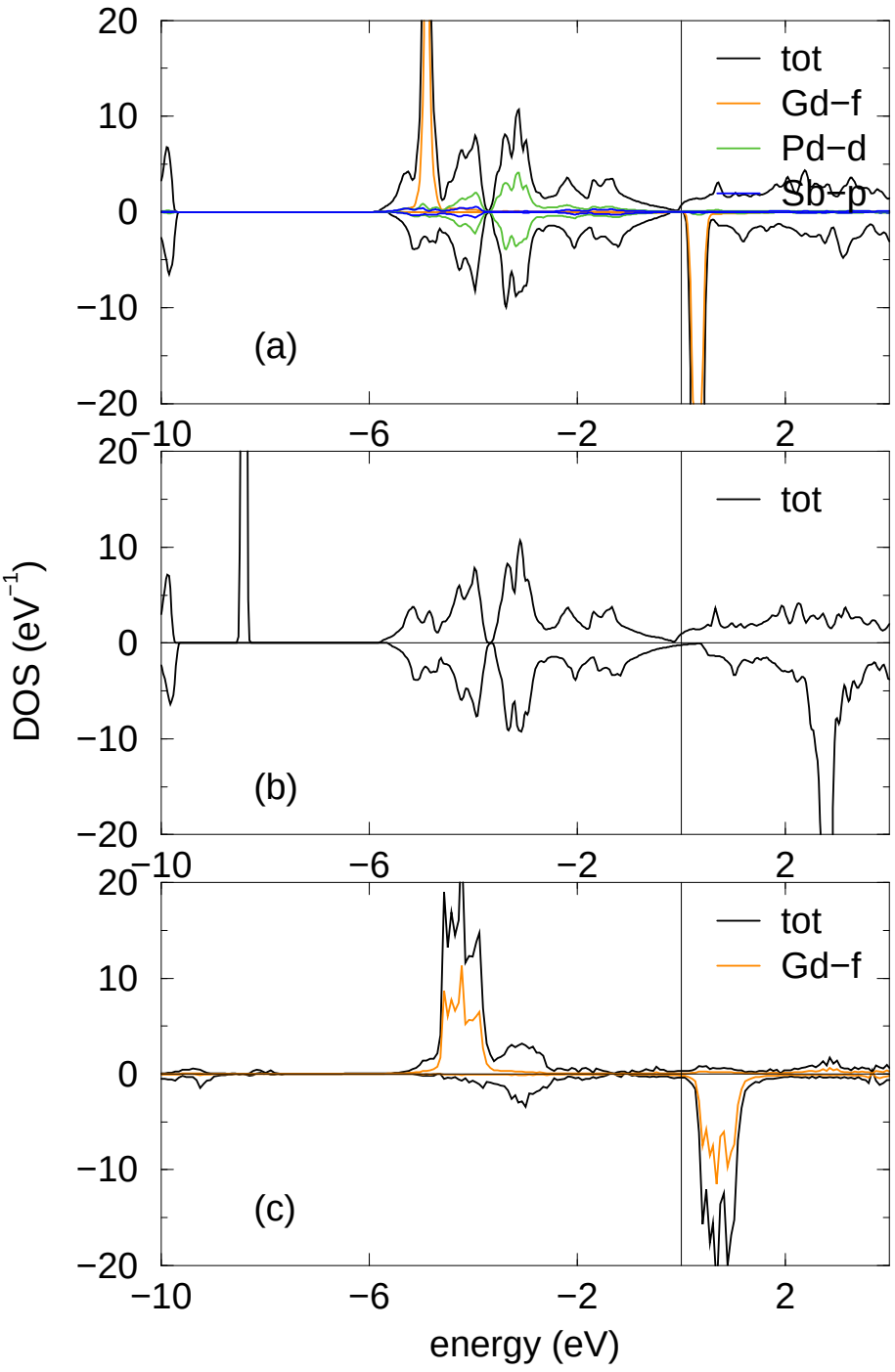

Figure 6.3: The projected density of states within (a) GGA, (b) LDA + U and (c) SPKKR for GdPdSb. Spin up states are shown in the the upper portions and spin down states in the lower portions in each panel. The origin on the energy axis is the ϵ_F.

6.3 Summary

The electronic band structure calculations show only a marginal energy difference between ferromagnetic and antiferromagnetic states. These finding indicates a possible ferromagnetic and half metallic behavior for GdPdSb. Finally, it has been found that GdPdSb is a weak ferromagnet at T $<$ 10 K, similar kind of magnetic behavior was also reported by Augsburger *et al.* in double perowskit Ca_2CoTeO_6 below 10 K [6]. Apparently, the position of Gd-f states was verified by the photoemission experiments [30].

Chapter 7

Variation of the bonding interactions in GdAuX (X = Mg, Cd, and In)

7.1 Introduction

Intermetallic gadolinium compounds are promising candidates for magnetocaloric materials (magnetocaloric effect; MCE) [90, 127, 128]. The recent developments in this field have been reviewed and can be found in Ref. [91]. Although gadolinium and gadolinium-based solid solution alloys are the excellent candidates for MCE materials, some intermetallic gadolinium compounds show adiabatic temperatures that are up to 30 % higher than those for elemental gadolinium. A highly interesting compound in that respect is the giant-MCE material $Gd_5Ge_2Si_2$ [127]. Another class of materials concerned the Fe_2P related pnictide solid solution $MnFeP_{0.5}As_{0.5-x}Ge_x$ [24]. Recently, Pöttgen *et al.* has started a more systematic investigation of the structure-property relations of Fe_2P / ZrNiAl related gadolinium intermetallics. The isotypic compounds GdAuIn [144], GdAuMg [105], and GdAuCd [106] show distinctly different magnetic ordering temperatures of T_N = 12.5 K, T_N = 81.1 K, and T_N = 66.5 K, respectively.

The chemical bonding analysis is an interesting tool to visualize the bonding interactions in the solids. This is investigated using the crystal orbital Hamilton population (COHP) analysis, which is an energy resolved partitioning technique of the band structure energy in terms of atomic and bonding contribution. Seshadri *et al.* [147, 151] were amongst to recognize the importance of the chemical bonding analysis in the solids. The electronic structure of GdAuMg has been recently

studied within local density approximation (LDA)/LDA+U with a view to understanding the role of partial density of states near the Fermi energy [62]. To understand their chemical bonding peculiarities, the electronic structures of these intermetallic compounds are investigated in detail.

The antiferromagnetic structures were obtained by constructing a hypothetical supercell of GdAuX by doubling lattice parameters in all the three directions. Where Gd atoms lying in one planes are aligned parallel to each others and the next nearest neighbor Gd atoms are aligned in opposite direction. Such arrangements of spin of Gd atoms avoid the possibility of spin frustration state within triangular network of Gd atoms.

7.2 Results and discussion

7.2.1 Density of states

In this section, the density of states (DOS) for three GdAuX (X = Mg, Cd and In) compounds are presented. The DOS of the compounds is displayed in the plots of Figure 7.1 for the different X atoms. The spin-down DOS is not displayed because they are similar to the spin-up DOS. All three materials are metallic. In every one of the three compounds, the DOS exhibits a narrow band composed largely of Gd-f orbitals appeared at approximately -4.3 eV below the Fermi energy (ϵ_F). Gd-d and X-p states contribute at the ϵ_F except for the cadmium compound, whereas nearly Gd-d states are at the ϵ_F. In GdAuMg, Mg-s states are mixed with Au-d states at approximately -5.5 eV. In-s states in GdAuIn are more localized at approximately -7 eV than the Mg-s states because indium has filled s orbitals and the p states are mostly below the ϵ_F. These states are mixed with Au-d states. Au-d states are quite sharply peaked and mostly centered around -5 eV below the ϵ_F. Some of the Au-d states are mixed with the In-s states at -7 eV.

The most obvious difference in the DOS of the two compounds (GdAuMg and GdAuIn) is the presence of filled s orbitals in indium, indicated by a narrow peak at -7 eV below the ϵ_F. Some Mg-s states are found mixed with the Au-d states. There is a slight mixing of Gd-f states with the Au-d states at approximately -4.3 eV. The d states of gold in the magnesium and indium compounds are distinctly broader than those of the cadmium compound. In the magnesium and indium compounds, the d states of the gold atoms trace the s and p states of magnesium and indium. One observes more pure Au-d states in the cadmium compound, whereas the Au-d and Mg-s or In-s states are found at the same energies in the magnesium and indium compounds.

The DOS of GdAuCd is shown in Figure 7.1(b). The Gd-f states are almost localized well below Fermi energy in all three compounds. It is confirmed that there are no Gd-f states at the Fermi energy. In general, LDA calculations underestimate the exchange splitting of the Gd-f states. Including the electron-electron correlation might results in larger splitting between the occupied and

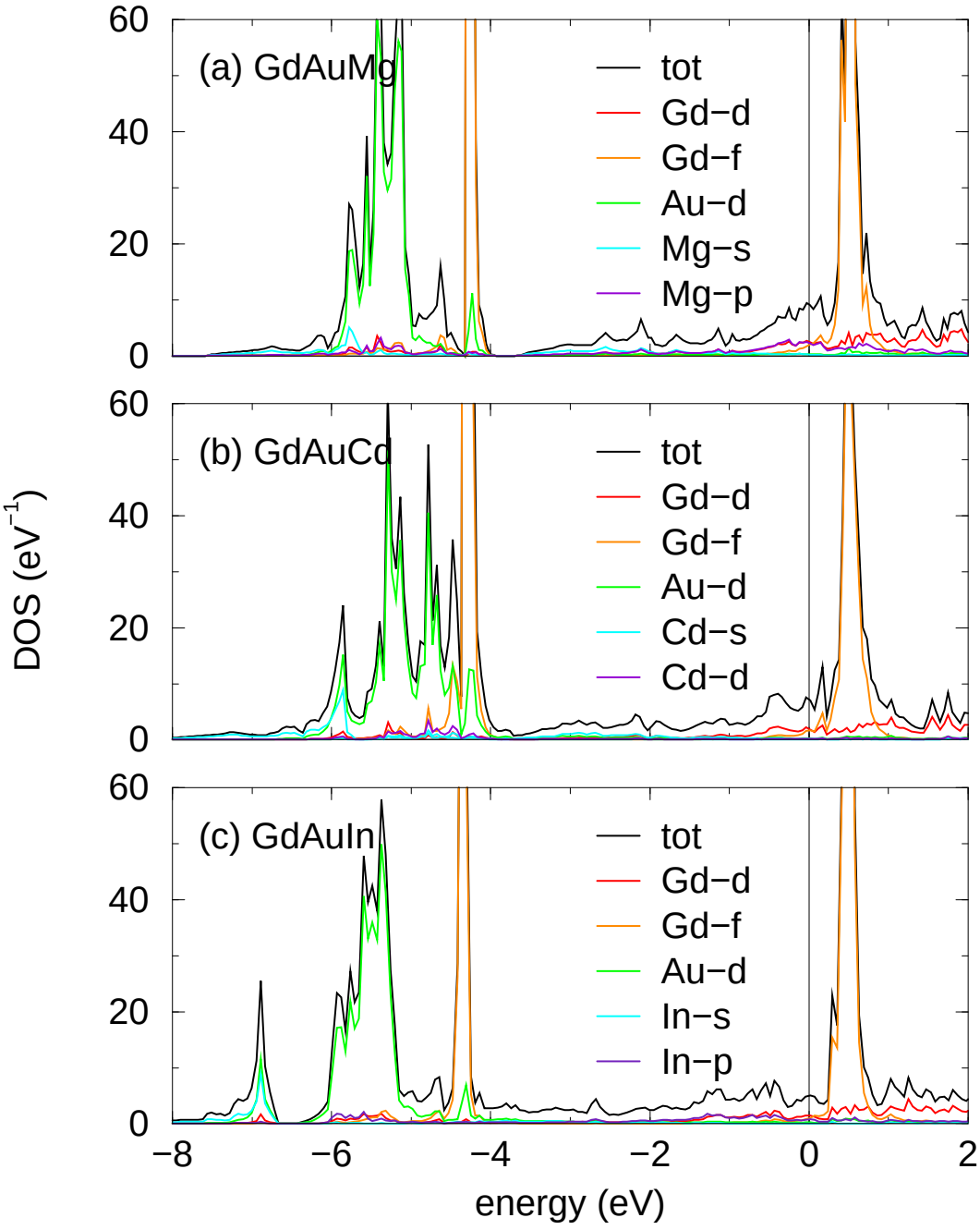

Figure 7.1: LMTO DOS for GdAuX compounds, plotted in spin-up direction only. Note that the spin-down DOS is not shown here because of the similarity with the spin-up DOS. In these and in other plots, the top of the valence band is taken as zero on the energy axis.

unoccupied Gd-f states. However, the states around Fermi energy are not influenced by the Gd-f states [30].

7.2.2 Chemical bonding

In order to show bonding interactions, a recently developed tool in density functional theory was used, the Crystal Orbital Hamiltonian Population (COHP) [48], which can be plotted as a function of the energy and can demarcate different bonding, non-bonding and antibonding contributions for specific pairwise interactions. COHPs are the solid state/DFT equivalent of a Mulliken population analysis and are similar to the Crystal Orbital Overlap Populations (COOPs) developed by Hoffmann and co-workers [76].

For the three compounds, LMTO COHPs for the Au-X interactions were calculated. To avoid unphysical COHP interactions between empty spheres and atoms, all empty sphere orbitals were kept downfolded. All COHPs were then scaled by the number of interactions in the unit cell. The COHPs are spin resolved because GdAuIn, GdAuMg, and GdAuCd are antiferromagnetic. The Au-X COHPs of GdAuX for the different X are displayed in the plots in Figure 7.2. For the convention used, a positive COHP represents bonding interactions while a negative COHP represents antibonding interactions. It was observed that the Au-X interaction is mostly bonding for all three compounds below ϵ_F. Antibonding states are well separated and far away from the ϵ_F. The unoccupied states above the ϵ_F show a small bonding component.

In these compounds, spin-up and spin-down COHPs are filling in the same manner. Mg-s states and Au-d states in GdAuMg occupy the same energy range, suggesting a significant Au-Mg covalency (confirmed by the DOS calculations). The situation is the same in GdAuIn, where only In-p states bond with Au-d states, indicating covalency between indium and gold states. The spin-up and spin-down bands are largely filled. Changes in the extent of Au-X covalency in GdAuMg and GdAuIn can be better seen by examining the COHPs. In every case, there is a bonding interaction below the Fermi energy. The high bonding interactions at approximately -7 eV are mainly due to the In-s states in GdAuIn. The bonding interaction at approximately -6 eV in GdAuCd is seen to be mainly due to the Cd-s states; in GdAuMg there is no separate bonding due to the Mg-s states. These states are mixed with the Au-d states and form bonding interactions over the entire energy range. The extra electrons in the In-p orbital enhance the extent of the favourable bonding hybridization in GdAuIn by pushing down the s electron pair from the Fermi energy and making it more localized. The Au-In COHP is more disperse in GdAuIn indicating Au-In hybridization over a broader energy range. In particular, the COHP strength in the region of the In-s states is increased significantly. In GdAuMg, the COHPs between gadolinium and magnesium are much weaker as a result of the longer Gd-Mg distances. The extents of such interactions are small but noticeable in the

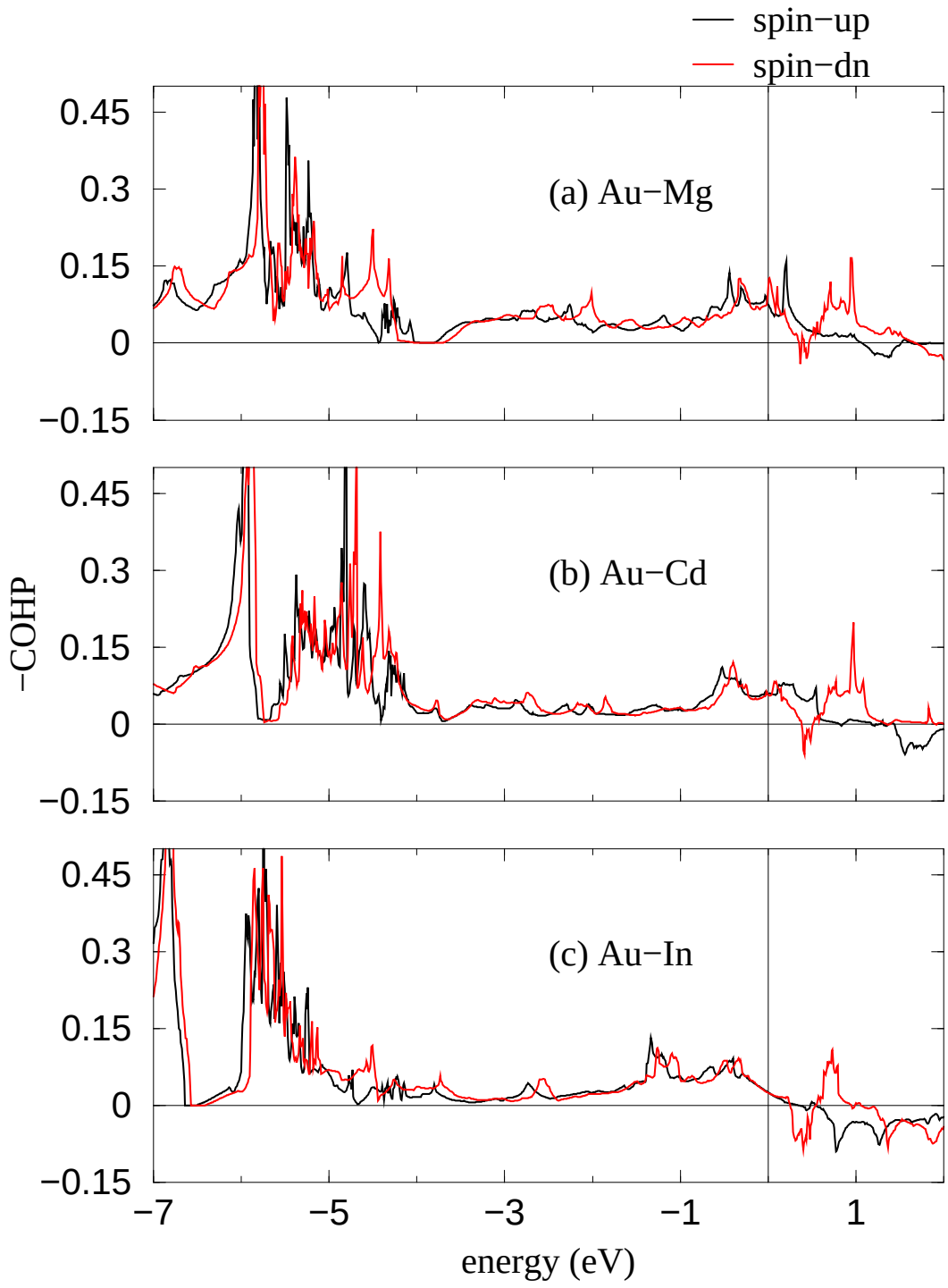

Figure 7.2: Crystal Orbital Hamiltonian Populations (COHPs) for the Au-X interactions in GdAuX (X = Mg, Cd and In).

Table 7.1: Total energies (in eV) for the ferromagnetic (FM) and antiferromagnetic (AFM) structures of GdAuX (X = Mg, Cd, and In)

Compounds	energy (FM)	energy (AFM)
GdAuMg	-2486151.40	-2486151.50
GdAuCd	-2926034.68	-2926034.67
GdAuIn	-2949447.86	-2949447.82

magnesium and indium compounds. In the region at approximately -5 eV (referenced to the top of the valence band), the Au-X interaction is primarily a bonding interaction for all three compounds.

The gold and X atoms together build up rigid three-dimensional $[AuX]$ networks in which the gadolinium atoms fill distorted hexagonal channels. The Au-In (282-290 pm), Au-Mg (278-291 pm) and Au-Cd (280-290 pm) distances compare well with the sums of the covalent single bond radii of 283 pm (Au + In), 270 pm (Au + Mg), and 275 pm (Au + Cd) [50]. For GdAuIn, the shorter Au-In distances match perfectly with the sum of the radii, while they are slightly longer for GdAuMg and GdAuCd. From this comparison we can assume that there are slightly stronger Au-In interactions in GdAuIn than in GdAuMg and GdAuCd which is verified by the calculations.

7.2.3 Electron localization function (ELF)

The electron localization function (ELF) [152] is a real space indicator of the extent to which electrons are localized, and display a strong Pauli repulsion. The ELF therefore serves to locate bonding and non-bonding electron pairs in the real space of the crystal structure.

The valence electron localization function (ELF) for ferromagnetic GdAuMg, GdAuCd, and GdAuIn are displayed in Figure 7.3. Figures 7.3(a), (b), and (c) show isosurfaces of the electron localization function (the ELF scale as used here goes from 0 to 1) for values of 0.61, 0.42, and 0.62 respectively. A high value of localization indicates a covalent bonding between gold (cyan) and magnesium (blue) in GdAuMg and as well as between gold (cyan) and indium (blue) in GdAuIn.

For GdAuMg the localization domain is closer to magnesium than it is to gold. As also seen from the map of the ELF projected at the rear of the unit cells, there is also a stronger localization of s states closer to the indium than to the gold in GdAuIn. It should be noted that magnesium does not behave in an ionic manner, but effectively in a covalent manner. When localization behavior around magnesium in GdAuMg is compared with that of indium in GdAuIn, it was found that the indium compound has In-s electrons that are more localized than Mg-s. Both compounds behave covalently compared to GdAuCd, localization behavior in the indium compound is well pronounced as compared to GdAuMg as can also be seen from the map of the projected ELF.

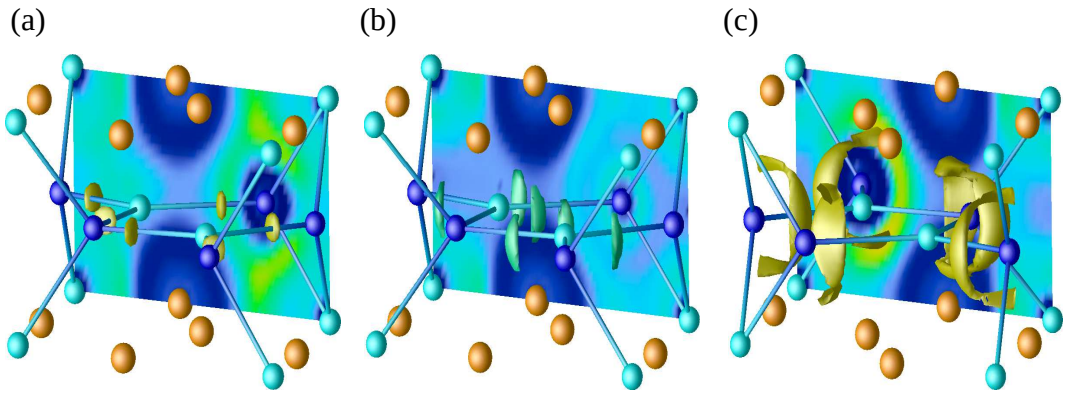

Figure 7.3: For the three compounds GdAuMg, GdAuCd, and GdAuIn, (a), (b), and (c) are valence electron localization isosurfaces for ELF values of 0.61, 0.42, and 0.62, respectively.

7.2.4 Magnetic behavior

The total energies for ferromagnetic and the antiferromagnetic GdAuX are presented in Table 7.1. The differences in the energies are marginal, and the most stable arrangement appears to be the antiferromagnetic structure for GdAuMg. The other two compounds GdAuCd and GdAuIn have almost the same energies for both magnetic structures. When compared to the other compounds, it is to be noted that GdAuMg clearly exhibits antiferromagnetic behavior and this explains why it has a higher Neel temperature than the other compounds.

7.3 Summary

In GdAuMg and GdAuIn, the Au-d bands are found broader than those observed in the corresponding cadmium compound. However, the valence band states in the magnesium and indium compounds have a strong Au-d admixture. In the case of the cadmium compound, states below the top of the valence band have a more pure Au-d character.

Chapter 8

Verwey-type transition in EuNiP

8.1 Introduction

In the past few years, studies on rare earth based ternary intermetallic compounds have revealed that these systems exhibit a variety of unusual magnetic, electric and structural related properties. This Chapter focused on studies of EuNiP, which according to earlier experimental results [117] reveals interesting effects related to structural phase transitions. In most of the Eu containing compounds, the Eu ion can be divalent or trivalent. In homogeneous mixed-valent Eu compounds, itinerant electrons fluctuate dynamically between the $4f^6$ and the $4f^7$ states with the charge on Eu sites being noninteger. In inhomogeneous mixed-valent compounds, the valence of Eu ions depends strongly on temperature. Above the Verwey transition, all Eu ions are crystallographically equivalent. Below the transition, however, they are characterized by charge ordering with di- and trivalent Eu ions occupying distinct lattice sites. Such a behavior is seen in Eu_3S_4 [13, 16, 22, 66, 114, 120, 142, 150], Eu_4As_3 [174], $EuBr_x$ [109], $EuPd_3B$ [35, 45, 166] and $EuPd_3Si_{0.25}$ [44].

The structures and properties of the ternary mixed-valent metallic compounds EuPtP, EuPdP and EuNiP are reported in references [55, 77, 88, 89, 116, 117]. The crystal structure of EuNiP as well as of EuPdP at room temperature belongs to the $P\overline{3}m1$ space group [117]. In these compounds, two inequivalent Eu atoms reside on planes well separated by layers composed of Pd and P atoms. There are two structural phase transitions in EuNiP [117]. The first order transition at 95 K is accompanied by temperature hysteresis, whereas the high temperature structural transformation at about 510 K is continuous and smeared over 100 K. Despite the absence of hysteresis, a small latent heat value of about 259 J/mole was registered. The high temperature transition associated with a change of crystal symmetry, $P\overline{3}m1$ (phase γ) - $P6_3/mmc$ (phase β), is accompanied by continuous changes of the lattice parameters and enhanced thermal volume expansion, causing a

volume increase of about 0.85 % in the temperature range between 370 K and 620 K [89]. The average valence of Eu in EuNiP that is found from magnetic susceptibility measurements is 2.33 at T = 510 K and 2.5 at room temperature [117].

Different valence states of Eu are easy to distinguish by means of ^{151}Eu Mössbauer spectroscopy. In inhomogeneous mixed-valent (charge-ordered) systems, two separate Eu sites are observed. Trivalent Eu ions show isomer shifts near zero velocity, while divalent Eu atoms have shifts in the range between -15 mms^{-1} and -12 mms^{-1} [67]. In systems displaying homogeneous mixed valence, the Mössbauer spectra display a single line, which is located in between. Above the Verwey transition temperature, the two lines transform to a single line if the charge fluctuations are faster than the characteristic observation time of the Mössbauer experiment. Mössbauer room temperature data indicating Eu^{3+} and Eu^{2+} states lead the authors [117] to conclude that EuNiP and EuPdP are the compounds with static mixing valence. However, a high density of $4f$ states close to the Fermi level, observed in photoemission experiments as well as in the calculations for EuPdP [55], is very similar to that have found for inhomogeneous mixed-valent metallic $EuPd_3B$ and semiconducting Eu_3S_4 with Verwey transition [54].

In this Chapter, based on the earlier results of photoemission measurements and the observation of saddle points near ϵ_F in the calculated f-electrons density of states, the inhomogeneous mixed valency is predicted in compounds analogous to EuNiP [55]. In the course of Mössbauer studies of EuNiP charge ordering below and valence fluctuations above a possible Verwey-type transformation was found [100].

8.2 Results and Discussion

In order to understand the valence of Eu in the compounds that were studied, it is necessary to consider their density of states (DOS) and in particular, the transition metal d states.

The total DOS for the spin polarized band structure calculations of EuAuAs, EuPdP and EuNiP is shown in Figure 8.1. The $4f$ majority band of EuAuAs (Figure 8.1(a) is situated slightly below ϵ_F, and no $4f$ peak in the DOS at ϵ_F is found that would indicate divalent Eu compounds. The dominant contributions to the DOS at ϵ_F originate from the Eu d electrons. In all divalent Eu compounds of this structure type, the transition metal d states, which in this case are the Au d states, are far below ϵ_F between -6.5 and -4 eV. Compared with other intermetallic compounds, the Au states are exceptionally low in energy, even lower than the anionic As p states between -4.5 and -0.5 eV.

In contrast to EuAuAs, the $4f$ majority states of EuPdP in Figure 8.1(b) are found in the vicinity of the Fermi energy (ϵ_F). A DOS peak is situated just at ϵ_F. The character of these electrons is $4f$, which is in agreement with photoemission results [55]. Pd d states are found between -4.5

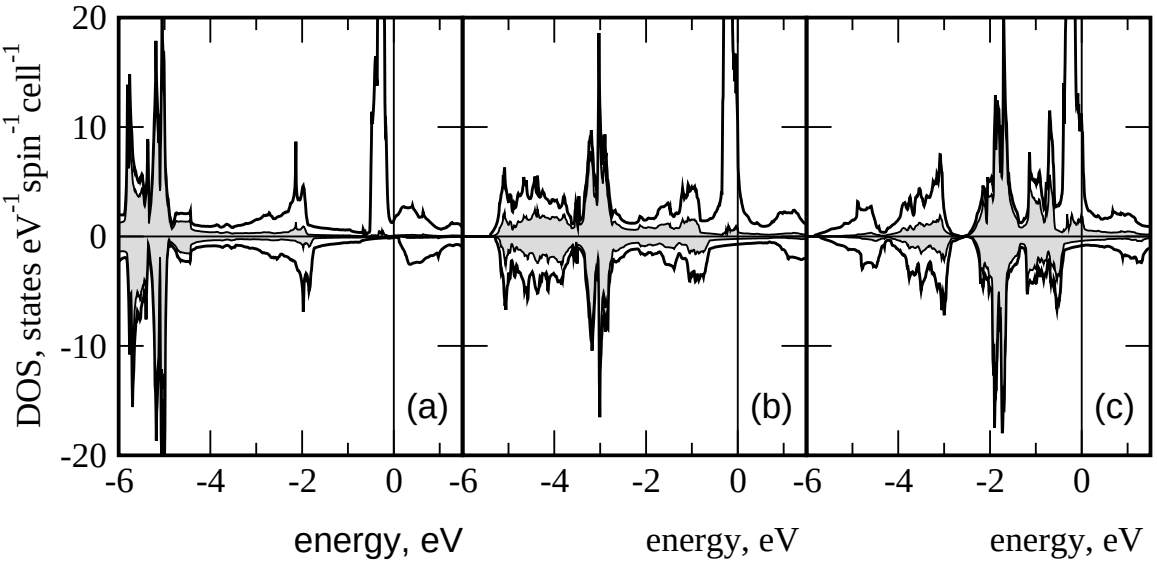

Figure 8.1: LMTO density of states for: (a) EuAuAs (b) EuPdP and (c) EuNiP plotted separately for the two spin directions. The projected density of (a) Au-5d (b) Pd-4d and (c) Ni-3d contributions are shown by shaded areas. The origin on the energy axis is the top of the valence band.

and -0.5 eV. The transition metal states are found at significantly higher energies in this noninteger valent Eu compound, whereas p states build the bottom of the valence band between -4.7 and -3 eV. In case of EuNiP, Ni d states even cross ϵ_F, Figure 8.1(c). Also in this compound, p states are situated below transition metal d states. This inversion between transition metal d and anionic p states seems to be a necessary condition for noninteger valent Eu. The highest Eu valence at room temperature is observed in EuNiP, the compound with the highest transition metal DOS of d-electrons at ϵ_F. A second necessary condition seems to be a peak of Eu $4f$ states at ϵ_F. This peak has its origin in a saddle point in the band structure, a van Hove singularity about 0.5 eV below ϵ_F [54]. A second van Hove singularity in EuNiP is built close to the ϵ_F by hybridization of $4f$ electrons with the conduction band level.

Eventually, taking into account the Mössbauer measurements, one can conclude the existence of inhomogeneous mixed-valent behavior in EuNiP, which is associated with a high density of $4f$ states close to the Fermi energy [100].

8.3 Summary

The inhomogeneous mixed valency of Eu in EuNiP follows from band structure calculations that demonstrates a high density of $4f$ states close to the ϵ_F. There is now growing evidence that this high density of states near ϵ_F could be a signature of inhomogeneous mixed valency. The van

Hove singularity is another significant feature that is associated with a large density of $4f$ states in the proximity of the ϵ_F. Large electron-phonon coupling associated with the saddle point could be responsible for the structural instability in inhomogeneous mixed-valent Eu compounds analogous to EuNiP.

Bibliography

[1] R. L. Abdon and T. Hughbanks. *J. Am. Chem. Soc.*, **117**:10035, 1995.

[2] D. T. Adroja, S. K. Malik, S. N. Padalia, R. Walia, and Vijayaraghavan. *Phys. Rev. B*, **42**:2700, 1990.

[3] V. I. Anisimov, F. Aryasetiawan, and A. I. Lichtenstein. *J. Phys. Condens. Matter*, **9**:767, 1997.

[4] V. N. Antonov, H. A. Dürr, Y. Kucherenko, L. V. Bekenov, and A. N. Yaresko. *Phys. Rev. B*, **72**:054441, 2005.

[5] V. N. Antonov, B. N. Harmon, L. V. Bekenov, A. P. Shpak, and A. N. Yaresko. *Phys. Rev. B*, **71**:174428, 2005.

[6] M. S. Augsburger, M. C. Viola, J. C. Pedregosa, A. Mu noz, J. A. Alonso, and R. E. Carbonio. *J. Mater. Chem.*, **15**:993, 2005.

[7] S. Baran, J. Ivanov, J. Leciejewicz, M. Slaski, A. Szytula, and A. Zygmunt. *J. Phys. Condens. Matter*, 9:9053, 1997.

[8] S. Baran, J. Ivanov, J. Leciejewicz, N. Stüsser, A. Szytula, A. Zygmunt, and Y. Ding. *J. Alloys Compds.*, 257:3, 1997.

[9] S. Baran, J. Leciejewicz, P. Hofmann, and A. Szytula. *J. Alloys Compds.*, **275**:541, 1998.

[10] S. Baran, J. Leciejewicz, M. Stüsser, A. Szytula, and Z. Tomkowicz. *Solid State Commun.*, **101**:631, 1997.

[11] S. Baran, J. Leciejewicz, M. Stüsser, A. Szytula, A. Zygmunt, and V. Ivanov. *J. Phys. Condens. Matter*, **8**:8397, 1996.

[12] U. V. Barth and L. Hedin. *J. Phys. C: Solid State Phys.*, **5**:1629, 1972.

[13] B. Batlogg, E. Kaldis, and P. Wachter. *J. Magn. Magn. Mater.*, **3**:96, 1976.

[14] A. D. Becke and K. E. Edgecombe. *J. Chem. Phys.*, **92**:5397, 1990.

[15] J. F. Bérar and G. Baldinozzi. *IUCr CPD Newsletter*, **20**:3, 1998.

[16] O. Berkooz, M. Malamud, and S. Shtrikman. *Solid State Commun.*, **6**:185, 1968.

[17] M. Bibes, L Balcells, S. Valencia, J. Fontcuberta, M. Wojcik, E. Jedryka, and S. Nadolski. *Phys. Rev. Lett.*, **87**:067210, 2001.

[18] P. Blaha, K. Schwarz, G. K. H. Madsen, D. Kvasnicka, and J. Luitz. Karlheinz Schwarz, Techn. Universität Wien, Wien, Austria, 2001.

[19] T. Block, M. J. Carey, B. A. Gurney, and O. Jepsen. *Phys. Rev. B*, **70**:205114, 2004.

[20] C. N. Borca, T. Komesu, H.-K. Jeong, P. A. Dowben, D. Ristoiu, Ch. Hordequin, J. P. Nozieres, J. Pierre, S. Stadler, and Y. U. Idzerda. *Phys. Rev. B*, **64**:052409, 2001.

[21] L. Brewer and P. R. Wengert. *Metall. Trans.*, **4**:83, 1973.

[22] P. Brix, S. Hüfner, P. Kienle, and D. Quitmann. *Phys. Lett.*, **13**:140, 1964.

[23] P. J. Brown, K. U. Neumann, P. J. Webster, and K. R. A. Ziebeck. *J. Phys. Condens. Matter*, **12**:1827, 2000.

[24] E. Brück, O. Tegus, L. Zhang, X. W. Li, F. R. de Boer, and K. H. J. Buschow. *J. Alloys Compds.*, **383**:32, 2004.

[25] K. H. J. Buschow and P.G. van Engen. *J. Magn. Magn. Mater.*, **25**:90, 1981.

[26] M. J. Calhorda and R. Hoffmann. *Inorg. Chem.*, **27**:4679, 1988.

[27] F. Canepa and S. Cirafici. *J. Alloys Compds.*, **232**:71, 1996.

[28] L. A. Carapella and R. R. Hultgren. *Phys. Rev.*, **59**:905, 1941.

[29] A. W. Carbonari, R. N. Saxena, Jr. W. Pendl, J. Mestnik Filho, R. N. Attili, M. Olzon-Dionysio, and S. D. de Souza. *J. Magn. Magn. Mater.*, **163**:313, 1996.

[30] F. Casper, Hem C. Kandpal, and Claudia Felser. *submitted*, 2006.

[31] F. Casper, V. Ksenofontov, H. C. kandpal, S. reiman, T. Shishido, M. Takahashi, M. Takeda, and C. Felser. *Z. Anor. Allg. Chemie*, 632:1273, 2006.

[32] D. M. Ceperley and B. J. Alder. *Phys. Rev. Lett.*, **45**:566, 1980.

[33] L. Chioncel, M. I. Katsnelson, R. A. de Groot, and A. I. Lichtenstein. *Phys. Rev. B*, **68**:144425, 2003.

[34] N. E. Christenson. *Phys. Rev. B*, **32**:6490, 1985.

[35] L. Cianchi, S. de Gennaro, F. Gulisano, M. Mancini, and G. Spina. *Hyperfine Interact.*, **56**:1437, 1989.

[36] S. Cirafici, Palenzona, and Canepa. *J. Less-Common Met.*, **107**:179, 1985.

[37] J. M. D. Coey and M. Venkatesan. *J. Appl. Phys.*, **91 (10)**:8345, 2002.

[38] J. M. D. Coey, M. Venkatesan, and M. A. Bari. volume **595**. Springer-Verlag, Heidelberg, 2002.

[39] J. M. D. Coey, M. Viret, and S. v. Molnàr. *Adv. Phys.*, **48**:167, 1999.

[40] R. D. Cowan. University of California Press, Berkeley and Los Angeles, 1981.

[41] R. A. de Groot, F. M. Müller, P. G. van Engen, and K. H. J. Buschow. *Phys. Rev. Lett.*, **50**:2024, 1983.

[42] G. A. de Wijs and R. A. de Groot. *Phys. Rev. B*, **64**:020402, 2001.

[43] S. K. Dhar, N. Nabudripad, and R. Vijayaraghavan. *J. Phys. F: Met. Phys.*, **18**:L41, 1988.

[44] S. K. Dhar, R. Nagarajan, S. K. Malik, D. Rambabu, and R. Vijayaraghavan. *J. Magn. Magn. Mater.*, **31**:393, 1983.

[45] S. K. Dhar, R. Nagarajan, S. K. Malik, R. Vijayaraghavan, M. M. Abd-Elmeguid, and H. Micklitz. *Phys. Rev. B*, **29**:5953, 1984.

[46] X. Y. Dong, C. Adelmann, J. Q. Xie, C. J. Palmstrom, X. Lou, J. Strand, P. A. Crowell, J.-P. Barnes, and A. K. Petford-Long. *Appl. Phys. Lett.*, **86**:102107, 2005.

[47] P. A. Dowben and R. Skomski. *J. Appl. Phys.*, **95**:7453, 2004.

[48] R. Dronskowski and P. E. Blöchl. *J. Phys. Chem.*, **97**:8617, 1993.

[49] H. Ebert. *The Munich SPR-KKR package, Version 3.6 , http://olymp.cup.uni-muenchen.de/ak/ebert/SPRKKR.* 2005.

[50] J. Emsley. *The Elements.* Clarendon Press Oxford, 1989.

[51] P. G. van Engen, K. H. J. Buschow, and M. Erman. *J. Magn. Magn. Mater.*, **30**:374, 1983.

[52] G. H. Fecher, Hem C. Kandpal, S. Wurmehl, C. Felser, and G. Schönhense. *J. Appl. Phys.*, **99**:08J106, 2006.

[53] G. H. Fecher, Hem C. Kandpal, S. Wurmehl, J. Morais, H.-J. Lin, H.-J. Elmers, G. Schönhense, and C. Felser. *J. Phys. Condens. Matter*, **17(46)**:7237, 2005.

[54] C. Felser. *J. Alloys Compds.*, **262-263**:87, 1997.

[55] C. Felser, S. Cramm, D. Johrendt, A. Mewis, O. Jepsen, G. Hohlneicher, W. Eberhardt, and O. K. Andersen. *Europhys. Lett.*, **40**:85, 1997.

[56] C. Felser, R. Seshadri, A. Leist, and W. Tremel. *J. Mater. Chem.*, 8:787, 1998.

[57] A. G. Froseth, R. Hoier, P. M. Derlet, S. J. Andersen, and C. D. Marioara. *Phys. Rev. B*, **67**:224106, 2003.

[58] H. Fuji, Y. Uwatoko, M. Akayama, K. Satoh, Y. Maeno, T. Fujita, J. Sakurai, H. Kanimura, and T. Okamoto. *Jpn. J. appl. Phys. (Suppl.)*, **26**:549, 1987.

[59] S. Fuji, S. Sugimura, S. Ishida, and S. Asano. *J. Phys. Condens. Matter*, **2**:8583, 1990.

[60] Peter Fulde. Springer-Verlag, Heidelberg, 1995.

[61] I. Galanakis, P. H. Dederichs, and N. Papanikolaou. *Phys. Rev. B*, **66**:174429, 2002.

[62] J. Gegner, T. C. Koethe, H. Wu, Z. Hu, H. Hartmann, T. Lorenz, T. Fickenscher, R. Pöttgen, and L. H. Tjeng. *Phys. Rev. B*, **74**:073102, 2006.

[63] U. Geiersbach, A. Bergmann, and K. Westerholt. *J. Magn. Magn. Mater.*, **240**:546, 2002.

[64] U. Geiersbach, A. Bergmann, and K. Westerholt. *Thin Solid Films*, **425**:225, 2003.

[65] E. I. Gladyshevskii. *Spvirt Powder Metallurgy and Metal Ceramics, Translated from Poroshkovaya Metallurgiya, Kiev*, **1**:262, 1962.

[66] E. Görlich, H. U. Hrynkiewics, R. Kmiec, K. Latka, and K. Tomala. *Phys. Status Solidi B*, **64**:174, 1974.

[67] N. N. Greenwood and T. C. Gibb. *Mössbauer Spectroscopy.* Chapman and Hall Ltd. London, 1971.

[68] S. J. Hashemifar, P. Kratzer, and M. Scheffler. *Phys. Rev. Lett.*, **94**:096402, 2005.

[69] L. Hedin and B. I. Lundquist. *J. Phys. C: Solid State Phys.*, **4**:2064, 1971.

[70] Fr. Heusler. *Verh. d. DPG*, **5**:219, 1903.

[71] M. C. Hickey, A. Husmann, S. N. Holmes, and G. A. C.Jones. *J. Phys. Condens. Matter*, **18**:2897, 2006.

[72] R. D. Hoffmann and R. Pöttgen. *Z. Kristallogr.*, **216**:127, 2001.

[73] P. Hohenberg and W. Kohn. *Phys. Rev.*, **136**:B864, 1964.

[74] C. Hordequin, D. Ristoiu, L. Rannoa, and J. Pierre. *Eur. Phys. J. B*, **16**:287, 2000.

[75] Ch. Hordequin, J. Pierre, and R. Currat. *Physica B*, **234-236**:605, 1997.

[76] T. Hughbanks and R. Hoffmann. *J. Am. Chem. Soc.*, **105**:3528, 1983.

[77] C. Huhnt, G. Michels, W. Schlabitz, D. Johrendt, and A. Mewis. *J. Phys. Condens. Matter*, **9**:9953, 1997.

[78] A. Hütten, S. Kämmerer, J. Schmalhorst, and A. Thomas. *phys. stat. sol.(a)*, **201**:3271, 2004.

[79] K. Inomata, S. Okamura, and N. Tezuka. *J. Magn. Magn. Mat.*, **282**:269, 2004.

[80] S. Ishida, S. Akazawa, Y. Kubo, and J. Ishida. *J. Phys. F: Met. Phys.*, **12**:1111, 1982.

[81] S. Ishida, S. Fujii, S. Kashiwagi, and S. Asano. *J. Phys. Soc. Jap.*, **64**:2152, 1995.

[82] S. Ishida, S. Kashiwagi, S. Fujii, and S. Asano. *Physica B*, **210**:140, 1995.

[83] S. Ishida, T. Masakai, S. Fujii, and S. Asano. *Physica B*, **245**:1, 1998.

[84] S. J. Jenkins and D. A. King. *Surf. Sci. Lett.*, **501**:L185, 2002.

[85] O. Jepsen and O. K. Andersen. MPI für Festkörperforschung, Stuttgart, Germany, 2000.

[86] M. H. Jo, N. D. Mathur, N. K. Todd, and M. G. Blamire. *Phys. Rev. B*, **61**:14905, 2000.

[87] S. Jobic, R. brec, and J. Rouxel. *J. Alloys Compds.*, **178**:253, 1992.

[88] D. Johrendt, C. Felser, C. Huhnt, G. Michels, W. Schäfer, and A. Mewis. *J. Alloys Compds.*, **246**:21, 1997.

[89] D. Johrendt and A. Mewis. *Z. Naturforsch. B: Chem. Sci.*, **45**:1262, 1990.

[90] K. A. Gschneidner Jr. and V. K. Pecharsky. *Annu. Rev. Mater. Sci.*, **30**:387, 2000.

[91] K. A. Gschneidner Jr., V. K. Pecharsky, and A. O. Tsokol. *Rep. Prog. Phys.*, **68**:1479, 2005.

[92] R. J. Soulen Jr., J. M. Byers, M. S. Osofsky, B. Nadgorny, T. Ambrose, S. F. Cheng, P. R. Broussard, C. T. Tanaka, J. Nowak, J. S. Moodera, A. Barry, and J. M. D. Coey. *Science*, **282**:85, 1998.

[93] D. Jung, H.-J. Koo, and M.-H. Whangbo. *J. Mol. Struct. Theochem*, **527**:113, 2000.

[94] S. Kämmerer, S. Heitmann, D. Meyners, D. Sudfeld, A. Thomas, A. Hütten, and G. Reiss. *J. Appl. Phys.*, **93**:7945, 2003.

[95] S. Kämmerer, A. Thomas, A. Hütten, and G. Reiss. *Appl. Phys. Lett.*, **85**:79, 2004.

[96] Hem C. Kandpal, G. H. Fecher, C. Felser, and G. Schönhense. *Phys. Rev. B*, **73**:094422, 2006.

[97] I. Karla, J. Pierre, and B. Ouladdiaf. *Physica*, **253**:215, 1998.

[98] K.-I. Kobayashi, T. Kimura, H. Sawada, K. Terakura, and Y. Tokura. *Nature*, **395**:677, 1998.

[99] W. Kohn and L. J. Sham. *Phys. Rev.*, **140**:A1133, 1965.

[100] V. Ksenofontov, Hem C. Kandpal, J. Ensling, M. Waldeck, D. Johrendt, A. Mewis, P. Gütlich, and C. Felser. *Europhys. Lett.*, **74(4)**:672, 2006.

[101] J. Kübler. *Physica*, **127B**:257, 1984.

[102] J. Kübler, A. R. Williams, and C. B. Sommers. *Phys. Rev. B*, **28**:1745, 1983.

[103] T. Y. Kuramoto, S. M. Kauzlarich, and D. J. Webb. *Chem. Mater.*, **4**:435, 1992.

[104] K. Kuriyama, K. Nagasawa, and K. Kushida. *J. Cryst. Growth*, **237**:2019, 2002.

[105] K. Łatka, R. Kmiec, A. W. Pacyna, T. Fickenscher, R. D. Hoffmann, and R. Pöttgen. *Soild State Sci.*, **6**:301, 2004.

[106] K. Łatka, R. Kmiec, A. W. Pacyna, T. Fickenscher, R. D. Hoffmann, and R. Pöttgen. *J. Magn. Magn. Mater.*, **280**:90, 2004.

[107] S. C. Lee, T. D. Lee, P. Blaha, and K. Schwarz. *J. Appl. Phys.*, **97**:10C307, 2005.

[108] M. Levy. *Proc. Natl. Acad. Sci.*, **76**:6062, 1979.

[109] S. J. Lyle and W. A. Westall. *J. Less-Common Met.*, **106**:109, 1984.

[110] S. Majumdar, M. K. Chattopadhyay, V. K. Sharma, K. J. S. Sokhey, S. B. Roy, and P. Chaddah. *Phys. Rev. B*, **72**:012417, 2005.

[111] S. K. Malik, H. Takeya, and K. A. Gschneider Jr. *Phys. Rev. B*, **48**:9858, 1993.

[112] A. P. Malozemoff, A. R. Williams, and V. L. Moruzzi. *Phys. Rev. B*, **29**:1620, 1984.

[113] T. Marukame, T. Kasahara, K.-I. Matsuda, T. Uemura, and M. Yamamoto. *Jpn. J. Appl. Phys.*, **44**:L521, 2005.

[114] O. Massenet, J. M. D. Coey, and F. Holtzberg. *J. Phys. C*, **4**:297, 1976.

[115] Ph. Mavropoulos, K. Sato, R. Zeller, P. H. Dederichs, V. Popescu, and H. Ebert. *Phys. Rev. B*, **69**:054424, 2004.

[116] G. Michels, C. Huhnt, W. Scharbrodt, E. Holland-Moritz, D. Johrendt, A. Mewis, and W. Schlabitz. *Physica B*, **199-200**:612, 1994.

[117] G. Michels, C. Huhnt, W. Scharbrodt, W. Schlabitz, E. Holland-Moritz, M. M. Abd-Elmeguid, H. Micklitz, D. Johrendt, V. Keimes, and A. Mewis. *Z. Phys. B: Condens. Matter.*, **98**:75, 1995.

[118] Y. Miura, K. Nagao, and M. Shirai. *Phys. Rev. B*, **69**:144413, 2004.

[119] P. Mohn, P. Blaha, and K. Schwarz. *J. Magn. Magn. Mater.*, **140-144**:183, 1995.

[120] I. Mörke, G. Travaglini, and P. Wachter. *Valence Instabilities.* North-Holland, Amsterdam, 1982.

[121] S. Nadolski, M. Wojcik, E. Jedryka, and K. Nesteruk. *J. Magn. Magn. Mater.*, **140-144**:2187, 1995.

[122] B. R. K. Nanda and I. Dasgupta. *J. Phys. Condens. Matter*, **15**:7307, 2003.

[123] V. Niculescu, T. J. Burch, K. Rai, and J. I. Budnick. *J. Magn. Magn. Mater.*, **5**:60, 1977.

[124] S. Öğüt and K. M. Rabe. *Phys. Rev. B*, **51**:10443, 1995.

[125] R. G. Parr and W. Yang. *Density Functional Theory of Atoms and Molecules.* Oxford University Press, 1989.

[126] L. Pauling. *Phys. Rev.*, **54**:899, 1938.

[127] V. K. Pecharsky and K. A. Gschneidner Jr. *Appl. Phys. Lett.*, **70**:3299, 1997.

[128] V. K. Pecharsky and K. A. Gschneidner Jr. *Adv. Cryog. Eng.*, **43**:1729, 1998.

[129] J. P. Perdew, K. Burke, and M. Ernzerhof. *Phys. Rev. Lett.*, **77**:3865, 1996.

[130] J. P. Perdew, K. Burke, and M. Ernzerhof. *Phys. Rev. Lett.*, **78**:1396, 1997.

[131] J. P. Perdew, J. A. Chevary, S. H. Vosko, K. A. Jackson, M. R. Pederson, D. J. Singh, and C. Fiolhais. *Phys. Rev. B*, **46**:6671, 1992.

[132] J. P. Perdew and W. Yue. *Phys. Rev. B*, **33**:8800, 1986.

[133] J. P. Perdew and A. Zunger. *Phys. Rev. B*, **23**:5048, 1981.

[134] J. C. Phillips and J. A. van Vechten. *Phys. Rev. B*, **2**:2147, 1970.

[135] W. E. Pickett and D. J. Singh. *Phys. Rev. B*, **53**:1146, 1996.

[136] S. Picozzi, A. Continenza, and A. J. Freeman. *Phys. Rev. B*, **66**:094421, 2002.

[137] S. Picozzi, A. Continenza, and A. J. Freeman. *Phys. Rev. B*, **69**:094423, 2004.

[138] S. Picozzi, A. Continenza, and A. J. Freeman. *J. Magn. Magn. Mat.*, **272-276**:315, 2004.

[139] J. Pierre, I. Karla, and K. Kaczmarska. *Physica B*, **259-261**:845, 1999.

[140] J. Pierre, R. V. Skolozdra, and Y. V. Stadnyk. *J. Magn. Magn. Mater.*, **128**:93, 1993.

[141] J. Pierre, R. V. Skolozdra, J. Tobola, S. Kaprzyk, C. Hordequin, M. A. Kouacou, I. Karla, R. Currat, and E. Leliévre-Berna. *J. Alloys Compds.*, **262-263**:101, 1997.

[142] R. Pott, G. Güntherodt, W. Wichelhaus, M. Ohl, and H. Bach. *Valence Instabilities*. North-Holland, Amsterdam, 1982.

[143] R. Pöttgen and D. Johrendt. *Chem. Mater.*, **12**:875, 2000.

[144] R. Pöttgen, G. Kotzyba, E. A. Görlich, K. Łatka, and R. Dronskowski. *J. Solid State Chem.*, **141**:352, 1998.

[145] M. P. Raphael, B. Ravel, Q. Huang, M. A. Willard, S. F. Cheng, B. N. Das, R. M. Stroud, K. M. Bussmann, J. H. Claassen, and V. G. Harris. *Phys. Rev. B*, **66**:104429, 2002.

[146] M. P. Raphael, B. Ravel, M. A. Willard, S. F. Cheng, B. N. Das, R. M. Stroud, K. M. Bussmann, J. H . Claassen, and V. G. Harris. *Appl. Phys. Lett.*, **79**:4396, 2001.

[147] J. M. Raulot, G. Baldinozzi, R. Seshadri, and P. Cortona. *Solid State Sci.*, **4**:467, 2002.

[148] A. Rehr, T. Y Kuramoto, S. M. Kauzlarich, J. Del Castillo, and D. J. Webb. *Chem. Mater.*, **6**:93, 1994.

[149] L. Ritchie, G. Xiao, Y. Ji, T. Y. Chen, C. L. Chien, M. Zhang, J. Chen, Z. Liu, G. Wu, and X. X. Zhang. *Phys. Rev. B*, **68**:104330, 2003.

[150] J. Röhler and G. Kaindl. *Solid State Commun.*, **36**:1055, 1980.

[151] R. Seshadri and N. A. Hill. *Chem. Mater.*, **13**:2892, 2001.

[152] B. Silvi and A. Savin. *Nature*, **371**:683, 1994.

[153] David J. Singh. Kluwer Academic Publishers, Norwell, Massachusetts 02061 USA, 1994.

[154] L. J. Singh, Z. H. Barber, Y. Miyoshi, Y. Bugoslavsky, W. R. Branford, and L. F. Cohen. *Appl. Phys. Lett.*, **84**:2367, 2004.

[155] Hans L. Skriver. Springer-Verlag, Heidelberg, Germany, 1984.

[156] J. C. Slater. *Phys. Rev.*, **49**:931, 1936.

[157] J. C. Slater. *Phys. Rev. B*, **49**:537, 1936.

[158] A. Ślebarski, W. Glogowski, A. Jezierski, A. Czopnik, and A. Zygmunt. *Phys. Rev. B*, **70**:184429, 2004.

[159] I. V. Solovyev and M. Imada. *Phys. Rev. B*, **71**:045103, 2005.

[160] H. Spiering, L. Deak, and L. Bottyan. *Hyperfine Interact.*, **125**:197, 2000.

[161] E. C. Stoner. *Proc. R. Soc. Lond. A*, **165**:372, 1938.

[162] J. Tabola and J. Pierre. *J. Alloys Compds.*, **296**:243, 2000.

[163] T. Takabatake, Y. Nakazawa, and Ishikawa. *Jpn. J. appl. Phys. (Suppl.)*, **26**:547, 1987.

[164] R. Y. Umetsu, K. Kobayashi, A. Fujita, K. Oikawa, R. Kainuma, K. Ishida, N. Endo, K. Fukamichi, and A. Sakuma. *Phys. Rev. B*, **72**:214412, 2005.

[165] J. H. van Vleck. *Rev. Mod. Phys.*, **25**:220, 1953.

[166] R. Vijayaraghavan. *J. Magn. Magn. Mater.*, **47-48**:561, 1985.

[167] P. Villars and L. D. Calvert. ASM International, Materials Park, 1996.

[168] S. H. Vosko, L. Wilk, and M. Nusair. *Can. J. Phys.*, **58**:1200, 1980.

[169] W. H. Wang, M. Przybylski, W. Kuch, L. I. Chelaru, J. Wang, F. Lu, J. Barthel, H. L. Meyerheim, and J. Kirschner. *Phys. Rev. B*, **71**:144416, 2005.

[170] W. H. Wang, M. Przybylski, W. Kuch, L. I. Chelaru, J. Wang, Y. F. Lu, J. Barthel, and J. Kirschner. *J. Magn. Magn. Mater.*, **286**:336, 2005.

[171] S. M. Watts, S. Wirth, S. v. Molnàr, A. Barry, and J. M. D. Coey. *Phys. Rev. B*, **61**:9621, 2000.

[172] P. J. Webster. *J. Phys. Chem. Solids*, **32**:1221, 1971.

[173] P. J. Webster and K. R. A. Ziebeck. *Landolt-Börnstein - Group III Condensed Matter*, volume **19C**. Springer-Verlag, Heidelberg, 1988.

[174] G. Wortmann, E. V. Sampathkumaran, and G. Kaindl. *J. Magn. Magn. Mater.*, **54-57**:338, 1986.

[175] S. Wurmehl, G. H. Fecher, and C. Felser. *Z. Anorg. Allg. Chem.*, **61b**:749, 2006.

[176] S. Wurmehl, G. H. Fecher, Hem C. Kandpal, V. Ksenofontov, and C. Felser. *Phys. Rev. B*, **72**:184434, 2005.

[177] S. Wurmehl, G. H. Fecher, V. Ksenofontov, F. Casper, U. Stumm, C. Felser, H.-J. Lin, and Y. Hwu. *J. Appl. Phys.*, **99**:08J103, 2006.

[178] S. Wurmehl, Hem C. Kandpal, G. H. Fecher, and C. Felser. *J. Phys. Condens. Matter*, **18**:6171, 2006.

[179] M. V. Yablonskikh, Yu. M. Yarmoshenko, E. G. Gerasimov, V. S. Gaviko, M. A. Korotin, E. J. Kurmaev, S. Bartkowski, and M. Neumann. *J. Magn. Magn. Mater.*, **256**:396, 2003.

[180] J. Zaanen, G. A. Sawatzky, and J. W. Allen. *Phys. Rev. Lett.*, **55**:418, 1985.

[181] K. R. A. Ziebeck and K.-U. Neumann. *Landolt-Börnstein - Group III Condensed Matter*, volume **32C**. Springer-Verlag, Heidelberg, 2001.

[182] E. Zintl. *Angew. Chem.*, **52**:1, 1938.

[183] I. Zutic, J. Fabian, and S. D. Sharma. *Rev. Mod. Phys.*, **76**:323, 2004.

[184] A. Zygmunt and A. Szytula. *J. Alloys Compds.*, 219 (1-2):185, 1995.

Appendix A

General information about the Slater-Pauling rule

Slater [156] and Pauling [126] first reported that the magnetic moments (m) of $3d$ elements and their binary compounds can be described by the mean number of valence electrons (n_V) per atom. The rule distinguishes the dependence of $m(n_V)$ into two regions. The first (closed packed structures: *fcc, hcp*) is the range of itinerant magnetism ($n_V \geq 8$) and the second (*bcc*) is the one of localized moments ($n_V \leq 8$), where Fe is a borderline case. According to Hund's rule it is often favorable for the majority d states to be fully occupied ($n_{d\uparrow} = 5$). Starting from $m = 2n_\uparrow - n_V$, this leads to the definition of the magnetic valence to be $n_M = 10 - n_V$ such that the magnetic moment per atom is given by $m = n_M + 2n_{sp\uparrow}$. Pauling gave a value of $n_{sp\uparrow} \approx 0.3$ for the second region. A plot of m versus magnetic valence ($m(n_M)$) is called the generalized Slater-Pauling rule, as described by Kübler [101]. In the case of localized moments, the Fermi energy is pinned in a deep valley of the minority electron density. This constrains $n_{d\downarrow}$ to be approximately three resulting in $m \approx n_V - 6 - 2n_{sp\downarrow}$, for Fe and its *bcc*-like binary alloys (Fe-Cr, Fe-Mn, and partially Fe-Co). It was shown by Malozemoff *et al.* [112] using *band-gap theory* that these arguments principally hold as well if using more realistic band structure models, even though they were initially derived from rigid band models. In particular, they have shown that the rule is still valid if metalloids are involved.

Half-metallic ferromagnets are supposed to exhibit a real gap in the minority density of states where the Fermi energy is pinned. The gap has the consequence that the number of occupied minority states has to be an integer. Thus, the Slater-Pauling rule will be strictly fulfilled with

$$m_{HMF} = n_V - 6 \tag{A.1}$$

for the spin magnetic moment per atom.

For ordered compounds with different kind of atoms it may be more convenient to use all atoms of the unit cell. In the case of 4 atoms per formula unit cell, as in Heusler (H) compounds, one has to subtract 24 (6 times the number of atoms) from the accumulated number of valence electrons N_V (s, d electrons for the transition metals and s, p electrons for the main group element) to find the spin magnetic moment M per unit cell:

$$M_H = N_V - 24. \tag{A.2}$$

This *rule of thumb* is strictly fulfilled for HMF only as first noted in [101] for cubic $C1_b$ (hH) compounds ($M_{hH} = N_V - 18$). In both types of compounds (X_2YZ and XYZ) the spin magnetic moment per unit cell becomes strictly integer for half-metallic ferromagnets. An already very small

deviation from an integer value indicates that the HMF character is completely lost. This situation changes for alloys with non-integer site occupancies like the quaternaries $X_2Y_{1-x}Y'_xZ$. In such cases M may become non-integer depending on the composition, even for the HMF state.

The Slater-Pauling rule relates the magnetic moment with the number of valence electrons, but is not formulated to predict a half-metallic ferromagnet.

Appendix B

Coulomb, exchange integrals and U_{eff} values

The average on-site Coulomb energy of pairs (ij) of equivalent electrons $(i = j)$ is calculated from the Slater integrals F_k to be

$$E_{ii} = F_{0,ii} - \frac{2l_i + 1}{4l_i + 1} \sum \begin{pmatrix} l_i \, k \, l_i \\ 0 \, 0 \, 0 \end{pmatrix}^2 F_{k,ii} \tag{B.1}$$

The sum runs over all $k > 0$ resulting in non-zero $3j$ symbols. The $3j$ symbols vanish for odd k, and $k_{max} = 2l_i = 4$ for d electrons so that Eq. B.1 becomes

$$E_{dd} = F_0 - \frac{2}{63}F_2 - \frac{2}{63}F_4, \tag{B.2}$$

where the on-site Coulomb integral is $U = F_0$, and all integrals are calculated for $l = 2$. The exchange integral is given by

$$J = \frac{2}{63}(F_2 + F_4). \tag{B.3}$$

Equation B.3, as calculated from Cowans's work [40], differs from the equation reported by Anisimov *et al.* [3] giving a factor 1/14 instead of 2/63. The difference is caused by weighting factors used for the spin of the electrons. The weighting factors in the LDA+U approach of Anisimov is for half of the electrons. (spin-up and spin-down are respected separately), whereas Cowan uses the average over all electrons of a particular shell. [1].

The atomic values of $U = F_0$, J, and $U_{eff} = E_{dd}$, as calculated for the $3d$ transition metals, are displayed in Figure B.1. In the following, we will denote the U_{eff} values by U_x, where the subscript x stands for the values (in %) relative to the atomic values (neutral atoms). It should be mentioned that the effect of screening in solids will mainly influence U rather than the exchange integrals J. On the other hand, the values of J also depend on the ionicity (see Figure B.1(b)), which will be different in solids and depend upon the compound under investigation. From a practical point of view, the use of U_x relative to the atomic values allows comparisons to be made between different systems that are easier to accomplish than those that use separate values for all quantities and atoms.

[1] This also affects the exchange integrals for f electrons, compare Ref. [40] Table: 6-1 page 165 and Ref. [3].

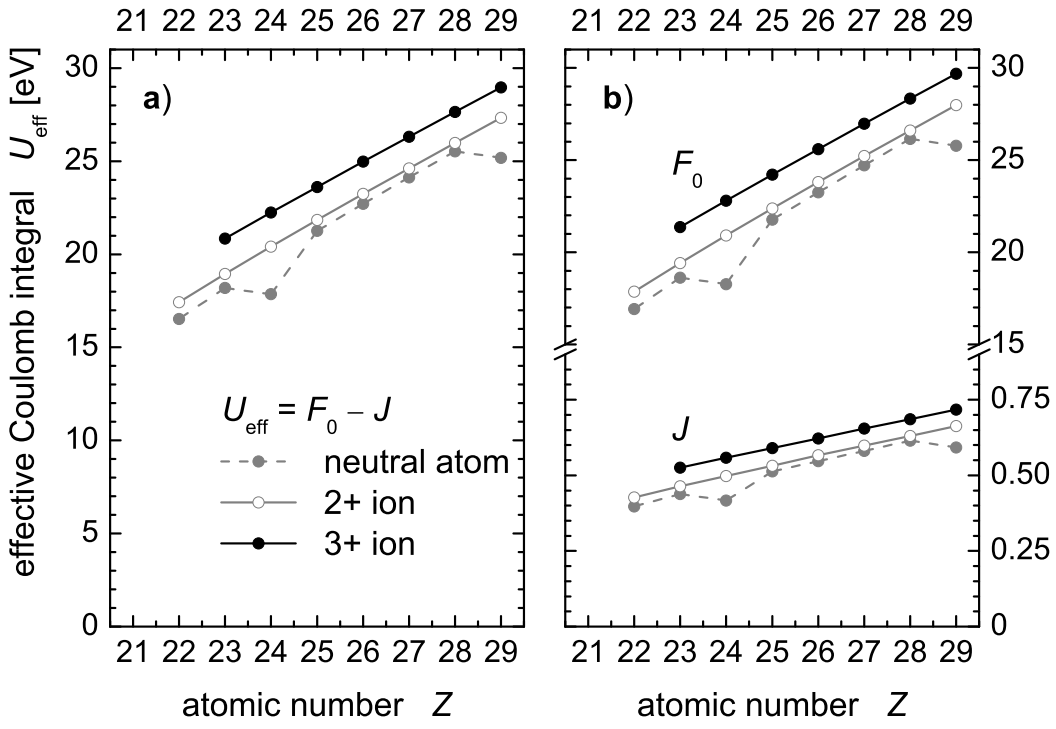

Figure B.1: Atomic Coulomb exchange parameter. The values were calculated for the 3*d* transition metals using the neutral as well as the most common ionic configurations. Note that the values for J in (b) are shown on an expanded scale below the break.

Appendix C

Band direction in Heusler compounds

Most of the Heusler compounds exhibit a gap along Γ - X, *i.e.* in the Δ-direction. This gap is defined by the external energies at the Γ and X points. Generally, it is seen in Heusler compounds, that the majority bands cross or touch the Fermi-energy (ϵ_F) in rather all directions of high symmetry. For Co_2CrAl, the width of the gap is given by the energies of the highest occupied band at the Γ-point and the lowest unoccupied band at the Γ or X-point. The Δ-direction is perpendicular to the Co_2 (100)-planes. The smaller value is found between Γ and X, thus it is an indirect gap. It should be noted that the direct gap at the Γ-point is only $60meV$ wider. Therefore, a small change in the parameters of the calculation may already change the character of the gap from indirect to direct. This could be the one reason why some LMTO calculations resulted in a direct gap. Therefore Δ-direction plays the important role for the understanding of the HMF character and magnetic properties of Heusler compounds. This role of the Δ-direction was also pointed out by Öğüt and Rabe [124].

More interesting is the behavior of the minority bands which determine the HMF character of the compounds. Comparing Cr and Fe based compounds, the energies of the states at Γ are nearly the same and occur below ϵ_F. The shapes of the bands close to Γ are similar. The situation is different at X where the unoccupied states are shifted towards ϵ_F in Co_2FeAl compared to Co_2CrAl.

The gap in the half-metallic $C1_b$ compounds is usually indirect, with the maximum of the valence band at the Γ point and the minimum of the conduction band at the X point.

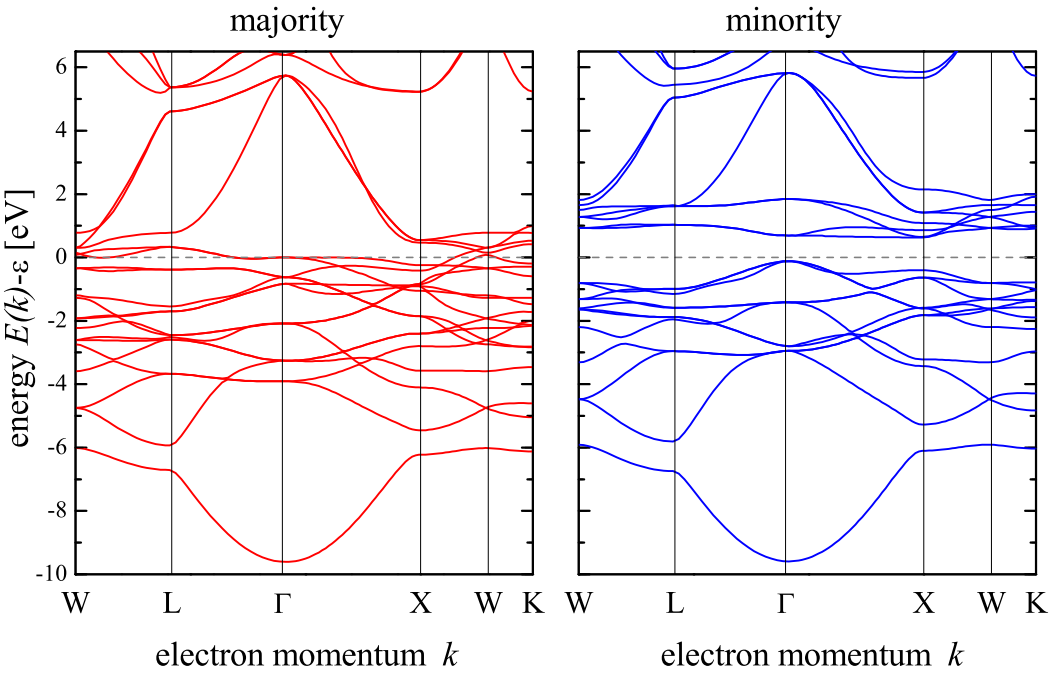

Figure C.1: Band structure of Co_2CrAl

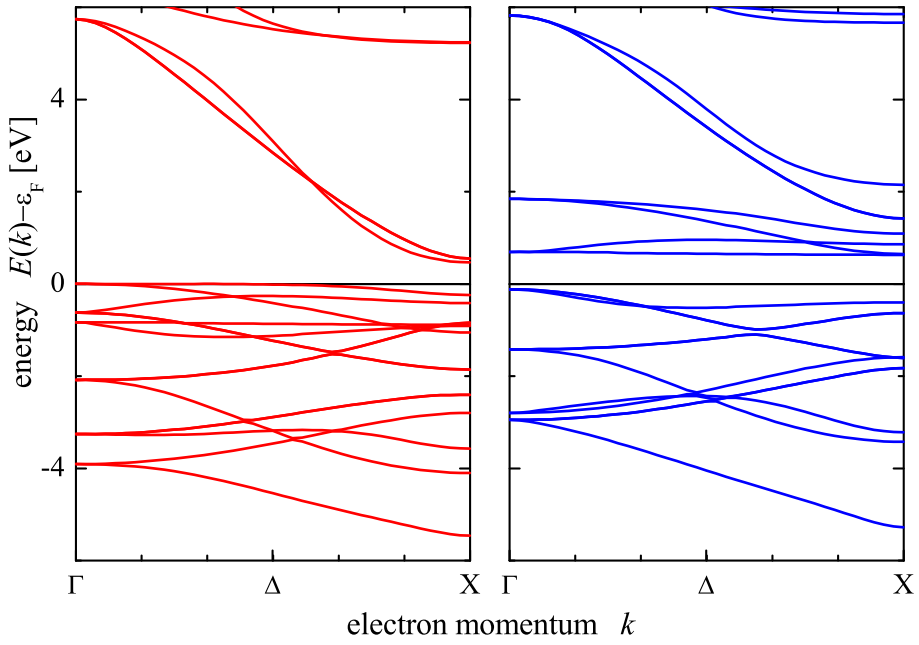

Figure C.2: Δ bands of Co_2CrAl

Appendix D

Results for Heusler compounds from FLAPW calculations (Wien2k)

D.0.1 Explanation of the columns in the following tables

The lattice parameter a is given in Å, a superscript asterisk ($\star$) assigns a lattice parameter found from the structural optimization.

The experimental transition temperatures T_{exp} for magnetic order are given in K. m = 0 and $T_{exp} \neq 0$ assigns antiferromagnetic compounds with Neel-temperature $T_N = T_{exp}$, otherwise $T_{exp} = T_C \neq 0$ gives the Curie temperature of ferro- or ferri-magnetic compounds.

The following abbreviations for the magnetic order (MO), found in the calculations are used:

- P paramagnetic, simple metal
- F ferromagnetic, Fi ferrimagnetic
- HMF ferromagnetic, half-metallic (HMFi, ferrimagnetic)
- SM semi-metallic, FSM ferromagnetic, semi-metallic
- SC semiconductor

The total magnetic moment m_t and experimental magnetic moments m_{exp} are given in μ_B per unit cell, the element specific values $m_{X,Y}$ are given in μ_B per atom (Note: the element specific values depend on the size of the sphere used for the integration).

Table D.1: Mn_2YZ Heusler compounds

Y	Z	a	m	T_{exp}	MO	m_t	m_x	m_y	N_v
V	Al	5.897	1.82		HMFi	1.99	1.52	-0.95	22
	Ga	6.095	1.66		Fi	3.99	2.88	-1.62	
Mn	Si	5.722			HMFi	1	-0.88	2.69	25
Fe	Si	5.45*			F	2.11	0.07	1.96	26
Ni	Sn	6.099	2.48		F	6.89	3.24	0.48	28

Table D.2: Fe_2YZ based Heusler compounds

Y	Z	a	m	T_{exp}	MO	m_t	m_x	m_y	N_v
Ti	Al	5.879	0.11	123	Fi	0.95	0.67	-0.28	23
V	Al	5.761	0		SM	0	0	0	24
	Ga	5.782	0		SM	0.03	-0.03	0.05	24
Ti	Sn	6.053	0		P	0	0	0	24
V	Si	5,675	0		Fi	0.8	0.54	-0.17	25
	Sn	5.959	1.32	200	Fi	0.84	0.68	-0.4	25
Cr	Al	5.805	1.67	246	Fi	1.95	1.32	-0.3	25
	Ga	5.824	2.6		Fi	2.04	1.46	-0.71	25
Mn	Al	5.816	1.58		F	4.71	1.6	1.76	26
Mn	Si	5.671	2.33	214	HMF	3	0.2	2.63	27
Fe	Al	5.792	2.59	713	F	6.05	1.97	2.43	27
	Ga	5.807			F	6.36	2.08	2.45	27
Fe	Si	5.653	2.21	823	F	5.11	1.38	2.57	28
Co	Al	5.81	2.06		F	6.12	2.26	1.85	28
	Ga	5.767	5.09		F	6.15	2.25	1.85	28
Co	Si	5.639	5.09		F	4.89	1.64	1.79	29
	Ge	5.775			F	5.68	2.06	1.75	29
Ni	Al	5.758	4.25		F	4.55	2.12	0.6	29
	Ga	5.78	3.21		F	4.78	2.24	0.55	29

Table D.3: Co_2YZ based Heusler compounds

Y	Z	a	m	T_{exp}	MO	m_t	m_x	m_y	N_v
Sc	Al	5.962			P	0	0	0	24
Sc	Ga	6.17			P	0	0	0	24
Sc	Si	5.862			HMF	1	0.6	-0.09	25
SC	Ge	5.78			F	1	0.58	-0.08	25
Sc	Sn	6.188			F	1.04	0.66	-0.14	25
Ti	Al	5.847			HMFi	1	0.62	-0.11	25
Ti	Ga	5.85			HMFi	1	0.63	-0.15	25
Ti	Si	5.743	1.65	375	HMF	2	1.03	-0.02	26
Ti	Ge	5.807	1.59	386	HMF	1.97	1.05	-0.06	26
Ti	Sn	6.077	1.96	371	HMF	1.96	1.08	-0.07	26
V	Al	5.772	1.95	310	F*	1.96	0.99	0.1	26
V	Ga	5.779	1.92	352	HMF	2.01	0.97	0.16	26
V	Si	5.657*			HMF	3	1.09	0.8	27
V	Sn	5.96	1.21	95	HMF	3.03	1.1	0.86	27
Cr	Al	5.727	1.55	334	HMF	3	0.83	1.47	27
Cr	Ga	5.805	3.01	495	F*	3.05	0.755	1.64	27
Cr	In	6.06	1.18		F	3.2	0.67	1.98	27
Cr	Si	5.65*			HMF	3.99	1.03	1.99	28
Mn	Al	5.749	4.04	693	F*	3.8	0.84	2.58	28
Mn	Ga	5.767	4.05	694	F*	4.14	0.77	2.75	28
Mn	Si	5.645	4.9	985	HMF	5	1	3	29
Mn	Ge	5.749	4.93	905	HMF	5	1.02	3.06	29
Mn	Sn	5.984	5.08	829	F*	5	0.98	3.2	29
Fe	Al	5.73	4.96		HMF	4.98	1.23	2.78	29
Fe	Ga	5.737	5.17	1093	F*	5	1.21	2.8	29
Fe	In	5.716			F	4.96	1.21	2.73	29
Mn	Sb	5.917	4.52		HMF	6	1.27	3.45	30
Fe	Si	5.64	6	1100	F	5.59	1.4	2.87	30
Fe	Ge	5.738	5.54		F	5.57	1.4	2.84	30
Zn	Ge	5.74			F	0.45	0.26	-0.02	34

Table D.4: Ni_2YZ Heusler compounds

Y	Z	a	m	T_{exp}	MO	m_t	m_x	m_y	N_v
Sc	Al	5.99			P	0	0	0	26
Sc	Ga	6.025			P	0	0	0	26
Sc	In	6.256			P	0	0	0	26
Sc	Sn	6.215			P	0	0	0	27
Ti	Al	5.895			P	0	0	0	27
Ti	Sn	6.09			P	0	0	0	28
V	Al	5.803			P	0	0	0	28
Ti	Sb	6.032			P	0	0	0	29
V	Sn	6.04			F	0.6	-0.02	0.62	29
Cr	Al	5.737	0.13	140	F	3.18	0.34	2.46	29
Mn	Al	5.824	0	30	F	4.16	0.4	3.39	30
Mn	Ga	5.835	4.07	379	F	4.14	0.38	3.42	30
Mn	In	6.075	4.34	323	F	4.28	0.33	3.65	30
Mn	Sn	6.053	4.05	360	F	4.1	0.24	3.64	31
Fe	Ga	5.741			F	3.27	0.256	2.83	31
Mn	Sb	5.982	3.52	365	F	3.81	0.2	3.53	32
Ni	Sn	5.98			P	0	0	0	34
Cu	Sb	5.86			P	0	0	0	36
Zn	Ge	5.74			P	0	0	0	36

Table D.5: Cu_2YZ Heusler compounds

Y	Z	a	m	T_{exp}	MO	m_t	m_x	m_y	N_v
Sc	Al	6.199			P	0	0	0	28
Sc	In	6.378			P	0	0	0	28
Ti	Al	6.01			P	0	0	0	29
Ti	In	6.22			P	0	0	0	29
Cr	Al	5.809			F	2.74	0.04	2.64	31
Mn	Al	5.968			F	3.52	0.02	3.49	32
Mn	In	6.206			F	3.75	0.02	3.67	32
Mn	Sn	6.168			F	3.84	0.03	3.66	33
Mn	Sb	6.096			F	3.76	0.03	3.57	34
Ni	Sn	5.969			P	0	0	0	36

Table D.6: X_3Z binary Heusler like compounds

Y	Z	a	m	T_{exp}	MO	m_t	m_x	m_y	N_v
Mn_3	Si	5.722			HMFi	1	-0.88	2.69	25
Mn_3	Si	5.722	0	25.8	AFM				
Fe_3	Al	5.792	2.59	713	F	6.05	1.97	2.43	27
Fe_3	Ga	5.807			F	6.36	2.08	2.45	27
Fe_3	Si	5.653	2.21	823	F	5.11	1.38	2.57	28
Fe_3	Ge	5.75			F	6	1.87	2.48	28
Ni_3	Sn	5.98	0		P	0	0	0	34

Table D.7: X_2YZ (X = 3*d* and Y = 4*d* or 5*d*) Heusler compounds

X_2	Y	Z	a	m	T_{exp}	MO	m_t	m_x	m_y	N_v
Co_2	Li	Ge	5.673			P	0	0	0	23
Mn_2	W	Sn	6.317	1.54	258	Fi	4.34	2.66	-0.68	24
Co_2	Be	Si	5.37			P	0	0	0	24
Co_2	Be	Ge	5.46			P	0	0	0	24
Fe_2	Mo	Al	5.918	0.36		P	0.84	0.51	-0.07	25
Co_2	Zr	Al	6.078	0.79	178	HMF	1	0.62	-0.1	25
Co_2	Hf	Al	6.045	0.82	193	HMF	1	0.61	-0.09	25
Co_2	Hf	Ga	6.032	0.6	186	F*	1	0.604	-0.09	25
Co_2	Nb	Al	5.935	1.35	383	HMF	2	1.04	0.01	26
Co_2	Nb	Ga	5.95	1.39		HMF	2	1.037	-0.01	26
Co_2	Zr	Sn	6.254	1.81	448	HMF	1.99	1.09	-0.09	26
Co_2	Hf	Sn	6.227	1.57	394	HMF	2	1.07	-0.07	26
Co_2	Nb	Sn	6.155*	0.69	105	F*	1.94	0.95	0.07	27
Fe_2	Ir	Si	4.999	3	662	F	2.60	1.03	0.50	27
Cu_2	Li	Si	5.776			P	0	0	0	27
Fe_2	Ru	Si	5.76			F	4.49	1.77	1.08	28
Ni_2	Zr	Sn	6.276	0		P	0	0	0	28
Ni_2	Nb	Sn	6.356	0		P	0	0	0	29
Ni_2	Hf	Sn	6.24	0		P	0	0	0	29

Table D.8: X_2YZ (X = 4*d* or 5*d* and Y = 3*d*) Heusler compounds

X_2	Y	Z	a	m	T_{exp}	MO	m_t	m_x	m_y	N_v
Pt_2	Sc	In	6.512			P	0	0	0	26
Pt_2	Sc	Sn	6.512			P	0	0	0	27
Pt_2	Ti	In	6.55			P	0	0	0	27
Pd_2	Sc	Sn	6.504			P	0	0	0	27
Ru_2	Mn	Ge	5.985			F	3.03	-0.008	3.00	27
Ru_2	Mn	Si	5.887			F	3.00	0.02	2.92	27
Ru_2	Mn	Sn	6.217			F	3.08	-0.06	3.21	27
Rh_2	V	Sn	6.192			F	2.58	0.40	1.64	27
Ru_2	Mn	Sb	6.200			F	4.02	0.22	3.55	28
Ru_2	Fe	Si	5.865			F	3.85	0.41	2.97	28
Ru_2	Fe	Sn	6.202			F	4.13	0.49	3.17	28
Rh_2	Mn	Al	6.005			F	4.07	0.35	3.43	28
Rh_2	Mn	Ga	6.056			F	4.13	0.33	3.50	28
Rh_2	Mn	In	6.287			F	4.36	0.31	3.79	28
Rh_2	Mn	Tl	6.324			F	4.44	0.31	3.83	28
Ag_2	Sc	Al	6.564			P	0	0	0	28
Au_2	Sc	Al	6.535			P	0	0	0	28
Au_2	Sc	In	6.692			P	0	0	0	28
Ir_2	Mn	Al	6.025			HMF	3.99	0.24	3.5	28
Ir_2	Mn	Ga	6.052			F	4.01	0.26	3.46	28
Au_2	Ti	Al	6.400			P	0	0	0	29
Rh_2	Mn	Ge	6.044			F	4.76	0.48	3.74	29
Rh_2	Mn	Sn	6.232	3.4	410	F	4.77	0.44	3.84	29
Rh_2	Mn	Pb	6.271	2.9	335	F	4.77	0.43	3.87	29
Pd_2	Mn	In	6.373	4.3		F	4.22	0.11	4.03	30
Pd_2	Mn	Ga	6.174	3.2	170	F	4.10	0.1	3.90	31
Pd_2	Mn	Sn	6.380	4.23	189	F	4.16	0.1	4.01	31
Pd_2	Mn	Sb	6.419	4.4	247	F	4.31	0.1	4.1	32
Rh_2	Ni	Sn	6.136			F	1.03	0.21	0.65	32
Rh_2	Cu	Sn	6.146			P	0	0	0	33
Au_2	Mn	Al	6.358	4.2	233	F	3.83	0	3.84	34

Table D.9: Anti-ferromagnetic (AFM-I) calculations for Y = 3*d* based Heusler compounds

X_2	Y	Z	a	m	T_{exp}	MO	m_t	m_x	m_y	N_v
Pd_2	Ti	In	6.365	0	110	AFM			27	
Pt_2	Mn	Al	6.24	0	190	AFM-I	0	±3.86	30	
Pt_2	Mn	Ga	6.16	0	75	AFM-I	0	±3.78	30	
Au_2	Mn	Ga		0		AFM			34	
Au_2	Mn	In		0		AFM			34	

Table D.10: Ferromagnetic calculations for Y = 3*d* based Heusler compounds including spin-orbit interaction

X_2	Y	Z	a	m	T_{exp}	MO	m_t	m_x	m_y	N_v
Pt_2	Sc	In	6.512			P	0	0	0	26
Pt_2	Sc	Sn	6.512			P	0	0	0	27
Pt_2	Ti	In	6.55			P	0	0	0	27
Au_2	Sc	Al	6.535			P	0	0	0	28
Au_2	Sc	In	6.692			P	0	0	0	28
Ir_2	Mn	Al	6.025			HMF	3.98	0.28	3.4	28
Ir_2	Mn	Ga	6.052			F	3.44	0.16	3.35	28
Pt_2	Mn	Al	6.24	0	190	AFM-I	0	0	±3.85	30
Pt_2	Mn	Ga	6.16	0	75	AFM-I	0	0	±3.74	30
Au_2	Mn	Al	6.36	4.2	233	F	3.83	0	3.83	34

Table D.11: Rare earth containing Heusler compounds

X_2	Y	Z	a	m	T_{exp}	MO	m_t	m_x	m_y	N_v
Pd_2	Gd	In	6.741	0	7	AFM-I	0	0	±7.0	26+7
Cu_2	Gd	In	6.641	0	10	AFM-I	0	0	±7.03	28+7
Ag_2	Gd	In	6.965	0	10	AFM-I	0	0	±7.04	28+7
Au_2	Gd	In	6.94			AFM-I	0	0	±6.99	28+7
Cu_2	Tb	In	6.623		7.5	AFM-I				28+8

Table D.12: Superconducting Heusler compounds

Y	Z	a	m	T_{exp}	MO	m_t	m_x	m_y	N_v
Pd_2	Y	In	6.72	1.04	P	0	0	0	26
Pd_2	Y	Sn	6.718	4.9	P	0	0	0	26
Ni_2	Hf	Al	6.069	0.74	P	0	0	0	27
Ni_2	Zr	Al	6.106	1.38	P	0	0	0	27
Ni_2	Hf	Ga	6.045	1.12	P	0	0	0	27
Ni_2	Nb	Sn	6.179	3.4	P	0	0	0	28
Au_2	Y	In	6.905	1.74	P	0	0	0	28

Table D.13: Minority gap in X_2YZ Heusler compounds

Mn_2YZ					
Y	Z	E_{gap}	E_{min}	E_{max}	N_v
V	Al	0.318	-0.549	0.264	22
Mn	Si	0.624	-0.007	0.617	25
Fe_2YZ					
Y	Z	E_{gap}	E_{min}	E_{max}	N_v
Mn	Si	0.633	-0.083	0.55	27
Co_2YZ					
Y	Z	E_{gap}	E_{min}	E_{max}	N_v
Sc	Si	0.246	-0.009	0.237	25
Sc	Ge	0.034	0.143	0.177	25
Ti	Al	0.456	-0.24	0.215	25
Ti	Ga	0.21	0.06	0.216	25
Ti	Si	0.785	-0.606	0.179	26
Ti	Ge	0.595	-0.401	0.194	26
Ti	Sn	0.504	-0.222	0.282	26
V	Al	0.238	-0.357	-0.119	26
V	Ga	0.189	-0.142	0.047	26
V	Si	0.789	-0.856	-0.067	27
V	Sn	0.548	-0.397	0.151	27
Cr	Al	0.748	-0.118	0.63	27
Cr	Ga	0.425*	0.203	0.628	27
Cr	Si	0.878	-0.412	0.466	28
Mn	Al	0.626*	0.256	0.882	28
Mn	Ga	0.369*	0.362	0.731	28
Mn	Si	0.798	-0.292	0.506	29
Mn	Ge	0.581	-0.048	0.533	29
Mn	Sn	0.411*	0.183	0.594	29
Fe	Al	0.111	-0.138	-0.027	29
Fe	Ga	0.021*	0.086	0.107	29

Co_2YZ					
Y	Z	E_{gap}	E_{min}	E_{max}	N_v
Mn	Sb	0.648	-0.604	0.044	30
Fe	Si	0.146*	-0.735	-0.589	30
Fe	Ge	0.087	-0.517	-0.43	30
Co_2YZ					
Y	Z	E_{gap}	E_{min}	E_{max}	N_v
Zr	Al	0.296	-0.116	0.18	25
Hf	Al	0.363	-0.211	0.152	25
Nb	Al	0.557	-0.49	0.067	26
Nb	Ga	0.527	-0.269	0.258	26
Zr	Sn	0.54	-0.236	0.304	26
Hf	Sn	0.48	-0.277	0.203	26

Appendix E

Results for cubic $C1_b$ compounds

Table E.1: Cubic $C1_b$ compounds based on $3d$ transition metals

Cubic $C1_b$ compounds based on two $3d$ transition metals										
X	Y	Z	a	m	T_{exp}	MO	m_t	m_x	m_y	N_v
Fe	Ti	Sn	6.056			F*	1.63	1.73	-0.2	16
Mn	V	Sb	5.93*			HMFi	1	2.1	-1.11	17
Fe	Ti	Sb	5.957			HMF	1.03	1.03	-0.06	17
Co	Ti	Sn	5.997	0.357	135	SC	0.95	0.41	0.35	17
Fe	V	Sb	5.816			SC	0	-0.19	0.19	18
Co	Ti	Sb	5.884			SC	0	0	0	18
Ni	Ti	Sn	5.941			HMF	0	0	0	18
Co	V	Sb	5.8	0.18	58	P	1	-0.19	1.12	19
Ni	Ti	Sb	5.872			HMF	0.02	0	0.02	19
Co	Cr	Sb	5.84*			HMF	2	-0.43	2.45	20
Ni	V	Sb	5.785			HMF	1.99	0.12	1.73	20
Co	Mn	Sb	5.875	3.89	490	HMF	3.03	3.31	-0.23	21
Co	Fe	Sb	5.8*			HMF	3.98	1.03	2.98	22
Ni	Mn	Sb	5.927	3.98	730	HMF	3.97	3.72	0.24	22
Ni	Fe	Sb	5.72	2.36		FSM	3.33	0.41	2.87	23
Cu	Mn	Sb	6.095	3.9	55	AFM	0	0	$\pm$4.26	23

Table E.2: Cubic $C1_b$ compounds based on $3d$ transition metals

Cubic $C1_b$ compounds based on one $3d$ transition metal on Y sites										
X	Y	Z	a	m	T_{exp}	MO	m_t	m_x	m_y	N_v
Pt	Ti	Sn	6.16			P	0	0	0	18
Ru	Mn	Ga	6.15	0.3	220	F	4	0.03	3.79	18
Mg	Cu	Bi	6.256							18
Li	Zn	P	5.77							18
Na	Zn	As	5.912							18
Ir	Mn	Ga	6.027		60	F	4.11	0.14	3.9	19
Pt	Mn	Ga	6.15	3.18	220	F	4.08	0.09	4.01	20
Rh	Mn	Sb	6.152	3.95	320	Fi	3.41	-0.11/-0.13	3.64	21
Ir	Mn	Sb	6.164	3.8	290	Fi*	3.14	-0.17/-0.1	3.47	21
Pt	Mn	Sn	6.263	3.57	330	F	3.74	0.02	3.87	21
Pd	Mn	Sb	6.285	3.97	500	F*	4.11	0.09	4.06	22
Pt	Mn	Sb	6.203	4.02	585	HMF	4.01	0.11	3.92	22
Au	Mn	Sn	6.34	3.8	600	F*	4.06	0.04	4.04	22
Pd	Mn	Te	6.271	0	23	AFM	0	0	$\pm$4.24	23
Pd	Mn	Te	6.271			F	4.9	0.26	4.28	23
Au	Mn	Sb	6.377	2.21	72	F	4.63	0.11	4.23	23
Ag	Zn	As	5.912							28

Table E.3: Cubic $C1_b$ compounds based on one $3d$ transition metal on Y sites including spin-orbit interaction

X	Y	Z	a	m	T_{exp}	MO	m_t	m_x	m_y	N_v
Pt	Ti	Sn	6.16			P	0	0	0	18
Ir	Mn	Ga	6.027			F	4.07	0.13	3.77	19
Pt	Mn	Ga	6.15	3.18		F	4.08	0.09	3.99	20
Ir	Mn	Sb	6.164	3.8	290	Fi	3.16	-0.17	3.47	21
Pt	Mn	Sn	6.263	3.57	330	F	3.73	0.01	3.87	21
Pt	Mn	Sb	6.203	4.02	585	F	4.02	0.10	3.92	22
Au	Mn	Sn	6.34	3.8	600	F	4.07	0.04	4.04	22
Au	Mn	Sb	6.277	2.21	72	F	4.63	0.11	4.23	23

Table E.4: Cubic $C1_b$ compounds containing transition and rare earth metals

Cubic $C1_b$ compounds based on transition metals										
X	Y	Z	a	m	T_{exp}	MO	m_t	m_x	m_y	N_v
X	Y	Z	a	m	T_{exp}	MO	m_t	m_x	m_y	N_v
Co	Hf	Sb	6.04			Sc	0	0	0	18
Rh	Hf	Sb	6.238			Sc	0	0	0	18
Pd	Hf	Sn	6.299			Sc	0	0	0	18
Pt	Hf	Sn	6.31			Sc	0	0	0	18
Cubic $C1_b$ compounds containing rare earth metals										
Pt	Gd	Sb	6.572			Sc/AFM-I	0		±6.98	18+7
Pt	Gd	Sb	6.572			HMF	7		6.97	18+7
Au	Gd	Pb	6.775			AFM-I	0		±6.98	18+7
Au	Gd	Pb	6.775			F	7		6.96	18+7
Ni	Tb	Sb	6.31	0	5.5	SC/AFM-I	0		±5.92	18+8
Ni	Tb	Sb	6.31			HMF	5.97		5.92	18+8
Au	Tb	Pb	6.747			AFM-I	0		±5.86	18+8
Au	Tb	Pb	6.747			F*	5.95		5.87	18+8
Ni	Dy	Sb	6.305	0	3.5	AFM-I	0		±4.79	18+9
Ni	Dy	Sb	6.305			F	4.91		4.81	18+9
Pd	Dy	Sb	6.533			AFM-I	0		±4.75	18+9
Pd	Dy	Sb	6.533			F	4.88		4.79	18+9

Table E.5: Minority gap in $C1_b$ half-metallic ferromagnet compounds

Half-metallic ferromagnet, minority band gap						
X	Y	Z	E_{gap}	E_{min}	E_{max}	N_v
Fe	Ti	Sb	0.999	-0.019	0.98	17
Co	Ti	Sn	0.784	0.071	0.855	17
Co	V	Sb	0.976	-0.841	0.135	19
Co	Cr	Sb	0.810	-0.214	0.597	20
Ni	V	Sb	0.516	-0.559	-0.044	20
Co	Mn	Sb	0.85	-0.014	0.836	21
Co	Fe	Sb	0.507	-0.601	-0.094	22
Ni	Mn	Sb	0.488	-0.134	0.354	22
Pd	Mn	Sb	0.375*	0.309	0.684	22
Pt	Mn	Sb	0.777	0.065	0.842	22
Au	Mn	Sn	0.288*	0.145	0.433	22
Semi-conductor, band gap						
X	Y	Z	E_{gap}	E_{min}	E_{max}	N_v
Fe	V	Sb	0.466	-0.136	0.33	
Co	Ti	Sb	1.066	-0.018	1.047	
Co	Nb	Sn	0.996	-0.095	0.9	
Co	Zr	Sb	1.074	-0.127	0.947	
Co	Hf	Sb	1.137	-0.082	1.055	18
Ni	Ti	Sn	0.451	-0.114	0.337	
Rh	Hf	Sb	1.142	-0.012	1.13	
Pd	Hf	Sn	0.402	-0.139	0.263	
Pt	Hf	Sn	0.939	-0.889	0.05	

Appendix F

Table of known full and cubic $C1_b$ compounds built from $3d$ metals

Potential HMF materials are printed in bold. An $\star$ assigns materials being close to HMF behavior.

Table F.1: Table of known Heusler compounds built from two 3*d* metals

	Sc $3d^14s^2$	Ti $3d^24s^2$	V $3d^34s^2$	Cr $3d^54s^1$	Mn $3d^54s^2$	Fe $3d^64s^2$	Co $3d^74s^2$	Ni $3d^84s^2$
Mn_2			**Al**, Ga		**Si**	Si		Sn
Fe_2		Al, Sn Sn	Al, Ga Si	Al, Ga	Al **Si**	Al Si	Al, Ga Ge	Ga
Fe		Sn* **Sb**	Sb					
Co_2	Ga **Si**, Ge, Sn	**Al, Ga** **Si, Ge, Sn**	Al*, **Ga** **Si, Sn**	**Al**, Ga, In **Si**	Al, Ga **Si, Ge**, Sn **Sb**	**Al**, Ga*, In **Si**, Ge		
Co		**Sn** Sb	**Sb**	**Sb**	**Sb**	**Sb**		
Ni_2		Al Sn	Al Sn	Al	Al, Ga, In Sn Sb	Ga		Sn
Ni		Sn Sb	**Sb**		**Sb**	Sb		
Cu_2				Al	Al, In Sn			Sn
Cu					Sb			